Early Physics at the LHC using the CMS Electromagnetic Calorimeter

Claire Timlin

High Energy Physics
Blackett Laboratory
Imperial College London

A thesis submitted to the University of London
for the degree of Doctor of Philosophy
and the Diploma of Imperial College.

August 2008

Abstract

The Compact Muon Solenoid (CMS) is a general purpose detector at the Large Hadron Collider (LHC) at CERN. It has been designed to study proton-proton collisions at a centre of mass energy of 14 TeV. CMS has constructed an electromagnetic calorimeter (ECAL) with extremely good energy resolution using scintillating lead tungstate crystals. Radiation studies performed on samples of these crystals are presented in this thesis. Results obtained from operating large parts (supermodules) of the ECAL in a test beam are also presented and compared to simulation. Methods of measuring electron efficiencies with data have been developed, tested and used in the measurement of W and Z boson cross sections in electron decay modes.

Samples of ECAL crystals produced by the Shanghai Institute of Ceramics were tested during 2005 for radiation hardness by measuring the drop in light yield caused by irradiation. Results showed crystals were radiation hard enough for use in CMS. The ability to monitor crystals in situ and crystal non-uniformity have also been investigated.

During the summer of 2006, nine ECAL supermodules were placed in a test beam from the Super Proton Synchrotron. The variation in the fraction of energy contained in reconstructed ECAL clusters versus pseudorapidity was studied and the comparison between data and simulation is presented.

The depth of an electromagnetic shower is an input parameter in the CMS electron reconstruction algorithm. A study to optimise this value and validate part of the electron reconstruction chain is documented.

Tag and probe methods have been developed to measure online and offline electron efficiencies from data. Methods of estimating the background and subtracting it have been successfully employed. These efficiencies are used in the measurement of the inclusive W and γ^*/Z production cross sections in the electron decay channel, assuming 10 pb^{-1} of proton-proton data.

Acknowledgements

Thank you first and foremost to my parents, Margaret and Michael, and my sisters, Helen and Laura, who have always had so much faith in me. Thanks to my late Grandfather, 'Bamp', who sparked an interest in physics and maths that eventually led to this thesis. Much appreciation must go to my boyfriend, William Humphreys, for coping worryingly well with me leaving the country for two years to work at CERN.

Many thanks to Chris Seez, Geoff Hall and Jim Virdee for their supervision and guidance. Thanks also to the HEP group at Imperial College for giving me a place to study and to STFC for providing funding. Much gratitude to Matt Ryan for being 'the best boss I'll ever have', Georgios Daskalakis and Alex Zabi for working with me and making our meetings so entertaining and Peter Hobson for irradiating the crystals.

Thank you to David Wardrope for being such a good deskmate and to Nikos Rompotis for his sterling work keeping the Imperial College tag-probe tools alive. Molti baci to the lovely people at ENEA; Stefania, Angelica, Danilo, Marco, Ioan and many more for making my stay in Rome so productive and enjoyable and putting up with my terrible Italian.

Contents

List of Figures

List of Tables

Chapter 1

Large Hadron Collider

1.1 Introduction

The Large Hadron Collider (LHC) [1] at CERN [2] has been designed and constructed to study the nature of physics at very high energies. By investigating this previously inaccessible energy regime, physicists hope not only to shed light on mathematical inconsistencies of the Standard Model but also to investigate theories beyond it. The LHC is a machine capable of making the next step in the understanding of our universe. It is powerful enough to probe space-time more deeply than ever before, leading to the possible discovery of compactified extra dimensions [3]. Many particles will be produced in the highly energetically dense environment, possibly leading to the discovery of new symmetries and forces that are beyond the scope of the Standard Model [3]. The LHC is an accelerator designed for discovery; it is hoped and expected that it will provide the necessary insight to move closer to a Grand Unified Theory.

The LHC has been constructed in the existing $27km$ circumference tunnel previously occupied by the Large Electron Positron Collider (LEP) [4]. It is buried between 50 and $150m$ below ground beneath the Swiss-French border near Geneva (Fig.1.1). Bunches of protons will be accelerated clockwise and anti-clockwise by the LHC to an energy of $7TeV$ per beam, these bunches will be brought into collision at specific

points around the ring. When the LHC is operating at design luminosity about 20 inelastic proton collisions will occur every $25ns$. Periodically the LHC will circulate and collide lead ions, instead of protons, at an energy of $2.75TeV$ per nucleon in order to study the properties of quark gluon plasma [5].

There are two general purpose detectors at the LHC, CMS (Compact Muon Solenoid) [6] and ATLAS (A Toroidal LHC Apparatus) [7]. Such detectors surround the interaction region as fully as possible and have been designed and built to discover manifestations of new physics. In addition to these, there are LHCb [8] (Large Hadron Collider Beauty Experiment) and ALICE [9] (A Large Ion Collider Experiment). LHCb has been specially designed to study B-physics whilst ALICE is dedicated to investigating heavy ion physics when the LHC is colliding lead ions rather than protons.

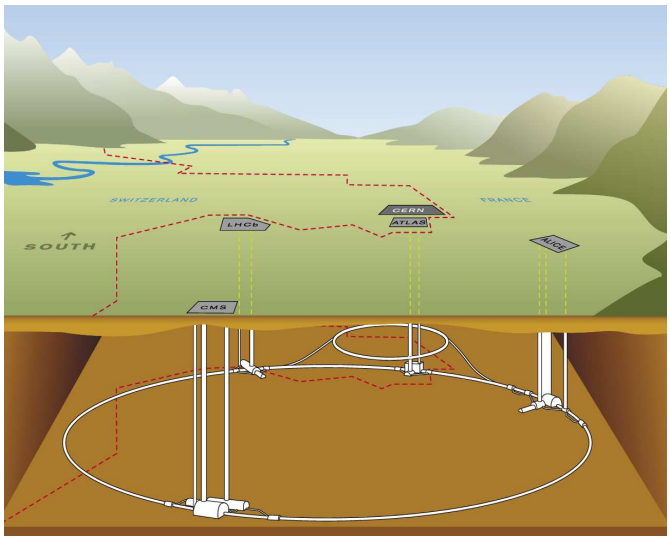

Figure 1.1: Schematic of the LHC showing experimental sites both above and below the surface.

1.2 Physics Motivation

The following section gives an overview of particle physics to date and what may lie beyond it. It explains the role of the LHC in the further development of this field.

1.2.1 Introduction to the Standard Model

The Standard Model of particle physics is a quantum field theory which encompasses all fundamental particles so far discovered and their interactions [10]. The building blocks of this highly successful model are twelve fermions, six leptons and six quarks, which can be arranged into three generations (Fig. 1.2). Interactions between these fermions are described in terms of the exchange of virtual bosons that are interpreted as quanta of force fields. Three out of the four known fundamental forces are included in the Standard Model: electromagnetism, the weak force and the strong force.

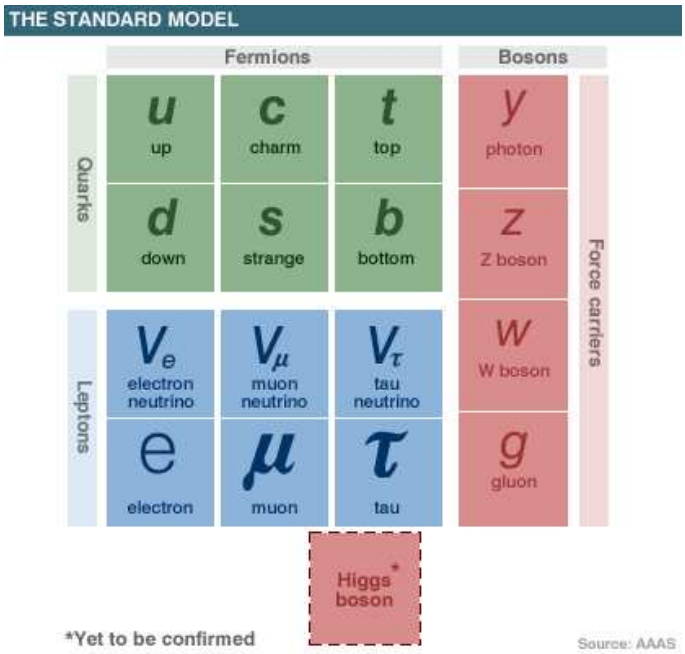

Figure 1.2: Constituents of the Standard Model of particle physics.

The force carrier of the infinite range electromagnetic force is a massless vector boson named the photon which acts on particles that possess electric charge. In contrast the short range weak force, responsible for radioactive decay, is mediated by three massive vector bosons (W^{+-} and Z) which couple to weak charge known as isospin. The strong force is responsible for holding nucleons together in the nucleus of atoms despite the tendency of electromagnetism to push them apart. The associated force carrier is a massless vector boson called the gluon which couples to particles that possess colour charge, namely quarks and other gluons.

The electromagnetic interaction is described by an Abelian field theory known as quantum electrodynamics (QED) and is based on a U(1) group. Weak and strong bosons carry isospin and colour respectively and require a non-Abelian theory for their description. Electroweak theory combines electromagnetic and weak interactions and is based on $SU(2)_L \times U(1)$ group. The strong interaction is described by quantum chromodynamics (QCD) based on unbroken SU(3) symmetry [10], [11].

Despite the many successes of the Standard Model, it is not quite complete. Electromagnetism and the weak forces have been shown to be low energy manifestations of the same interaction. However, the weak gauge bosons are very massive in contrast to the massless photon. The electroweak symmetry must therefore be broken at energies below the electroweak scale ($\sim TeV$) and it is postulated that the Higgs mechanism is responsible [12]. The theory predicts the existence of a Higgs field that permeates all space and endows with mass not only the weak gauge bosons but also the fundamental fermions. The quantum of this field, the Higgs boson, is thought to be the one remaining elusive piece of the Standard Model. One of the principal aims of the LHC is to discover and study this particle and complete the theory.

The next sections include more detail concerning electroweak theory and the Higgs mechanism and describe some theories beyond the Standard Model. The emphasis is placed on electroweak physics rather than QCD [10], [11] due to the relevance to this thesis.

1.2.2 Electroweak Interaction

The Glashow, Weinberg and Salam model [11] explains how electromagnetism and the weak force can be encompassed by one unified theory based on $SU(2)_L \times U(1)$ symmetry group. This section gives a brief description of this model and shows how its predictions compare with experiment.

The short range of the weak interaction implies that the mediating bosons are massive. However, in order to ensure local gauge invariance*, the initial Lagrangian of the theory does not include mass terms for the weak bosons. A scalar field, termed the Higgs field, is introduced into the theory and causes a spontaneous breakdown of the symmetry. This mechanism endows mass to the weak bosons and most fundamental fermions whilst leaving particles such as the photon and the neutrino massless.

The Dirac Lagrangian for massless fermions is:

$$\mathcal{L}_{dirac} = i\bar{\psi}\gamma^{\mu}\partial_{\mu}\psi = i\bar{\psi}\gamma \cdot \partial\psi \tag{1.1}$$

A fermion spinor (ψ) is a combination of left-handed and right-handed states:

$$\psi_L = \left(\frac{1-\gamma_5}{2}\right)\psi, \qquad \psi_R = \left(\frac{1+\gamma_5}{2}\right)\psi \tag{1.2}$$

where γ_5 is the product of the four Dirac γ matrices. Putting these into the Lagrangian (Eq. 1.1) along with the fact that γ_5 anticommutes with γ_μ :

$$\mathcal{L}_{dirac} = i\bar{\psi_R}\gamma \cdot \partial\psi_R + i\bar{\psi_L}\gamma \cdot \partial\psi_L \tag{1.3}$$

Only electrons will be considered in the following formula for brevity but the description applies to quarks and the other leptons. Electrons can exist in both left-handed and right-handed states but only left-handed neutrinos have ever been observed experimentally [13]. Considering this, the electron Lagrangian can be written as:

$$\mathcal{L}_{dirac} = ie\bar{_R}\gamma \cdot \partial e_R + ie\bar{_L}\gamma \cdot \partial e_L + i\bar{\nu_e}\gamma \cdot \partial\nu_e \tag{1.4}$$

From equation 1.4 it is evident that it is possible to group the left-handed electron and neutrino states into a doublet of weak isospin $I = \frac{1}{2}$ (Eq. 1.5). The right-handed

*Local gauge invariance is a symmetry of nature where matter fields transform by a phase which is a function of spacetime. This transformation can only leave the Lagrangian invariant if there are gauge potentials, interpreted as force carrying particles in the Standard Model, that transform similarly.

electron state does not have a partner with the same space-time properties and is therefore an isosinglet $I = 0$ (Eq.1.6).

$$\psi_L = \begin{pmatrix} \nu_e \\ e^- \end{pmatrix}_L \qquad \begin{matrix} I = \frac{1}{2}, & I_3 = +\frac{1}{2}, & Q = 0 \\ I = \frac{1}{2}, & I_3 = -\frac{1}{2}, & Q = -1 \end{matrix} \tag{1.5}$$

$$\psi_R = \left(e^-\right)_R \qquad I = 0, \quad Q = -1 \tag{1.6}$$

where Q is electric charge and I_3 is the third component of weak isospin. The symmetry of the Lagrangian is now considered: what transformations can be made to the fermion states that still leave the Lagrangian invariant? There are two symmetry groups of $\mathcal{L}_{dirac}$, the first is SU(2) symmetry generated from rotations of the left-handed states in isospin space (Eq.1.7) and the second is a U(1) transformation (Eq.1.8):

$$SU(2): \qquad \psi_L \rightarrow e^{\left(\frac{-i}{2}\right)\tau\cdot\alpha}\psi_L, \qquad \psi_R \rightarrow \psi_R \tag{1.7}$$

$$U(1): \qquad \psi_L \rightarrow e^{in\beta}\psi_L, \qquad \psi_R \rightarrow e^{i\beta}\psi_R \tag{1.8}$$

where n in Equation 1.8 is simply a number to account for the fact that the transformation does not have to be the same for left and right-handed states. From Noether's theorem [14] it is known that a conservation law can be derived from global symmetries. Weinberg defined the conserved quantity of U(1) symmetry as weak hypercharge, Y:

$$Y = 2\left(Q - I_3\right) \tag{1.9}$$

It is clear from equations 1.5 and 1.6 that the left-handed fermion states have hypercharge of -1 and the right-handed states have -2, meaning they couple to the hypercharge gauge field with twice the strength of left-handed states. The U(1) transformation can therefore be rewritten as:

$$\psi_L \rightarrow e^{\frac{i\beta}{2}}\psi_L, \qquad \psi_R \rightarrow e^{i\beta}\psi_R \tag{1.10}$$

In order to gauge the theory the ordinary derivative in the Lagrangian must be replaced with the covariant derivatives consistent with SU(2) and U(1) transformations (Eqs. 1.11 and 1.12 respectively):

$$SU(2): \qquad D_\mu \psi_L = \partial \psi_L - \frac{i}{2} g \boldsymbol{\tau} \cdot \boldsymbol{W}_\mu \psi_L \tag{1.11}$$

$$U(1): \qquad D_\mu \psi_L = \partial \psi_L + \frac{i}{2} g' X_\mu \psi_L, \qquad D_\mu \psi_R = \partial \psi_R + i g' X_\mu \psi_R \tag{1.12}$$

Where g and g' are the coupling constants of the SU(2) group and U(1) group respectively. The Lagrangian defined in equation 1.3 can now be written as:

$$\mathcal{L}_{dirac} = i\bar{\psi}_R \gamma^\mu \left(\partial_\mu + i g' X_\mu\right) \psi_R + i\bar{\psi}_L \gamma^\mu \left(\partial_\mu + \frac{i}{2} g' X_\mu - \frac{i}{2} g \boldsymbol{\tau} \cdot \boldsymbol{W}_\mu\right) \psi_L \tag{1.13}$$

In addition to the Dirac Lagrangian the gauge interaction terms must be included:

$$\mathcal{L}_{int} = \mathcal{L}_{dirac} - \frac{1}{4} \boldsymbol{W}_{\mu\nu} \cdot \boldsymbol{W}^{\mu\nu} - \frac{1}{4} X_{\mu\nu} \cdot X^{\mu\nu} \tag{1.14}$$

$$= \mathcal{L}_{dirac} - \frac{1}{4} \left(\partial_\mu \boldsymbol{W}_\nu - \partial_\nu \boldsymbol{W}_\mu - g \boldsymbol{W}_\mu \times \boldsymbol{W}_\nu\right)^2 - \frac{1}{4} \left(\partial_\mu X_\nu - \partial_\nu X_\mu\right)^2 \tag{1.15}$$

The problem with using this Lagrangian to describe electroweak theory is that there are no mass terms for the weak vector bosons. This cannot be solved by simply introducing such terms by hand as it destroys gauge invariance. It was postulated that an interaction with a scalar field, called the Higgs Field, is responsible for breaking the symmetry and endowing the weak bosons and fundamental fermions with mass [12]. In order to give the fermions mass the field must have appropriate quantum numbers to link left-handed and right-handed states. The Higgs field is therefore postulated to be a scalar, isospin doublet of complex fields with $I = \frac{1}{2}, Y = 1$ which can be expressed in terms of four real fields; ϕ_1, ϕ_2, ϕ_3, ϕ_4:

$$\phi = \begin{pmatrix} \phi^+ \\ \phi^0 \end{pmatrix} \qquad = \begin{pmatrix} \phi_3 + i\phi_4 \\ \phi_1 + i\phi_2 \end{pmatrix} \tag{1.16}$$

The following terms should be present in the Higgs Lagrangian:

1. Kinetic term: the covariant derivative of the Higgs field squared.

2. Mass term: term of the order ϕ^2.

3. Self interaction term: the Higgs self interaction term of the order ϕ^4 is required.

4. Higgs-fermion interaction term: the Higgs must couple left-handed fermion states to right-handed ones so terms like $\bar{\psi_L}\phi\psi_R$ must be present in the Higgs Lagrangian.

Putting all the terms together:

$$\mathcal{L}_{higgs} = (D_\mu\phi)^\dagger (D_\mu\phi) - \mu^2\phi^\dagger\phi - \lambda\left(\phi^\dagger\phi\right)^2 - G_e\left(\bar{\psi_L}\phi\psi_R + \bar{\psi_R}\phi^\dagger\psi_L\right) \tag{1.17}$$

where the second term is the mass term, λ is a dimensionless constant and G_e is the coupling constant of Higgs field to electrons and neutrinos.

The minimum in the Higgs potential can be calculated by solving:

$$\frac{\partial}{\partial\phi}\left(\mu^2\phi^\dagger\phi + \lambda\left(\phi^\dagger\phi\right)^2\right) = \mu^2\phi^\dagger + 2\lambda\phi^\dagger\left(\phi^\dagger\phi\right) = 0 \tag{1.18}$$

This gives two possible outcomes depending on whether μ^2 is negative or positive. Exploring the case where $\mu^2 < 0$ gives the following solution for ϕ where potential is at a minimum (Fig. 1.3):

$$\left(\phi^\dagger\phi\right)_0 = \frac{-\mu^2}{2\lambda} = \frac{v^2}{2} \tag{1.19}$$

where v is the non-zero vacuum expectation value of the Higgs potential. A real positive mass for the Higgs Boson has now emerged $M_H\ \alpha\ v\sqrt{\lambda}$.

From equation 1.16, $\phi^\dagger\phi$ can be computed in terms of the real fields:

$$\phi^\dagger\phi = \left(\phi_1^2 + \phi_2^2 + \phi_3^2 + \phi_4^2\right) \tag{1.20}$$

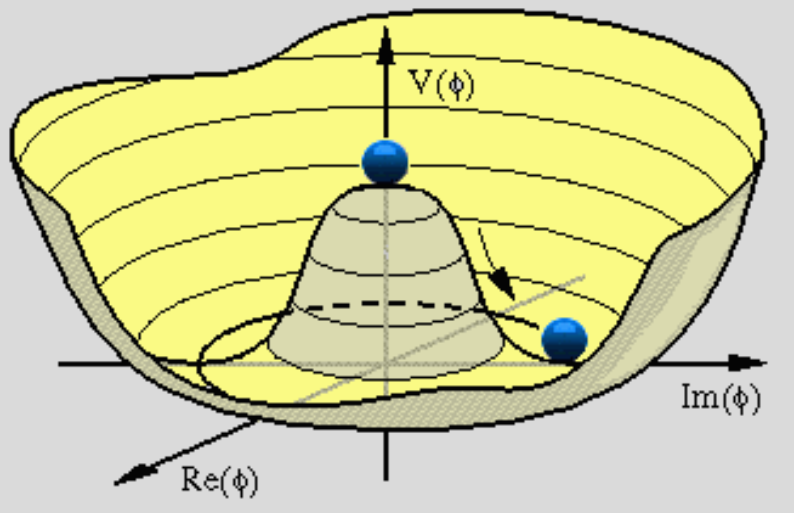

Figure 1.3: The Higgs potential.

Choosing an isospin frame where the ground states of all fields except ϕ_1 are zero:

$$(\phi_1)_0 = \left(-\frac{\mu^2}{2\lambda}\right)^{\frac{1}{2}} = \frac{v}{\sqrt{2}} \tag{1.21}$$

so

$$(\phi)_0 = \frac{1}{\sqrt{2}}\begin{pmatrix}0\\v\end{pmatrix} \tag{1.22}$$

Taking into account the quantum numbers of the Higgs field, the kinetic term can be calculated from the covariant derivative of ϕ:

$$D_\mu\phi = \left(\partial_\mu - \frac{i}{2}g\boldsymbol{\tau}\cdot\boldsymbol{W}_\mu + \frac{i}{2}g'X_\mu\right)\phi \tag{1.23}$$

Performing a perturbative expansion around the minimum in the potential by putting $\phi_1(x) = v + \sigma(x)$ into the covariant derivative of the Higgs field (Eq. 1.23) leads to the following equation:

$$D_\mu\phi = \frac{-i}{\sqrt{2}}\left[\begin{pmatrix} 0 \\ \partial_\mu\sigma \end{pmatrix} - \left[\frac{ig}{2}\begin{pmatrix} W_\mu^3 & W_\mu^1 - iW_\mu^2 \\ W_\mu^1 + iW_\mu^2 & -W_\mu^3 \end{pmatrix} + \frac{ig'}{2}X_\mu\right]\begin{pmatrix} 0 \\ v+\sigma(x) \end{pmatrix}\right]$$
$$= -\frac{i}{2\sqrt{2}}\begin{pmatrix} gv\left(W_\mu^1 - iW_\mu^2\right) + g\sigma\left(W_\mu^1 - iW_\mu^2\right) \\ 2i\partial_\mu\sigma + v\left(-gW_\mu^3 + g'X_\mu\right) + \sigma\left(-gW_\mu^3 + g'X_\mu\right) \end{pmatrix} \tag{1.24}$$

The kinetic term in the Higgs Lagrangian (Eq. 1.17) can be calculated and the masses of the weak bosons can be determined from the coefficients of the field squared terms (terms with higher powers of the fields have not been evaluated as they do not contribute to the masses):

$$\left(D_\mu\phi\right)^\dagger\left(D_\mu\phi\right) = \frac{1}{2}\left(\partial_\mu\phi\right)^2 + \frac{g^2v^2}{8}\left[\left(W_\mu^1\right)^2 + \left(W_\mu^2\right)^2\right] + \frac{v^2}{8}\left(gW_\mu^3 - g'X_\mu\right)^2 + [higher\ order\ terms] \tag{1.25}$$

The W_μ^1 and W_μ^2 fields are associated with the charged weak vector bosons, $W^\pm$. From the third term in Equation 1.25 it can be seen that the theory also predicts a field proportional to $\left(gW_\mu^3 - g'X_\mu\right)$ that has a non-zero mass which is defined as the physical neutral weak boson, Z:

$$Z_\mu = \frac{gW_\mu^3 - g'X_\mu}{\left(g^2 + g'^2\right)^{\frac{1}{2}}} = W_\mu^3\cos\theta_w - X_\mu\sin\theta_w \tag{1.26}$$

where θ_w is the weak mixing angle, otherwise known as the Weinberg angle:

$$\cos\theta_W = \frac{g}{\left(g^2 + g'^2\right)^{\frac{1}{2}}}, \qquad \tan\theta_W = \frac{g'}{g} \tag{1.27}$$

The electromagnetic field A_μ is orthogonal to Z_μ:

$$A_\mu = \frac{g'W_\mu^3 + gX_\mu}{\left(g^2 + g'^2\right)^{\frac{1}{2}}} = W_\mu^3\sin\theta_w + X_\mu\cos\theta_w \tag{1.28}$$

From inspection of Equation 1.25 the masses for the four physical electroweak vector bosons emerge:

$$M_A = 0 \tag{1.29}$$

$$M_{W_1} = M_{W_2} = \frac{gv}{2} \tag{1.30}$$

$$M_Z = \frac{v\left(g'^2 + g^2\right)^{\frac{1}{2}}}{2} \tag{1.31}$$

Putting the expressions for the physical boson fields into the kinetic term in the Lagrangian (Eq. 1.14) the following relationship can be derived:

$$e = g\sin\theta_w = g'\cos\theta_w \tag{1.32}$$

The predictions of the electroweak model were spectacularly confirmed with the first observations of the W and Z bosons at CERN by the UA1 and UA2 collaborations [15], [16], [17], [18].

Masses of the Fermions

The introduction of the Higgs field endows mass to fermions by coupling to both left-handed and right-handed states. This coupling is expressed in the last term in the Higgs Lagrangian (Eq. 1.17):

$$\mathcal{L}_{fermion\ coupling} = -G_e\left[(\bar{\nu_e}\ \bar{e})_L \begin{pmatrix} \phi^+ \\ \phi^0 \end{pmatrix} e_R + \bar{e_R}\left(\phi^-\ \bar{\phi}^0\right)\begin{pmatrix} \nu_e \\ e \end{pmatrix}_L\right] \tag{1.33}$$

When the isospin frame is chosen such that the Higgs field can be expressed as:

$$(\phi)_0 = \frac{1}{\sqrt{2}}\begin{pmatrix} 0 \\ v+\sigma \end{pmatrix} \tag{1.34}$$

$\mathcal{L}_{fermion\ coupling}$ becomes:

$$\mathcal{L}_{fermion\ coupling} = -\frac{G_e v}{\sqrt{2}}\left(\bar{e_L}e_R + \bar{e_R}e_L\right) - \frac{G_e\sigma}{\sqrt{2}}\left(\bar{e_L}e_R + \bar{e_R}e_L\right) \tag{1.35}$$

Replacing $\frac{G_e v}{\sqrt{2}}$ with m_e:

$$\mathcal{L}_{fermion\ coupling} = -m_e \bar{e}e - \frac{m_e}{v}\bar{e}e\sigma \tag{1.36}$$

The interaction with the Higgs field introduces a mass term for electrons (and similarly for the other charged leptons and quarks) whilst keeping the theory gauge invariant and renormalisable.

Electroweak theory with the inclusion of the Higgs mechanism has already had great success predicting the mass of the weak vector bosons. Such bosons will be produced in abundance at the LHC and will prove to be very useful for commissioning of CMS and testing the Standard Model (Section 1.2.3). The LHC will allow experimental elucidation of the EWK symmetry breaking mechanism. Methods for finding the Higgs boson at the LHC are described in Section 1.2.4.

1.2.3 Production of Weak Bosons at the LHC

The production mechanisms of W and Z bosons at the LHC have large cross-sections that are well understood theoretically which make them extremely useful channels for commissioning of the CMS detector and subsequently for investigating possible deviations from the Standard Model. Leptonic decay modes of the weak bosons produce distinctive signatures at hadron colliders [19] and will be very useful for calibrating CMS with early data.

The Drell-Yan process is the dominant mechanism for weak vector boson production at the LHC (Fig. 1.4), where a W or Z is produced by a quark - anti-quark annihilation. Chapter 6 explains in detail the analysis performed with simulated data to study the methods and techniques to be used to measure W and Z cross sections in the electron decay channels [20]. Further information concerning the production and decay of weak vector bosons at the LHC can be found in Ref. [3].

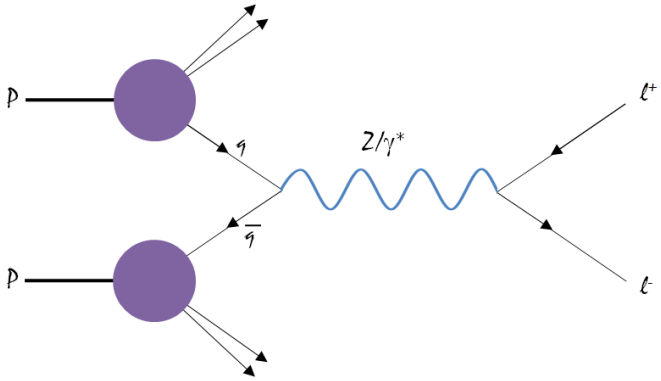

Figure 1.4: Drell-Yan process for producing vector bosons subsequently decaying to leptons.

1.2.4 Production and Decay of Standard Model Higgs Boson at the LHC

The mass of the Higgs boson can be expressed as $M_H \; \alpha \; v\sqrt{\lambda}$ where λ is an unknown constant relating to the Higgs self-interaction (Equation 1.19). Hence, theory does not predict the mass of the Higgs boson; however, lower and upper limits can be placed on it from experimental searches and theoretical arguments.

Upper limits on the Higgs boson mass come from consideration of the energy scale, Λ, at which perturbation theory breaks down in the Standard Model. If the assumption is made that the Standard Model remains weakly interacting all the way up to the Planck scale ($\Lambda \sim 10^{19} GeV$) the Higgs boson mass is constrained to be less than about $180 GeVc^{-2}$. However, there are 'naturalness' arguments against assuming the Standard Model can be extrapolated to energies above the electroweak scale ($\Lambda \sim 1 TeV$); if this scale is taken as the limit, the upper bound on the Higgs boson mass is approximately $700 GeVc^{-2}$ [21].

Theoretical arguments based on the stability of the Higgs potential can be used to establish a lower limit on the mass of the Higgs boson [21]. If it is asserted that the Higgs potential is stable and the Standard Model is valid up to the Planck scale a lower bound on the Higgs mass of approximately $130 GeVc^{-2}$ is calculated. If the Higgs potential is allowed to be metastable this lowers the value to about

$115 GeVc^{-2}$. Unsuccessful searches for the Higgs boson at LEP2 placed a lower limit of $114.4 GeVc^{-2}$ on its mass [22].

If the postulated Higgs boson exists within the mass range predicted then the centre of mass energy at the LHC will be sufficient to find it and confirm the theory. Figure 1.5 shows the leading order mechanisms for producing the Higgs boson. At the LHC the dominant method will be gluon-gluon fusion. The production mechanism with the next highest cross-section is weak vector boson fusion (Fig. 1.6). If the Higgs boson is not found this opens up new theoretical avenues of exploration for the origin of the EWK symmetry breaking mechanism.

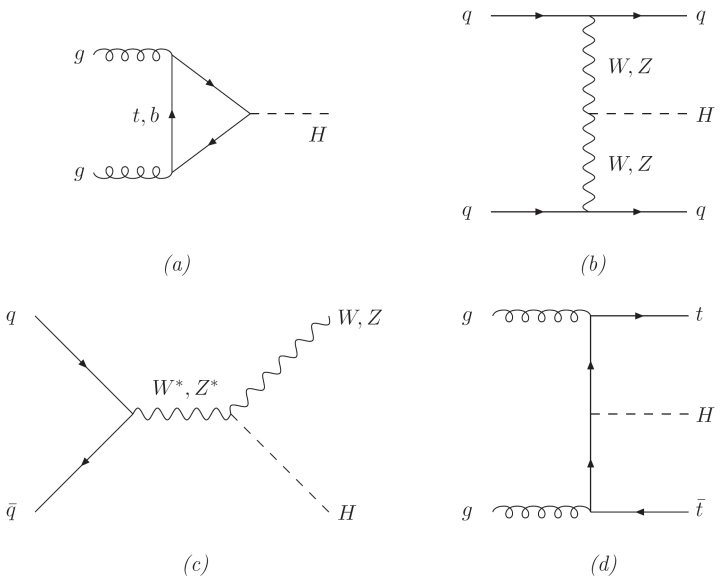

Figure 1.5: Leading order Higgs production mechanisms at the LHC: (a) gluon fusion, (b) vector boson fusion, (c) Higgs-strahlung, (d) Higgs bremsstrahlung off top quarks.

The Standard Model predicts how the Higgs boson will decay depending on its mass (Fig. 1.7). For a Higgs boson mass below about 135 $GeVc^{-2}$ the decay with the largest branching ratio is Higgs to $b\bar{b}$. This decay has a very low signal to background ratio which combined with difficulties in selecting a high purity sample of b-quarks, with high efficiency, makes detection of the Higgs through this decay channel extremely difficult. The next largest branching ratio is Higgs to $\tau^+\tau^-$ but detection of this signal is similarly problematic. A rare but extremely distinctive decay mode in this mass region is Higgs boson to two photons.

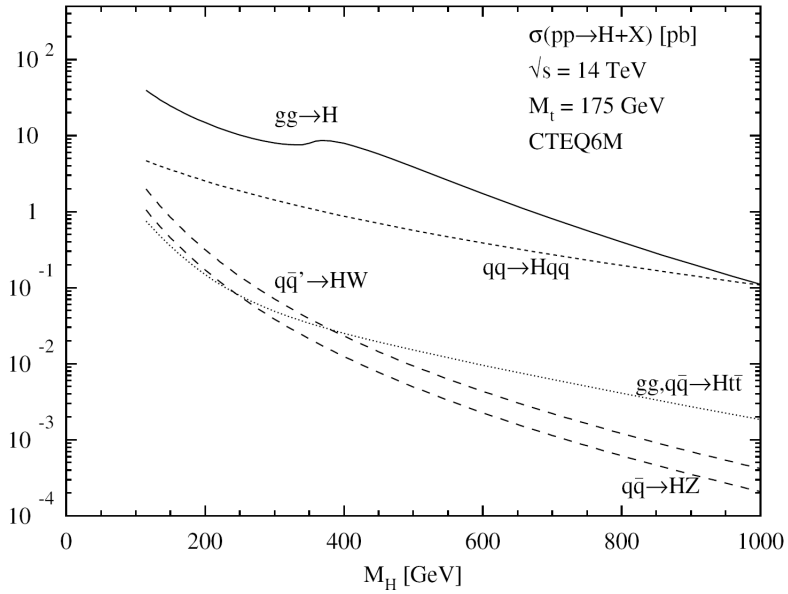

Figure 1.6: Higgs production cross sections at the LHC.

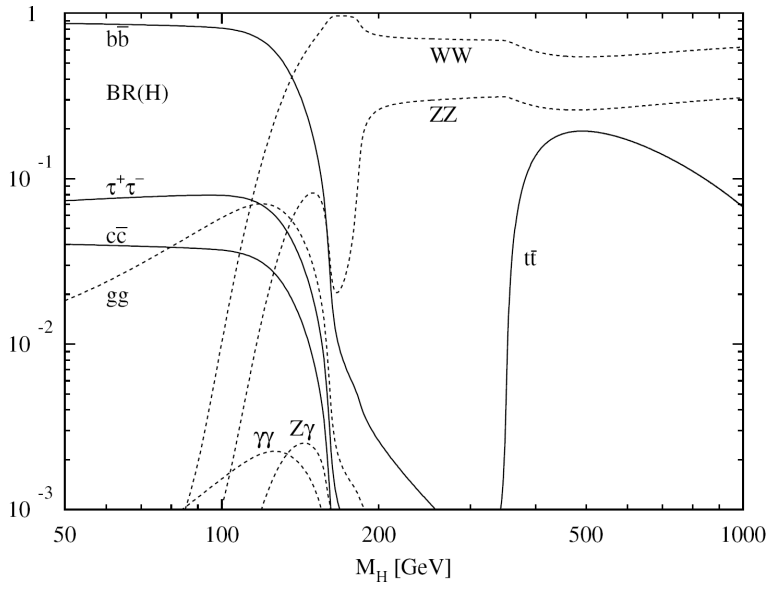

Figure 1.7: Branching ratio of dominant SM Higgs decay modes.

The decay of a Higgs boson with mass above about 135 $GeVc^{-2}$ is dominated by production of two vector bosons. The decay H→ZZ→4l will provide a very clean signal. In the case that both Z bosons are real, the invariant mass of each pair of leptons will be equivalent to the mass of the Z, meaning that stringent cuts can be put on the signal.

Details of Higgs discovery analyses are documented in Refs. [3], [23]. Particular attention is paid in the next section to the $H \rightarrow \gamma\gamma$ decay mode because of its relevance to the ECAL crystal studies conducted by the author and presented in this thesis.

Higgs Decay to Two Photons

The two photon decay mode is considered a very important discovery channel for the Higgs boson [3]. Its signature is two high transverse energy, isolated photons which is extremely distinctive and can be very well reconstructed. However, there are difficulties; this decay has a small branching ratio as the process cannot occur directly because the Higgs boson couples to mass. It is mediated by a virtual top quark or W boson loop (Fig. 1.8). This channel suffers from a very poor signal to background ratio so the Higgs boson can only be detected in this way if the di-photon invariant mass forms a narrow, observable peak above the background. For this to be achieved the photon energy and position resolution must be extremely good, requiring a state of the art electromagnetic calorimeter (ECAL). A large chapter in this thesis is dedicated to the testing of CMS ECAL crystals in order to make sure they meet strict quality criteria to facilitate the required energy resolution.

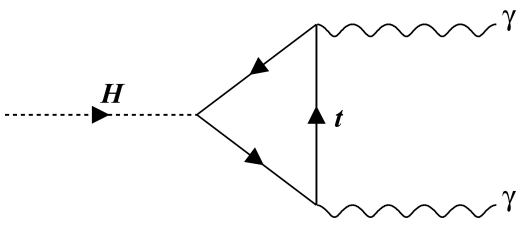

Figure 1.8: Decay of Higgs boson to two photons via virtual top quark loop.

1.2.5 Beyond the Standard Model

Whilst finding the missing piece in the Standard Model, the Higgs boson, would be a momentous achievement, it cannot be the whole story as the model has limitations. It does not include a description of gravity on the quantum scale and cannot explain large variations in the masses of fundamental fermions. Neutrinos are assumed massless in the theory but there is experimental evidence to the contrary [24] and most of the universe is made up of dark matter and dark energy that cannot be fully explained. In fact, the universe would not exist at all without sufficient charge-parity violating interactions that caused matter to dominate significantly over antimatter in the early universe. Whilst such interactions have been observed [25] the effect is not large enough to account for the large dominance of matter. The LHC is expected to shed light on many of these unexplained phenomena and provide a more extensive picture of how nature works.

Unification of Fundamental Forces

Many particle physicists believe that the four fundamental forces might be described as different aspects of the same universal interaction (Fig. 1.9). These forces appear distinct from each other at low energies because they separated out as the universe expanded and cooled. In 1865 James Clerk Maxwell showed that electricity and magnetism were different components of the same force named electromagnetism. The next unification milestone occurred about 100 years later when Weinberg, Salam and Glashow proposed that electromagnetism and the weak force could be treated as different manifestations of the electroweak interaction (Section 1.2.2). Since the conception of this theory it has been experimentally verified with the discovery of the weak bosons [15], [16], [17], [18] and precise measurements [26]. It is expected that this trend will continue to include the unification of the strong interaction and gravity at much higher energy scales than the electroweak. The energy scale at which the strong force is thought to unify with the electroweak is beyond the reach of the LHC. However experimental evidence that the coupling constants of the forces are running to a common value at high energies can be explored.

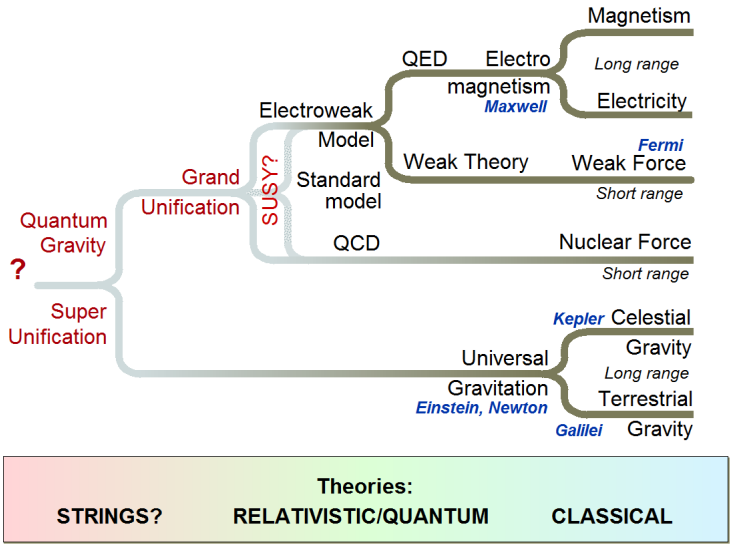

Figure 1.9: Schematic showing the unification of fundamental forces.

1.3 Design, Construction and Operation of the LHC

1.3.1 Overview

The LHC will be supplied with protons (or lead ions) from an existing chain of accelerators (Fig. 1.10). A linac will perform initial acceleration, followed by the Proton Synchrotron (PS) which will provide a $25GeV$ beam for injection into the Super Proton Synchrotron (SPS). The SPS is responsible for further acceleration to $450GeV$, at which stage the charged particles have sufficient momentum to be injected into the LHC. Within the LHC the beams will move around the ring both clockwise and anticlockwise in separate evacuated beam pipes. Acceleration is achieved using very high voltages; cavities allow powerful resonant oscillation causing the protons to gain energy and acceleration continues until the proton beams have an energy of $7TeV$.

The bending required to make the charged particles move in a circle is provided by superconducting dipole magnets [27]. These magnets have been designed to operate at $1.9K$ and keeping them at this temperature requires a huge cryogenics system which essentially involves immersing the magnets in superfluid helium.

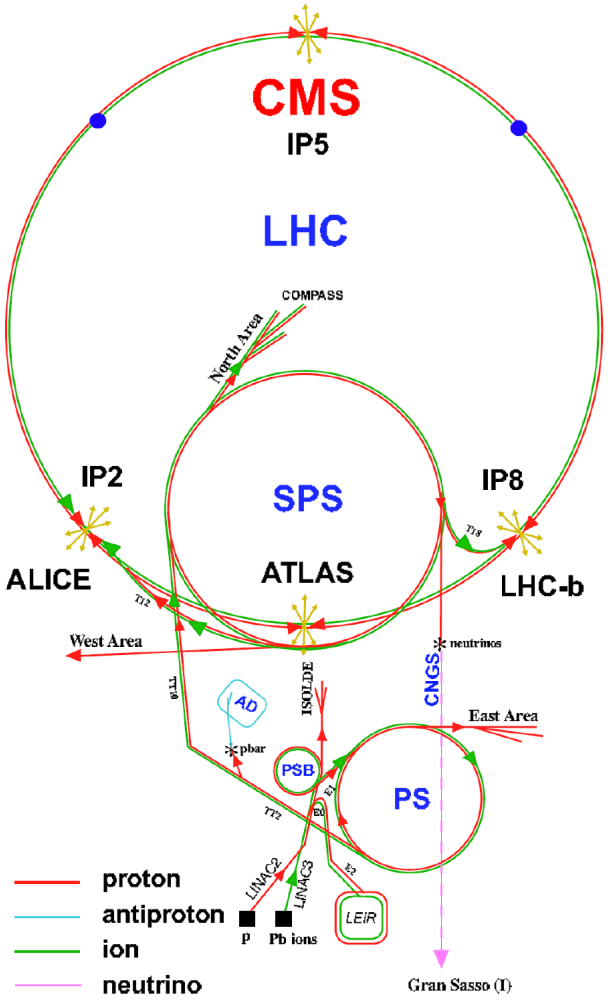

Figure 1.10: Layout of CERN accelerator complex showing the position of each LHC experiment and the chain of injectors into LHC.

1.3.2 Beam structure and Collisions

The beam consists of bunches of protons which, at design luminosity ($10^{34} cm^{-2} s^{-1}$), contain 1.15×10^{11} particles at the start of a fill and each beam will contain 2808 bunches. The bunches themselves are ellipsoidal in shape with a Gaussian width of $16\mu m$ and $23\mu m$ in the x and y directions respectively and $8cm$ parallel to the beam pipe (when the beam is at $7TeV$). These bunches are much more compact than in previous hadron accelerators [28]. At design luminosity bunches of protons will be brought into contact every $25ns$ and on average each bunch crossing will result in about twenty inelastic collisions. Such a small time interval between bunch crossings has imposed tough constraints on the design of detectors; every element must respond rapidly, have high granularity and good time resolution.

Chapter 2

Compact Muon Solenoid

To study accurately the fleeting particles that will be produced when the LHC beams collide, as much information as possible must be gathered about the products they decay into. Precise particle detecting and measuring devices have therefore been built at each collision point at the LHC. The Compact Muon Solenoid (CMS) is such a device (Fig. 2.1). It is a highly complicated, general purpose particle detector that has been designed and constructed over the last 15 years. The main design goals for CMS were:

- A high performance muon system.
- The best possible electromagnetic calorimeter.
- High quality central tracking.
- Hadron calorimetry with sufficient energy resolution and good hermiticity.
- Financially affordable.

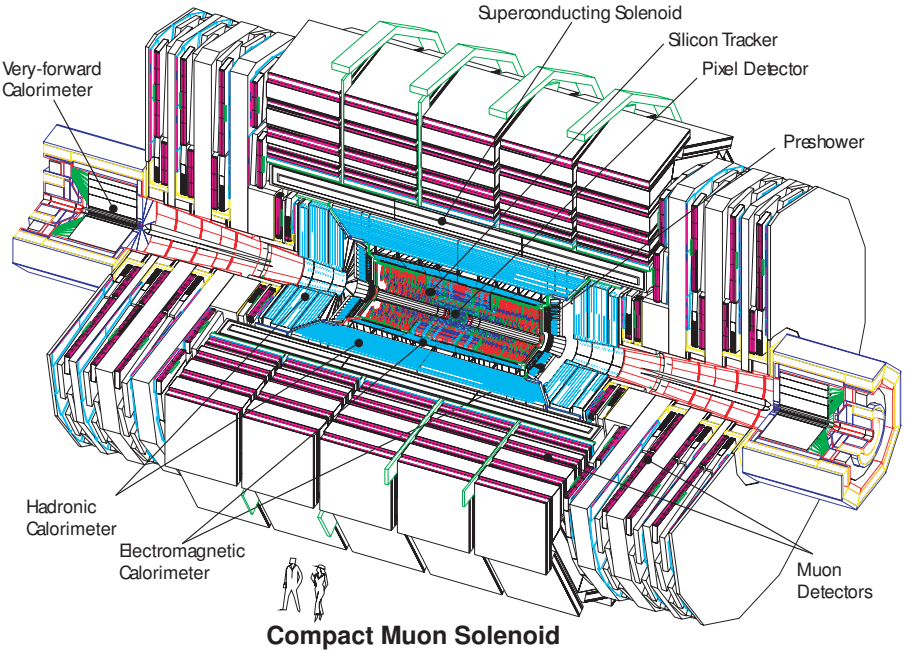

Figure 2.1: Schematic of CMS.

2.1 Overview of CMS

CMS is constructed in cylindrical layers and consists of a barrel section closed at each end with endcap discs (Figs. 2.2 and 2.3). CMS has been designed to have good hermetic coverage to minimise the fraction of particles escaping detection. The right-handed coordinate system has the origin placed at the nominal interaction point: the x-axis points toward the centre of the LHC, the y-axis points vertically upwards and the z-axis points along the direction of the beam. The azimuthal angle, ϕ, is the angle with respect to the x-axis in the x-y plane. The radius in this plane is defined as: $r = \sqrt{x^2 + y^2}$. The polar angle, θ, is the angle from the z-axis. However, pseudorapidity (defined as $\eta = -\ln[\tan(\theta/2)]$) is used as it is Lorentz invariant at high particle energies. The momentum transverse to the beam axis is an important quantity in particle physics and can be calculated using the following equations:

$$P_T = \sqrt{\left(P_x^2 + P_y^2\right)} = \frac{P}{\cosh \eta} \tag{2.1}$$

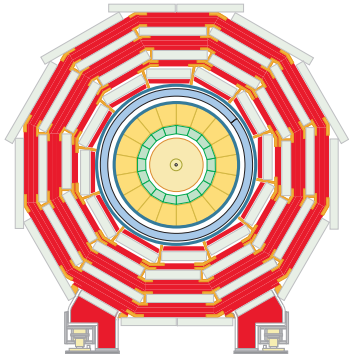

Figure 2.2: Transverse slice through CMS.

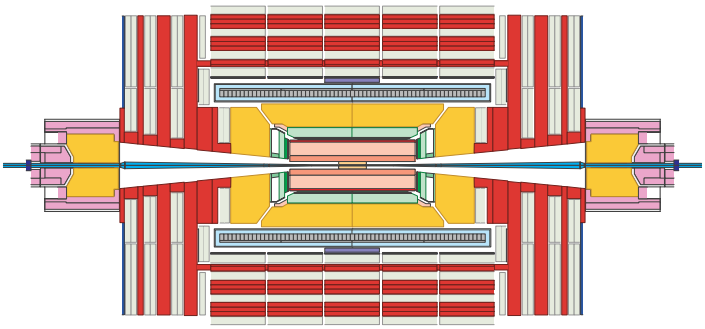

Figure 2.3: Longitudinal slice through CMS.

From the beam pipe outward the component sub-detectors are: silicon tracker, electromagnetic calorimeter (ECAL), hadron calorimeter (HCAL), superconducting solenoidal magnet, outer barrel HCAL, muon chambers and iron return yoke. The silicon pixel detector surrounds the interaction region to improve the measurement of charged particles produced from the decay of extremely short-lived particles. Directly outside this lies a silicon microstrip detector comprising layers of sensors in both barrel and endcap regions. The next layer is the ECAL which consists of about 76,000 scintillating crystals made of lead tungstate. This measures the energy of electrons and photons with extremely good resolution. Immediately surrounding the ECAL are the inner barrel and endcap regions of the HCAL which measures the energy of hadronic particles produced in CMS. It is a sampling calorimeter made from alternate layers of brass absorber and plastic scintillator and provides good spatial and adequate energy resolution. All these components are confined within a superconducting solenoid that will produce a 4 Tesla field.

Some extra layers of scintillator are placed immediately outside the solenoid in the barrel region to catch the tails of hadronic showers. The outer region of CMS consists of the muon chambers and the iron return yoke. Two forward hadron calorimeters (HF) are placed at small angles to the beam pipe outside the main body of CMS to increase the acceptance of the detector, to tag forward jets and to improve the measurement of missing transverse energy.

Each subdetector is described in more detail in the subsequent sections in this chapter with particular attention paid to the ECAL due to its relevance to this thesis.

2.2 The Silicon Tracker

The high beam energy and luminosity at the LHC place huge demands on the design of the CMS tracker. The tracker must measure trajectories of charged particles very precisely, with high efficiency. Particles that decay very rapidly, such as heavy quarks and τ leptons, will be produced in many LHC collisions and are a good indication of interesting physics. Identification of such particles requires precise reconstruction of secondary vertices.

As with all detector elements at the LHC, a fast response time is essential in view of the $25ns$ bunch crossing interval which places strict constraints on the sensor materials and electronics. The intense flux of particles produced can cause radiation damage so all tracker components are radiation hard enough to operate well in the harsh environment for at least 10 years of LHC running.

The CMS tracker is made entirely of silicon sensors in order to meet all the requirements placed on it, including excellent position resolution [29]. A schematic of its layout is shown in Fig. 2.4. The tracker extends to a radius of 1.1m and is composed of ten detection layers in the barrel and twelve discs in each endcap. It is made of silicon mircostrips and extends to $|\eta|$ of 2.5.

In the region immediately surrounding the interaction point many overlapping particle tracks will be present which requires a very high granularity in order to keep the occupancy low. Good spatial resolution is also necessary to measure the position of secondary vertices precisely so a silicon pixel detector has been chosen for this region and sits inside the microstrip detector. It is composed of three barrel layers at a transverse distances of 4.4cm, 7.3cm and 10.2cm, and it is closed at both ends by two endcap discs.

2.3 The Hadron Calorimeter

The hadron calorimeter (HCAL) [30] measures the energy of hadronic particles produced in CMS. It needs adequate spatial and energy resolution, but more impor-

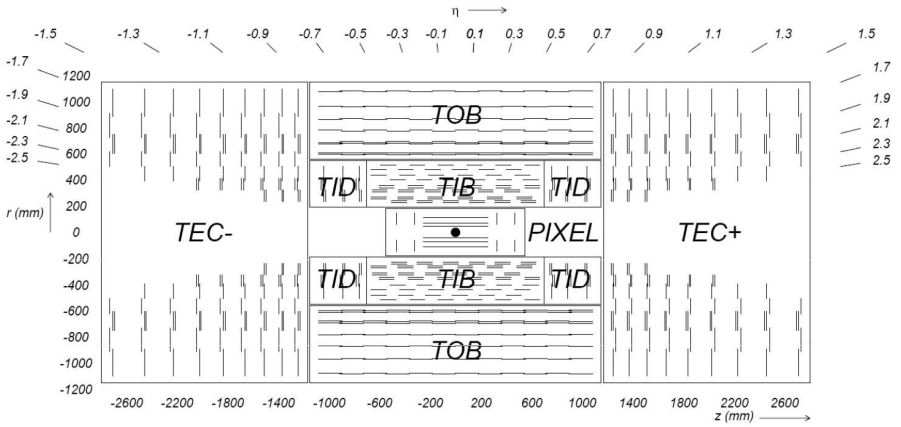

Figure 2.4: Schematic of CMS tracker.

tantly should have good hermetic coverage. This is necessary for precise measurement of the missing transverse energy, which is an important quantity for inferring the presence of neutrinos or other possible particles that do not interact with the detector.

Figure 2.5 shows the various regions of the HCAL. The main part of the barrel calorimeters (HB) is placed just inside the magnet. To ensure that energy from hadronic showers does not leak from the back of the HCAL, outer barrel calorimeters (HO) are placed immediately outside the magnet increasing the combined depth of the ECAL and HCAL to at least eleven interaction lengths. The endcap calorimeters (HE) are positioned behind the ECAL endcaps. To increase the hermetic coverage further, forward hadron calorimeters (HF) are located close to the beam pipe outside the muon system extending the $|\eta|$ range from 3 to 5.2.

With the exception of HF, the HCAL is a sampling calorimeter constructed of alternating layers of brass absorber (5-8cm thick) and plastic scintillator (3.7mm thick). The scintillator is comprised of sixteen η segments, each with a size of $\Delta\eta \times \Delta\phi = 0.087 \times 0.087$ in the $|\eta| < 2$ region.

The forward hadron calorimeters (HF) must cope with an extreme radiation environment. The main consideration when designing these detectors was to select a material that could withstand huge particle fluxes for at least ten years. For this

reason quartz fibres were chosen for use as the active medium and are inserted into steel absorber plates.

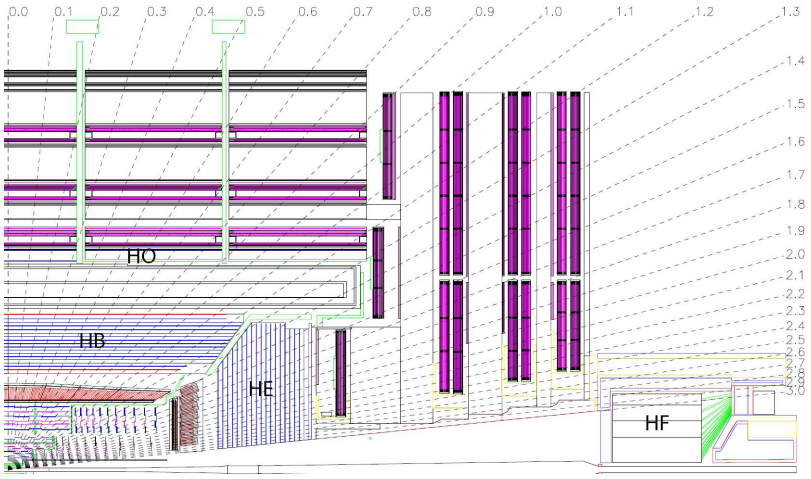

Figure 2.5: Schematic of CMS showing the various regions of the HCAL, lines represent constant η.

2.4 The Magnet

The magnet at the heart of CMS is, in terms of energy stored, the largest superconducting solenoid ever constructed [31]. It will provide a strong field of almost $4T$ over the inner tracking and calorimetry regions. Such a large field is necessary to make highly energetic charged particles bend enough to measure their momentum precisely. The magnetic flux is returned using $10,000t$ of iron which also provides a support structure for the muon chambers. The inner diameter of the magnet bore is $6.3m$ and its length is $13.5m$, the return yoke extends to 14m in diameter. Figure 2.6 shows a schematic of the CMS solenoid and a picture of it inserted into the central slice of CMS.

2.5 The Muon Chambers

Muons are relatively straightforward to detect because they are highly penetrating which makes them almost background free. Muons are produced in the decay

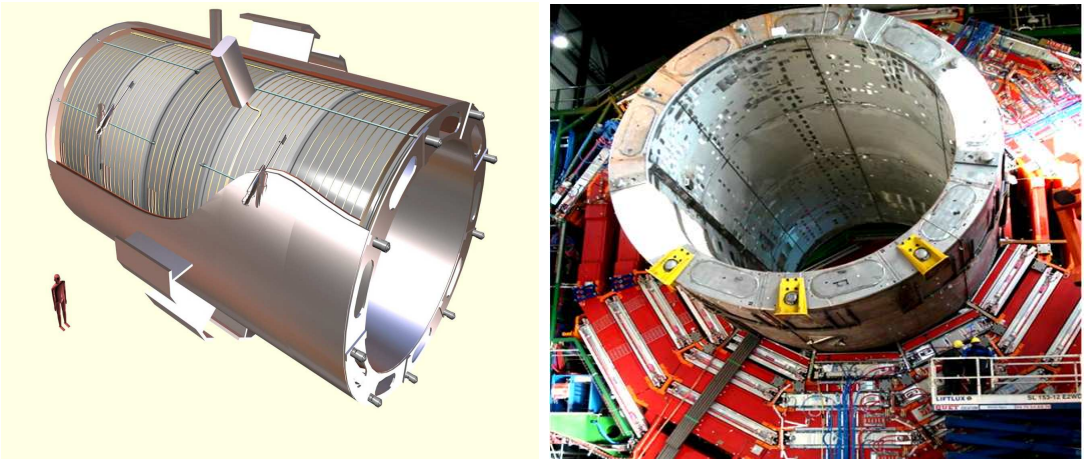

Figure 2.6: The CMS solenoidal magnet.

of many interesting particles, the Higgs boson being a very good example of this [3], so it is important to be able to reconstruct them efficiently. In order to fully exploit these properties of muons, it was decided from the very outset that CMS must be equipped with a muon tracking system that can perform robust measurement of muons sufficiently precise to allow good stand-alone measurement of muon momentum [32].

Drift tubes (DT) are used in the barrel to detect muons in the region $|\eta| < 1.2$. In the two CMS endcaps, cathode strip chambers (CSC) are used to cover the pseudorapidity range $0.9 < |\eta| < 2.4$. CSCs cope well with the high radiation rates and non-uniform magnetic field present in the endcaps. Muon identification is possible over a θ range from 10 to 170 degrees. When the muon system is used in conjunction with the inner tracker a good muon momentum resolution can be achieved ($\sim 5\%$ for a 1 TeV momentum track).

The muon system is also equipped with a dedicated trigger system in the form of resistive plate chambers (RPC). They are positioned in both barrel and endcap regions, up to $|\eta|$ of 1.6, and have a very fast response time of approximately $1ns$ making them ideal for contributing to quick triggering decisions.

2.6 The Trigger System

One of the main challenges at hadron colliders is to select interesting physics events whilst discarding others. At the LHC this is of paramount importance due to the high rate at which collisions will occur. The crossing frequency of the proton beams is $40MHz$ and each crossing could produce as many as twenty proton-proton collisions at high luminosity. Only a small fraction of this information can be read out and stored, which requires LHC detectors to employ complex, dedicated trigger systems.

The CMS trigger consists of two main stages in order to achieve high efficiency:

1. Level 1 trigger (L1T): custom designed programmable electronics
2. High level trigger (HLT): software system implemented on a filter farm

The job of the L1T is to make quick decisions and pass potentially interesting physics events to the next stage whilst applying tight enough criteria to reduce the event rate from $40MHz$ to a maximum of $100kHz$. The need for a speedy response means that the L1T is based on coarse calorimeter and muon chamber information only. All event data are stored in pipelines for $3.2\mu s$. If the L1T is fired then the high resolution information gets passed to the HLT. A L1T fail means the data stored in the pipelines is overwritten by new data.

The L1T is subdivided into three main subsystems:

1. L1 calorimeter trigger
2. L1 muon trigger
3. L1 global trigger

The L1 calorimeter trigger is described in more detail in the next section, further information concerning the muon triggers can be found in Ref. [33].

2.6.1 Level 1 Calorimeter Trigger

For the purposes of triggering, the calorimeters are divided into sections called trigger towers, the majority having a size of $\Delta\eta \times \Delta\phi = 0.087 \times 0.087$. Trigger primitive generators (TPG) sum the transverse energy in the ECAL and HCAL to give the total value for the tower and calculate the lateral extent of the electromagnetic energy deposit in the ECAL. The TPs are subsequently transmitted to the regional calorimeter trigger (RCT) which combines information from 4×4 trigger towers. This stage of the trigger determines electron and photon candidates, and calculates the transverse energy for the calorimeter region. The global calorimeter trigger (GCT) uses the information provided by the RCT to determine the highest rank calorimeter objects across the whole detector. At this stage event variables such as total transverse energy and missing transverse energy are computed.

Event information from the global calorimeter trigger is combined with that from the global muon trigger, and it is at this stage where the overall L1T decision is made. Events passing L1T are passed to the HLT for further scrutiny.

2.6.2 High Level Trigger

The HLT has access to full information from events that pass L1T and is designed to perform complex and detailed online calculations on a farm of standard processor units. The HLT is required to pick out events with the most interesting physics content whilst reducing the rate further to approximately $100Hz$. Events passing the HLT are stored and made available for offline analyses. More detail of the algorithms used in the HLT for electron and photon selection are given in Ref. [34].

2.7 The Electromagnetic Calorimeter

The purpose of the CMS ECAL (Fig. 2.7) is to measure the energy of electromagnetic showers with very good resolution. It has a fast response, fine granularity and is radiation hard. The ECAL is constructed of scintillating lead tungstate crystals.

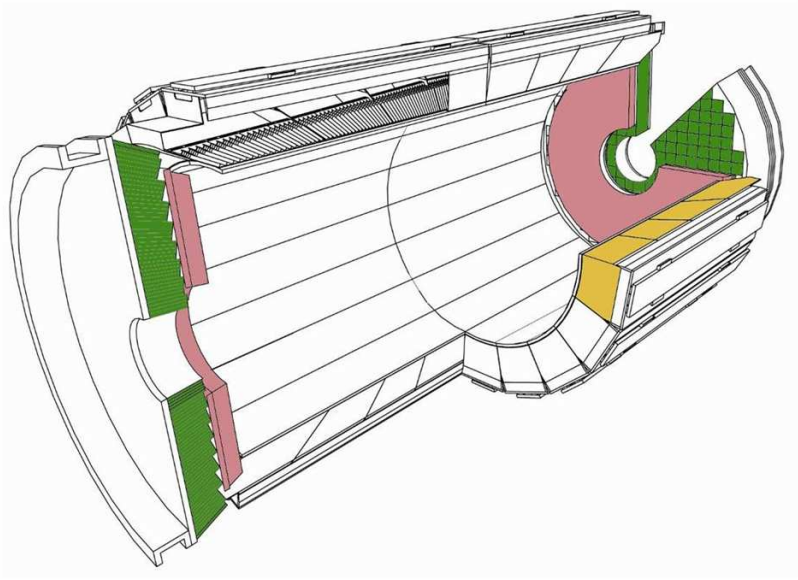

Figure 2.7: Schematic of the CMS ECAL.

A detailed schematic of a quadrant of the ECAL is shown in Figure 2.8. The barrel region consists of about 61,000 crystals contained in 36 modules, 18 in each half of the detector, and covers a range of $-1.48 < \eta < 1.48$. The exact size of barrel crystals is dependent on pseudorapidity. A typical crystal has a front face of $\sim 2.2cm \times 2.3cm$ and a rear face of $\sim 2.5cm \times 2.6cm$ with a length of $23cm$. The supermodules have a width of 20 crystals in the ϕ direction and are divided into four modules in the η direction with widths of 25 crystals for module 1 and 20 for modules 2,3 and 4. Each module is further divided into submodules, consisting of 2×5 crystals in ϕ and η directions respectively, held in a glass fibre structure called and alveolar.

The endcaps are made of four dees with each endcap containing about 7,300 crystals, covering a range of $1.48 < |\eta| < 3$ (Fig. 2.8). All endcap crystals are the same size and shape with a front face of $2.86cm \times 2.86cm$ and a rear face of $3cm \times 3cm$ and a length of $22cm$. They are grouped into supercrystals of 5×5 crystals held in carbon fibre alveolar. Figure 2.9 shows photographs of the barrel and endcap ECAL.

Photodetectors collect and amplify the scintillation light produced by electromagnetic showers in the crystals. Avalanche photodiodes (APD) are used in the barrel and vacuum phototriodes (VPT) in the endcaps. Figure 2.10 shows a barrel and an endcap crystal with attached photodetectors.

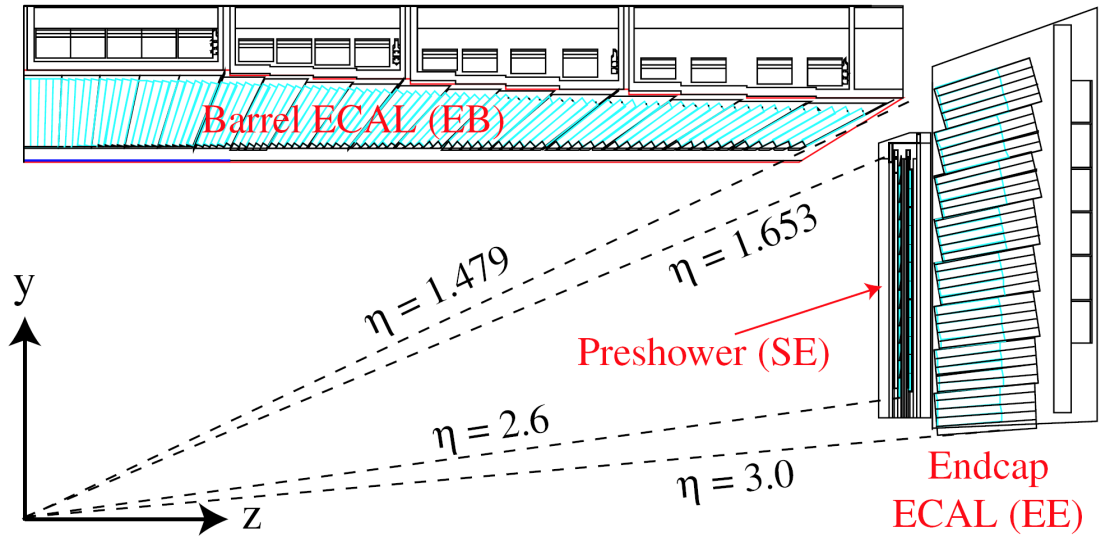

Figure 2.8: Longitudinal schematic of a quarter of the CMS ECAL.

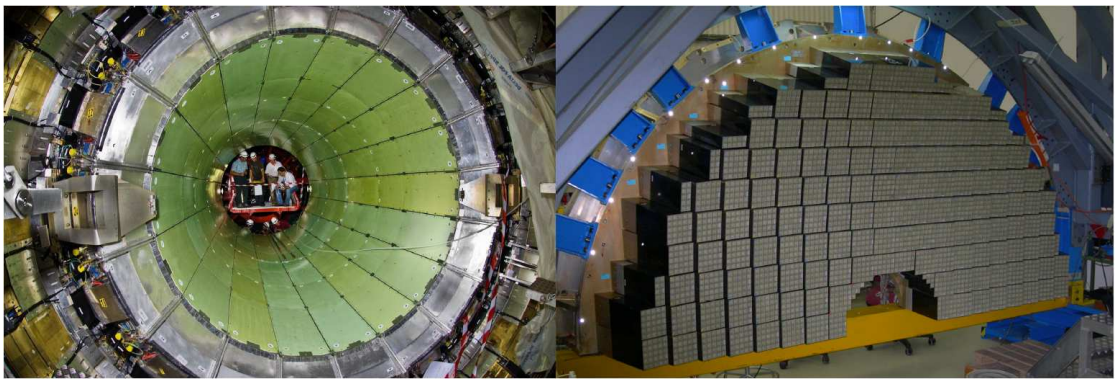

Figure 2.9: Photographs showing the barrel supermodules inserted inside the HCAL (left) and one endcap dee with mounted supercrystals (right).

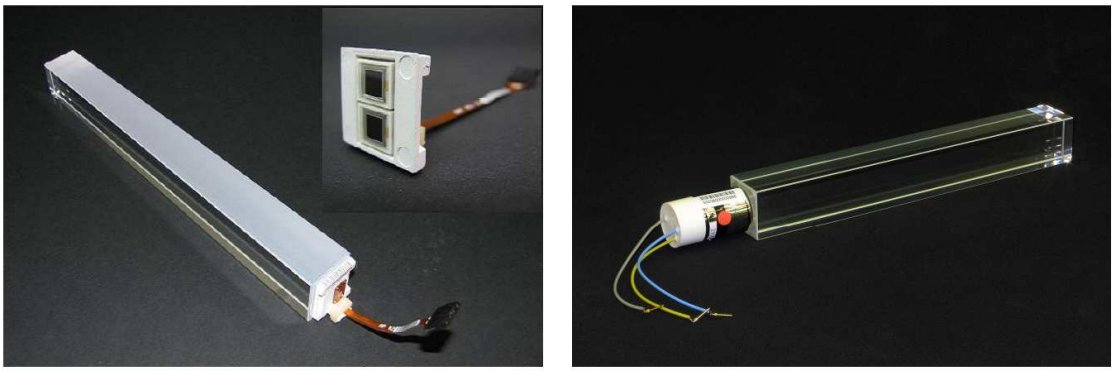

Figure 2.10: Photographs of CMS ECAL barrel (left) and endcap (right) crystals with attached photodetectors.

The ECAL is designed to operate at $18°C$. This is an attainable temperature at which the crystal light yield is acceptable. In order to achieve the desired energy resolution the temperature must be kept constant to within $\pm$ 0.1 degrees because the amount of scintillation light changes with temperature.

Crystals constituting the barrel region are approximately 26 radiation lengths (X_0) long (Fig. 2.10), while endcap crystals are about a radiation length shorter due to the presence of a preshower which contributes an extra $2.8X_0$ in front of the endcap. The angle of the crystals with respect to the cylindrical radius increases the further they are away from the interaction region. Crystals have a pseudo-pointing geometry illustrated in Fig. 2.8 meaning the principal axes of the crystals are off pointing by an angle of 3° with respect to the interaction point in both η and ϕ directions.

2.7.1 ECAL Energy Resolution

The energy resolution of the ECAL is given by the following formula:

$$\frac{\sigma}{E} = \frac{a}{\sqrt{E}} \oplus \frac{b}{E} \oplus c \tag{2.2}$$

where a is the stochastic term, b is the noise term and c is a constant term that dominates the energy resolution at high energy. Table 2.1 displays the targets for each term in Equation 2.2 and contributions to the constant term are discussed [35].

Parameter	Barrel $\eta = 0$	Endcap $\eta = 2$
Stochastic Term	$\frac{2.7\%}{\sqrt{E}}$	$\frac{5.7\%}{\sqrt{E}}$
Noise Term (High Luminosity)	210MeV	E_T = 245MeV
Constant Term	0.5%	0.5%

Table 2.1: Design goals for each term contributing to the ECAL energy resolution. Noise term includes contributions from electronics noise, leakage current and pile-up.

A limit of 0.5% is the collaboration's goal for the constant term so that Higgs boson to two photon decay mode can be observed as a narrow mass peak above the background. The following effects contribute to this term:

- Crystal to crystal inter-calibration errors.
- Non-uniformity of longitudinal light collection.
- Energy leakage through the rear of the crystal.
- Imperfections in calorimeter construction.

Furthermore, changes in transparency due to irradiation must be monitored in situ and corrected for to achieve the required energy resolution.

2.7.2 Monitoring the Crystals Online

Crystals will be monitored in situ using a laser monitoring system. Laser pulses injected into every crystal map changes in transparency caused by radiation damage. This information will be used to correct the energy response of the crystals by taking into account how damaged each crystal was at the time of the measurement.

2.7.3 The Endcap Preshower Detector

The main reducible background to the signal $H \rightarrow \gamma\gamma$ is neutral pions faking single photons. In the barrel the granularity of the crystals is sufficient to distinguish the two photons produced in a π^0 decay. However, at higher pseudorapidity the photons will have a smaller separation at the ECAL surface. Because of this, a silicon preshower detector will be located in front of the ECAL endcap (Fig. 2.8) to increase the neutral pion rejection by having sufficient granularity to resolve the two close photons from a π^0 decay. The presence of the preshower contributes 2.8 radiation lengths so endcap crystals are shorter than barrel crystals and suffer similar amounts of longitudinal leakage.

Chapter 3

Irradiation Studies on CMS ECAL Crystals

In this chapter the properties of lead tungstate crystals used to construct the CMS ECAL are discussed in detail and particular attention is paid to the effect of irradiation on these crystals. Methods and results of measurements conducted at Imperial College CMS crystal laboratory and also at the research centre ENEA during 2005 are presented.

3.1 Lead Tungstate Crystals

The CMS electromagnetic calorimeter has been designed and constructed to provide the best possible energy resolution. It also must respond quickly and be radiation hard. Lead tungstate was chosen for use in the CMS ECAL for the following reasons:

- Intrinsic radiation hardness; crystals will be required to operate well after receiving an integrated radiation dose over at least 10 years operation of CMS.
- Short radiation length ($0.89cm$); crystals need to be short enough for the ECAL to fit inside the solenoid to fulfill the objective that CMS is compact.

- Small Molière radius ($2.2cm$); narrow showers are advantageous and transverse crystal dimensions were decided upon so that most of the energy from an electromagnetic shower is contained within one crystal.
- Short scintillation time; bunch crossings occur every $25ns$ at LHC so a fast response is vital.

The main disadvantage of using lead tungstate is its low light yield [36]. Fortunately this can be compensated for by using advanced photodetectors that can provide gain and operate in high magnetic fields.

3.1.1 Crystal Suppliers

Lead tungstate crystals for the CMS ECAL were produced by the Bogoroditsk Techno-Chemical Plant (BTCP) in Russia. To ensure the required number were produced on time a second supplier was enlisted, namely the Shanghai Institute of Ceramics (SIC). In 2004 and 2005 SIC produced batches of preproduction endcap crystals (Table 3.1) that needed to be tested in order to check they met specifications imposed to achieve the required ECAL energy resolution (Section 2.7.1).

Batch No	Crystals in Batch	Month Produced
0	2568-2617	January 2004
1	2659-2708	November 2004
2	2709-2758	November 2004
3	2759-2808	December 2004
4	2809-2858	January 2005
5	2859-2908	January 2005
6	2909-2958	February 2005

Table 3.1: Details of SIC endcap crystals produced.

Three main measurements were carried out to test the quality of crystals:

1. Radiation hardness: quantified by light yield decrease and induced absorption coefficient (μ) as a result of irradiation.

2. Changes in transparency: corrections depend on the ratio of change in scintillation light to change in monitoring signal (R).

3. Uniformity of crystal light yield in the region of shower maximum: quantified by front non-uniformity (FNUF).

Each of these points is explained in detail in the next three sections.

3.1.2 Radiation Damage in Lead Tungstate

During CMS operation the crystals, particularly those in the endcaps, will be subject to high ionising radiation dose rates (Table 1 in Appendix A). The effect of radiation on lead tungstate has been studied [37]; it results in a decrease in optical transmission and hence light yield. Figure 3.1 shows a simulation of crystal transparency evolution at LHC based on test beam irradiation results.

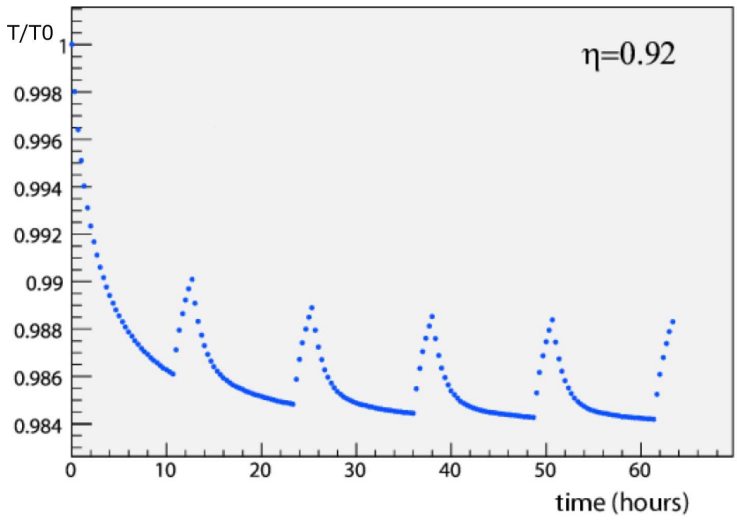

Figure 3.1: Simulation of changes in crystal transparency normalised to pre irradiation transmission for $\eta = 0.92$ and LHC luminosity of $2 \times 10^{33} cm^{-2} s^{-1}$.

The scintillation mechanism of lead tungstate* is not appreciably affected by exposure to radiation, making it intrinsically radiation hard. Another important prop-

*Lead tungstate crystals produce scintillation light at three main wavelengths, two of which appear green and one blue. The light is produced due to energy transfer between lead anions and tungstate groups; for a more detailed explanation see Ref. [38]. The resulting spectrum is a convolution of the individual spectra produced by the three transitions. The spectrum peaks at 420nm and is negligible below about 310nm and above about 600nm.

erty of lead tungstate is good transmission over the wavelength range of its emission spectrum (Fig. 3.2).

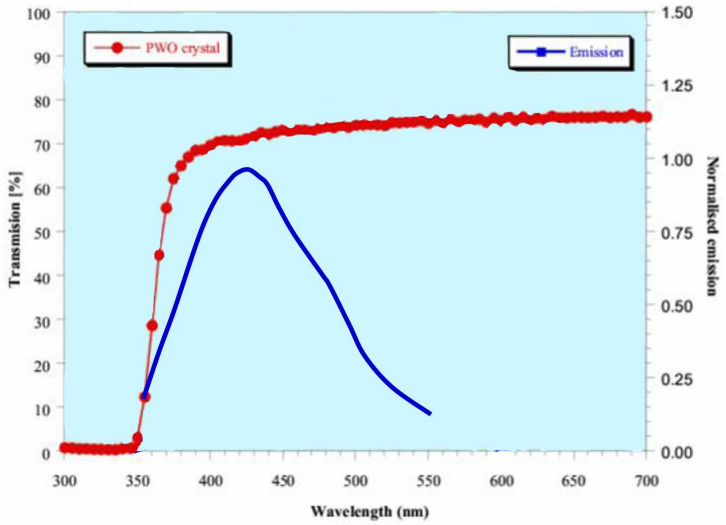

Figure 3.2: Emission and longitudinal transmission of lead tungstate crystals.

Radiation induced decrease in transmission is attributed to the production of colour centres which lead to the appearance of absorption bands. Colour centres are created by a change in charge state of existing point defects in the crystal lattice and are produced by γ radiation exposure[†] in the following three step process [39] :

1. Creation of hot electron-hole pairs.
2. Cooling down and diffusion of separated electrons and holes.
3. Thermalised electrons and holes are fixed in suitable lattice sites.

During irradiation, colour centres are continually created and annihilated. When all pre-existing defects are filled, saturation is reached and no further colour centres will appear. The kinetics of colour centre formation have been modelled and the relative influence of different types of centres has been investigated [40]. The model assumes that existing defects are distributed randomly throughout the crystal, they do not interact with one another and the density of each type of defect is much

[†]The creation of new defects in the lattice caused by radiation or neutron fluence is negligible.

smaller than the density of lattice atoms. The rate of change of colour centres is given by the following equation:

$$\frac{dN_i}{dt} = -\omega_i N_i + \frac{S}{d_i}(N_i^* - N_i) \tag{3.1}$$

where N_i is the density of colour centres of type i at time t , ω_i is the recovery rate of the damaged centres of type i, S is the rate of irradiation in Gy/hr, N_i^* is the density of pre-existing defects of type i and d_i is a damage constant for centre type i.

The model takes into account a number of different types of centre with distinct recovery time and damage constants. The total density is given by summing over all centre types:

$$N = \sum_i N_i^* \frac{S}{S + \omega_i d_i}\{1 - exp[-(\omega_i + \frac{S}{d_i})t]\} \tag{3.2}$$

Equation 3.2 describes the development of centres during irradiation. When irradiation ceases these centres recover at a rate dependent on the time constant for that type of defect. The following equation describes the change in density of colour centres with time post-irradiation:

$$N = \sum_i N_i^* \frac{S}{S + \omega_i d_i}\{1 - exp[-(\omega_i + \frac{S}{d_i})t_0]\}exp(-\omega_i[t - t_0]) \tag{3.3}$$

where t_0 marks the end of the irradiation period.

The amount of damage to a crystal is often quantified by its induced absorption coefficient μ, given by $\mu = \sigma N$, where σ is the cross-section of the centre. The parameter μ is a quantity that describes how much light a crystal absorbs as a result of the radiation damage it has received. From Equation 3.3 it follows that:

$$\mu = \sum_i \mu_i^{sat} \frac{S}{S + \omega_i d_i}\{1 - exp[-(\omega_i + \frac{S}{d_i})t_0]\}exp(-\omega_i[t - t_0]) \tag{3.4}$$

where $\mu^{sat} = \sigma N^*$ is the saturated induced absorption coefficient and has the units m^{-1}.

Figure 3.3 shows how μ changes with time during and after irradiation for colour centres with five different recovery time constants. The plot has been produced by the author using the model in Ref. [40] with the radiation dose rate, S, set to $7Gy/hr$ as this is typical of the ECAL endcaps. It can be inferred from Figure

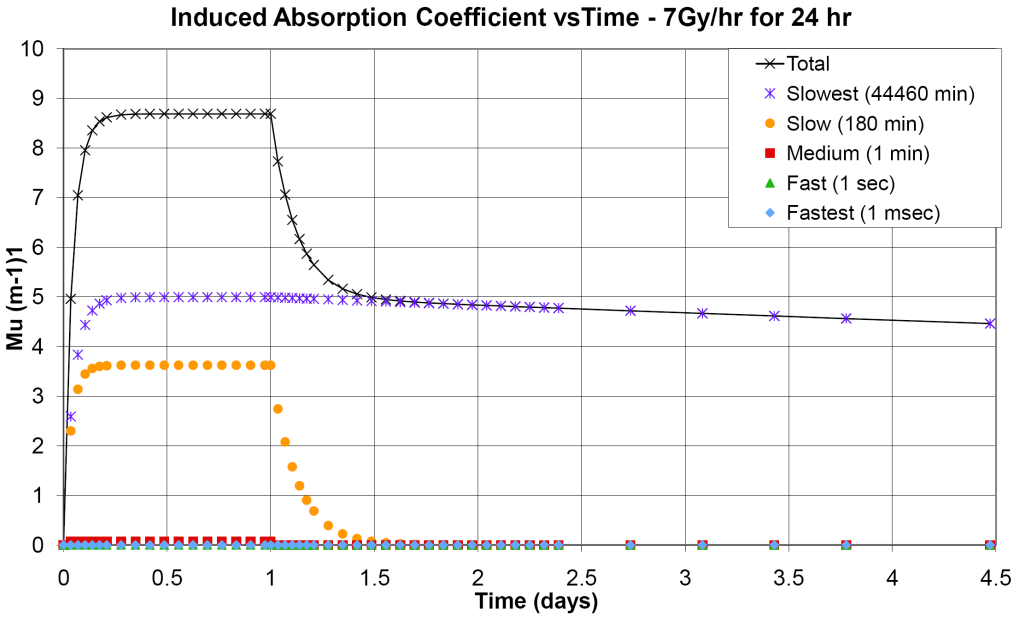

Figure 3.3: Induced absorption coefficient variation with time during and post irradiation for a dose rate of $7Gy/hr$ for 24 hours.

3.3 that the slower the recovery time constant of the colour centre, the larger the contribution to the induced absorption coefficient.

Measurement of the induced absorption coefficient of a crystal irradiated with doses typical of those during CMS operation is an important quantity. If a crystal damages too easily it is not suitable for use in CMS because the energy resolution will be unacceptably degraded by the following effects:

- Poor light collection uniformity due to short attenuation length.
- Loss of linearity in the relationship between light yield and monitoring signal.
- Poor photo-statistics due to increased absorption of scintillation light.

Radiation hardness can also be quantified by the percentage light yield loss after irradiation with respect to its pre irradiation value. Measurements of induced absorption coefficient and light yield decrease are detailed in this chapter.

3.1.3 Correcting for Changes in Crystal Transparency

To achieve the required constant term in the energy resolution (Section 2.7.1) the crystals will be monitored in situ to track and correct for changes in transparency. Calibration coefficients that relate transparency at different times are dependent on the parameter R [41], where;

$$R = \frac{log\,(Fractional\ Change\ in\ Scintillation\ Signal)}{log\,(Fractional\ Change\ in\ Monitoring\ Signal)} \tag{3.5}$$

If R can be calculated with a small enough variation between crystals then it can be considered a universal crystal parameter. It will therefore be possible to calculate a change in the scintillation light, caused by radiation damage and subsequent recovery, from a change in the monitoring signal for all crystals in CMS assuming a single value of R for all crystals. The parameter R was measured for each crystal in a sample of SIC preproduction crystals and the results are detailed in this chapter.

3.1.4 Longitudinal Non-uniformity of Light Yield

Despite efforts of the crystal grower to produce uniform crystals, many exhibit a non-uniformity of light yield along their length. Electromagnetic showers in the CMS ECAL will reach a maximum at about eight radiation lengths from the front face of the crystal on average. If the light collected varies as a function of depth in the region where most energy is deposited, known as the shower maximum, then the light collected from a shower will depend on depth. Shower to shower variation of this depth will induce a variation in the reconstructed energy inducing a constant term in the energy resolution [42]. If the degree of non-uniformity is large then this will seriously degrade the resolution.

There are two competing factors that contribute to uniformity: focusing and absorption. The taper of the crystals combined with the high refractive index of lead

tungstate focuses scintillation light so showers that develop earlier give a larger response. Absorption has the opposite affect; a short light attenuation length leads to a decrease in light yield for earlier developing showers.

Crystals produced by SIC tend to have long attenuation lengths so focusing is the dominant factor and crystals suffer from non-uniformity in the shower maximum region. To avoid this seriously degrading the energy resolution the collaboration imposes a limit on the absolute value of the parameter known as the front non-uniformity (FNUF) with units of $\%/X_0$. Radiation damage in a crystal can lead to a change in FNUF because the attenuation length changes. FNUF was measured for a small sample of crystals both before and after irradiation, the results of which are detailed in this chapter.

The taper of barrel crystals is more pronounced than endcap crystals and therefore they suffer large non-uniformity. For this reason the barrel crystals had one face depolished to reduce focussing and achieve the required light collection uniformity. The resulting loss of light is partly compensated for by surrounding the crystals with a reflective aluminium coating applied to the inside of the alveolar support structure. Deopolishing of the endcap crystals was not considered necessary due to the smaller taper.

3.2 Procedure for Testing Endcap Crystals from SIC

The Shanghai Institute of Ceramics produced preproduction endcap crystals for CMS during 2004/2005 (Table 3.1). Forty five of these from various batches were tested at Imperial College during 2005. One crystal from the Bogoroditsk Techno-Chemical Plant has also been tested for comparison. Radiation hardness and the ratio R (Eqn. 3.5) were calculated for all these crystals. Ten crystals were measured both at Imperial College and at ENEA, a laboratory near Rome, in the interest of providing a calibration between the two institutes. Of these ten, five had pre and post irradiation FNUF measurements taken at Imperial College to investigate

how non-uniformity is affected by irradiation. Details concerning batch numbers and dates measured are given in Table 2 and Table 3 in Appendix B. Details of the apparatus used to perform these measurements are provided in this section.

3.2.1 Measuring SIC Crystals at Imperial College

Crystals are annealed before any measurements are made in order to remove any colour centres in the lattice. This involves heating gradually to a temperature of $200°C$ in an oven, maintaining this temperature for 24 hours and then bringing it back down to $18°C$. Measurements of light yield and transmission are made after annealing and then the crystals are irradiated. After irradiation, measurements are taken every day for the next ten to twenty days in order to map the recovery.

Irradiation Facility at Brunel University

Brunel University has two radiation cells. One of these houses a ^{60}Co source with an activity of $0.93TBq$. Crystals are irradiated for 24 hrs at a rate of approximately 7Gy/hr, which is the rate expected in the CMS ECAL endcaps at a pseudorapidity of 2.7 [35]. The dose rate in the endcaps ranges from $0.29Gy/hr$ at the point where it meets the barrel to $15.0Gy/hr$ at maximum pseudorapidity (Table 1 in Appendix A). The other cell contains a ^{60}Co source that is capable of irradiating the crystals at approximately $16.5Gy/hr$. Both cells are kept at a temperature of about $20°C$.

Light Yield Measurement

The apparatus used to measure the light yield, in photoelectrons per MeV, of crystals at Imperial College is shown in Figure 3.4. It is kept at $18.0°C \pm 0.1$ because this is the operating temperature of the ECAL. The crystal is wrapped in Tyvek which is a highly reflective, in order to increase the number of photons reaching the detector. Two gammas with energies of 1.173 and $1.32MeV$ are emitted in coincidence from a $20kBq$ ^{60}Co source and produce scintillation in the crystal and the response is measured by a hybrid photomultiplier tube (HPMT). This is used instead of a

photomultiplier tube because the gain is essentially noise free and therefore the required photoelectron resolution can be achieved [43].

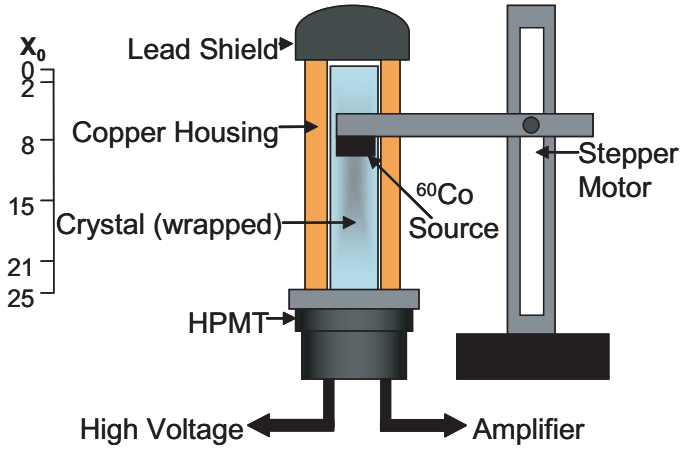

Figure 3.4: Apparatus for measurement of crystal light yield.

Two background scans are taken with the cobalt source raised above the level of the lead shielding and these are subtracted from the light yield scans. For all measurements other than FNUF the light yield in the shower maximum region, which is taken to be 8 X_0 from the crystal front face, is always quoted.

Front Non-Uniformity Measurement

The apparatus in Figure 3.4 is used to measure front non-uniformity (FNUF) defined as the gradient of the light yield with respect to the crystal length calculated between 3.5 and 11.5cm from the crystal front face and has units of $\%/X_0$. To measure this parameter accurately, light yield scans are taken at intervals of 0.89cm (equivalent to one radiation length) from 1.5 to 11.5 radiation lengths from the front face of the crystal. The gradient is found by performing a linear fit to the light yield measurements.

Transmission Measurement at Imperial College

The apparatus shown in Figure 3.5 is used to measure transmission. Light from the LED is channelled along an optical fibre and incident on the rear face of the crystal.

Figure 3.6 shows the spectrum of the LED which is similar to the scintillation spectrum of lead tungstate (Fig. 3.2). The light travels through the crystal and is reflected at the front face, then travels back to the rear face where it is read out by a photodiode in the centre of the rear face of the crystal. The apparatus is set up in this way to emulate the endcap monitoring configuration in CMS. Signal and reference readings are then taken. Reference measurements are used to correct for variations in signal due to changes in LED output. The equation for transmission (T) is:

$$T = \frac{Signal}{Reference} \tag{3.6}$$

The signal is read out by the rear photodiode and the reference is simply the output of the LED measured by another photodiode used to correct for fluctuations in the LED light.

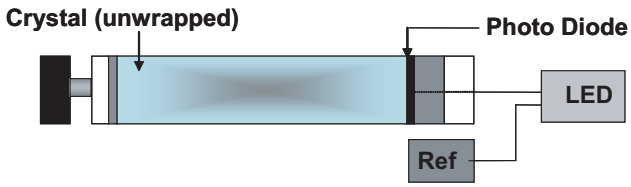

Figure 3.5: Apparatus for measurement of transmission.

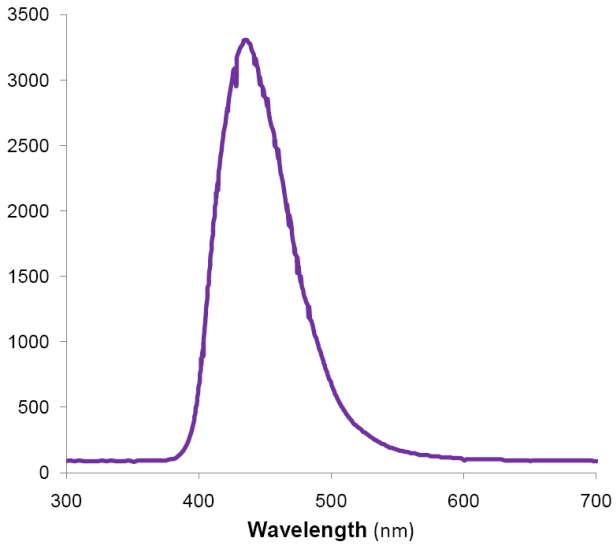

Figure 3.6: LED spectrum.

Induced Absorption Coefficient Calculation

The induced absorption coefficient (μ) is a quantity that reflects how much light a crystal absorbs per metre as a result of radiation damage and subsequent recovery [39]. Transmission measurements made using the apparatus in Figure 3.5 are used to calculate μ using the following formula:

$$\mu(t) = \frac{1}{l} ln \left[\frac{T_{init}}{T_{post-irrad}(t)} \right] \tag{3.7}$$

where T_{init} is the optical transmission before irradiation, $T_{post-irrad}$ is the optical transmission as a function of recovery time t and l is the length of crystal through which the light travels. The maximum induced absorption coefficient occurs immediately after irradiation and quantifies radiation hardness. For a crystal to be considered suitable for use in CMS the μ must be less than $1.5m^{-1}$. Measurement of μ also allows a comparison between experimental data and damage kinetics theory.

Ratio of Change in Scintillation Light to Change in Monitoring Signal Measurement

Pre and post irradiation measurements of light yield and transmission are made using the apparatus in Figures 3.4 and 3.5 and results are used to compute the ratio of change in scintillation light to change in monitoring signal (R). To calculate R the log of the ratio of light yield pre and post irradiation is plotted vs the log of the ratio of transmission pre and post irradiation. R is defined as the gradient of a linear fit to the data points.

3.2.2 Calibration Measurements at ENEA

In order to compare the induced absorption coefficient calculated at two crystal laboratories, calibration measurements were taken at the research centre ENEA and subsequently at Imperial College. Crystals produced at SIC from various batches were annealed, irradiated and transmission measurements subsequently taken. The apparatus used at ENEA is described in the following two sections.

Irradiation Facility

The irradiation plant, namely Calliope, is located in the Research Centre ENEA near Rome [44]. The irradiation cell houses a ^{60}Co source with an activity of $672 \times TBq$ which is immersed in water when the plant is not active. It is possible to obtain a wide range of dose rates due to the geometry of the cell. The crystals were irradiated at approximately $16.5 Gy/hr$ which is a little larger than the maximum expected dose rate in the ECAL endcaps at maximum pseudorapidity. The period of irradiation was 24 hours.

Transmission Measurement

Transmission measurements were made by the dedicated spectrophotometer called Lumen illustrated in Figure 3.7 [45]. The light for both paths comes from the same lamp via an arrangement of mirrors. The instrument is equipped with two different lamps so measurements can be taken over a large wavelength range[‡]. Reference readings are taken in conjunction with the crystal in order to correct for changes in light intensity. A baseline scan is also taken prior to measurements and dedicated software is used to correct the results accordingly.

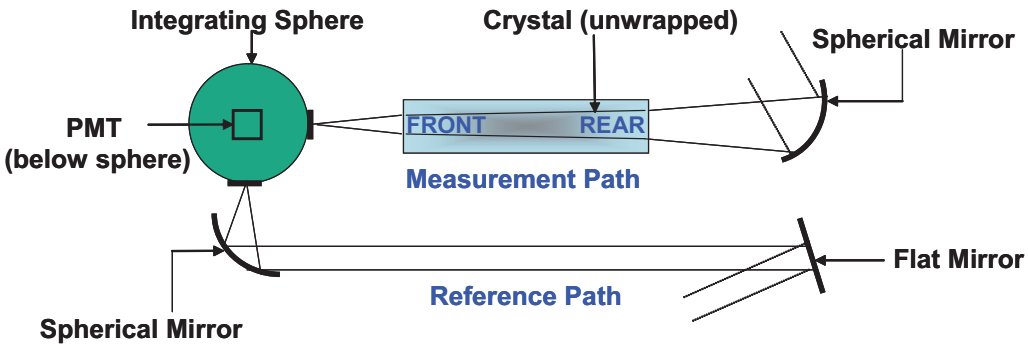

Figure 3.7: Apparatus used to measure transmission at ENEA.

Measurements are performed in a temperature controlled dark room a few metres away from Calliope so transmission can be measured very quickly after a sufficiently

[‡]A deuterium lamp is used for wavelengths shorter than 365nm. For wavelengths above this a quartz tungsten halogen lamp is used.

long and intense irradiation. Measurements are made before irradiation, after annealing, and for approximately ten days after the end of the irradiation period in order to map recovery. The crystals are kept in the dark at all times and at a temperature of $18°C$.

The main features of the apparatus for measurement of transmission at Imperial College and ENEA are given in Table 3.2.

	Imperial College	**ENEA**
Light Injection Point	Rear of crystal	Rear of crystal
Readout Point	Rear of crystal	Front of crystal
Light Source	Diffuse Light Source	Collimated Light Source
Wavelength Range(nm)	400 - 550 (range of LED spectrum)	320 - 700 (measurements at 3nm steps)

Table 3.2: Main features of transmission measurement apparatus.

3.3 Results of Crystal Measurements

Forty five SIC crystals have been tested during 2005 from batches $1-6$, along with one from BTCP for comparison (Table 2 and 3 in Appendix B). Measurements showing how light yield changes with time due to irradiation and subsequent recovery are displayed in this section for a group of four SIC crystals from batch 1 and five from batch 5. Plots displaying R and μ are included for one SIC crystal from each group and the BTCP crystal. A summary of the results for these crystals is also included, followed by results of calibration measurements with ENEA and front non-uniformity measurements (Sections 3.3.4, 3.3.5 and 3.3.6 respectively).

3.3.1 Light Yield

Goals of Measurements

The goal of the light yield measurements is to check that crystals are radiation hard enough for use in CMS by measuring the percentage light yield decrease between

pre and post irradiation. This value must be below 45% for crystals to be considered suitable. Investigation into the how light yield changes as crystals recover is important to show how crystal response is expected to vary in CMS.

Results

Figure 3.8 shows pre and post irradiation light yields vs. time for four SIC crystals from batch 1. The first point is a pre irradiation average calculated for each crystal. The shaded region corresponds to the irradiation period. The graph shows how the light yield changes as a result of irradiation and how the crystals recover. The light yield plateaus after about 2 weeks' recovery with a lower value than the pre irradiation average.

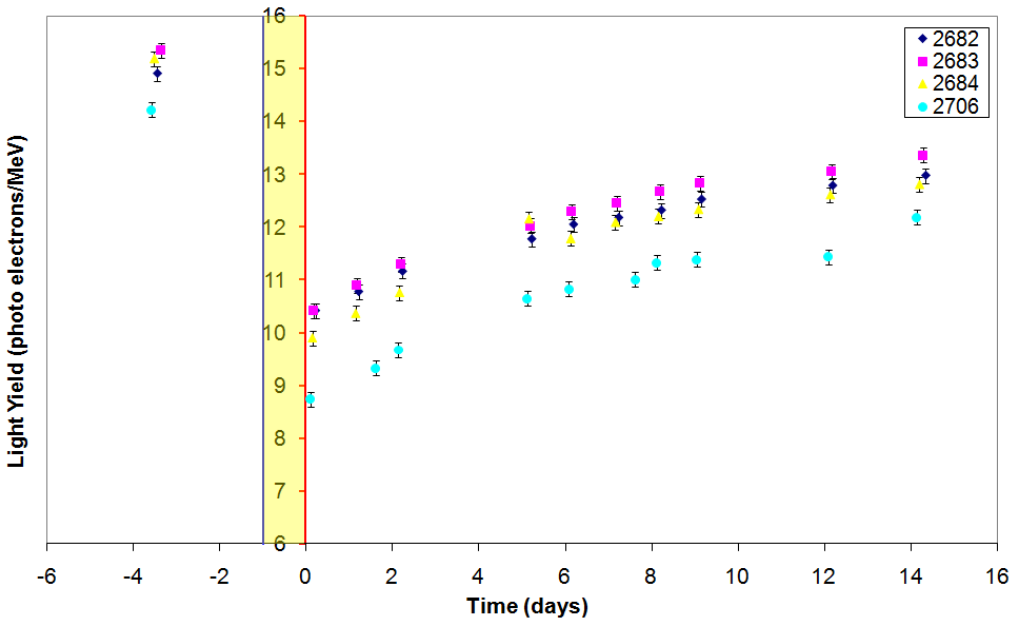

Figure 3.8: Pre and post irradiation light yields at $8X_0$ for four SIC crystals from batch 1. The shaded region indicates the irradiation period.

Comparison of a crystal's properties after annealing with properties after irradiation gives a good idea of how radiation hard the crystal is. However, in CMS the crystals will receive dose after dose of irradiation without annealing completely so it is important to see how crystals behave after repeated irradiations. In order to investigate this behaviour five crystals from batch 5 have been annealed once and

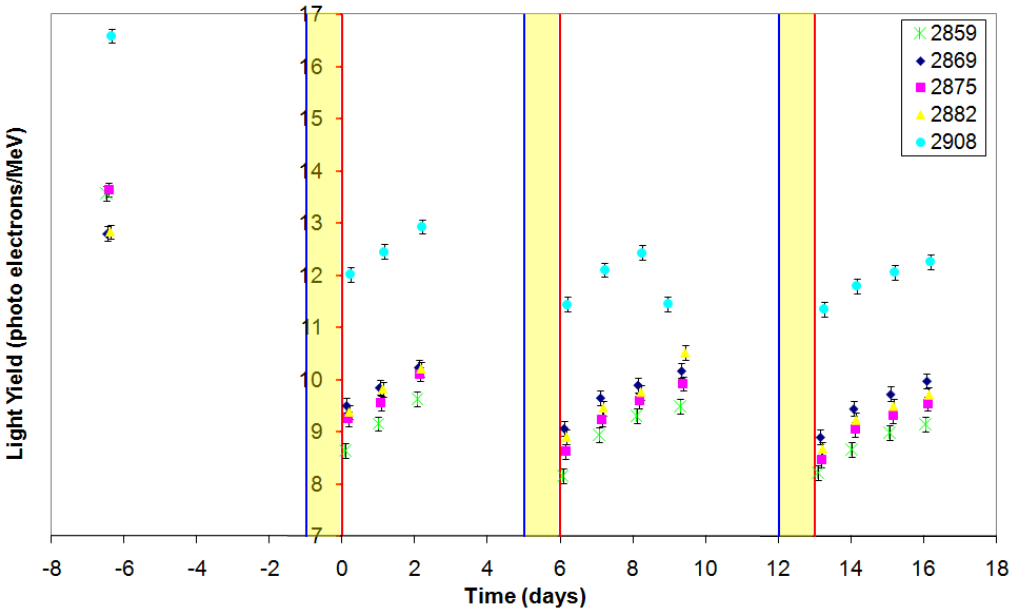

Figure 3.9: Pre and post irradiation light yields at $8X_0$ for five crystals from batch 5. The shaded region indicates the irradiation period. No annealing before second and third irradiations.

irradiated as usual, followed by two further irradiations without annealing. Figure 3.9 shows how the light yield changes with time for these crystals where the shaded areas represent irradiation periods. The measurement of crystal 2908 taken on the ninth day after irradiation is anomalous the reason for which is unclear.

Interpretation of Results

Irradiation causes a drop in the light yield of crystals (Fig. 3.8) as it induces a change in charge state of pre-existing defects in the crystal lattice leading to the formation of colour centres. These centres absorb scintillation light. It is this effect that is responsible for the observed loss in light yield, as the scintillation mechanism is not affected by radiation.

Subsequent to the initial drop in response, the light yield increases with recovery time (Fig. 3.8). Section 3.1.2 describes how colour centres can be created and annihilated during irradiation, dependent on the dose rate. Radiation induces the creation of these centres and post irradiation colour centres annihilate. As this occurs the crystal absorbs less scintillation light leading to an increase in light yield.

However, for the crystals shown the light yield does not reach the pre irradiation value over the timescale of the tests (about 2 weeks). This leads to the assumption that some colour centres have large recovery time constants and therefore cause semi-permanent damage in the crystal.

Figure 3.9 shows how the light yield of crystals is affected by repeated periods of irradiation and recovery. It can be seen that irradiation always causes a drop in light yield due to formation of colour centres, followed by recovery due to their annihilation. After the initial irradiation and recovery the amount of semi-permanent damage does not increase significantly. From this study and the results given in [46] it is expected that after the first couple of irradiations the pattern will repeat. The damage kinetics of colour centres can be used to explain this behaviour. The model describes how colour centres form at a finite number of pre-existing defects in the crystal lattice. It is expected that after the irradiation period the damage will be saturated, hence all the pre-existing defects will have formed colour centres. Those with long decay times will be formed during the first irradiation and cause semi-permanent damage. Such colour centres will not noticeably recover during the time span of the measurements. Annihilation of colour centres with shorter recovery time constants, of the order of a few days, are responsible for the changes in light yield observed during the second and third recovery periods.

3.3.2 Induced Absorption Coefficient

Goals of Measurements

The goals of the measurement of induced absorption coefficient (μ) are the same as those for light yield. However, light yield is measured by inducing scintillation whereas μ is calculated from transmission measurements. It is therefore a good test of the apparatus that the values show consistency. The maximum induced absorption coefficient measured at 420nm in CMS like radiation conditions must be below $1.5m^{-1}$ [§] for crystals to be considered suitable for use in CMS.

[§]More recently this constraint was raised to $1.6m^{-1}$ for SIC crystals to increase the yield.

Results

Equation 3.7 shows how the induced absorption coefficient can be calculated from pre and post irradiation transmission measurements. Pre irradiation μ is defined to be zero and is a maximum immediately after irradiation. The recovery can be described by a first order exponential plus a constant term with parameters given in Table 3.3. Figure 3.10 shows how μ changes with time after irradiation for crystal number 2706 from batch 1. Figure 3.11 shows how the induced absorption coefficient changes with time for batch 5 crystal 2859 that underwent three irradiations.

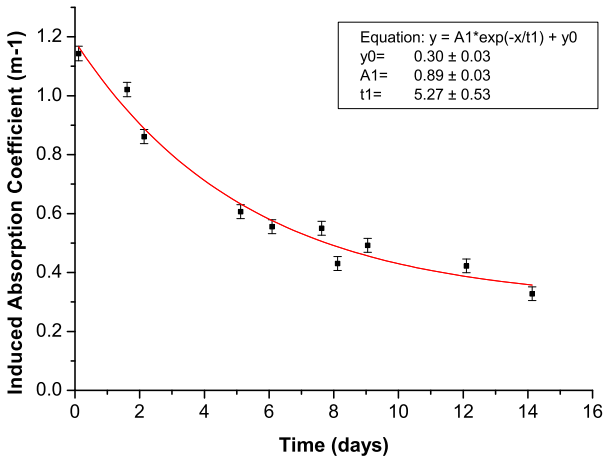

Figure 3.10: Induced absorption coefficient measurement for SIC crystal 2706.

The graphs show that μ has increased from 0 during irradiation followed by a decrease as the crystal recovers. The induced absorption coefficient does not return to zero again on a short timescale. Values of μ immediately after irradiation are given in Table 4 and 5 in Appendix C for all crystals tested.

Recovery Time Constants

The recovery time constants are found by fitting the data of μ vs. recovery time and have been calculated for the four batch 1 SIC crystals along with BTCP 2552 (Table 3.3). The mean recovery time for the SIC crystals is 4.30 days with a standard

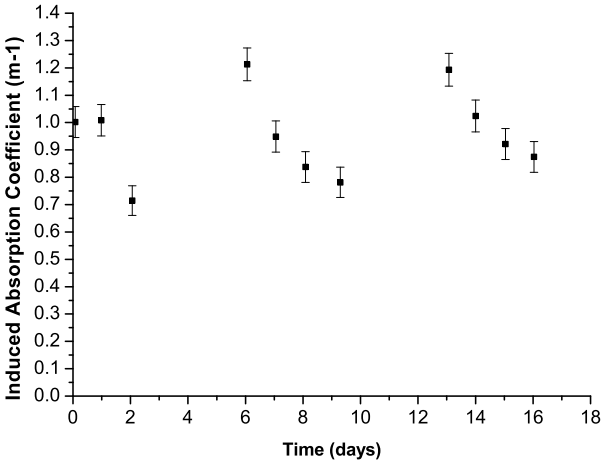

Figure 3.11: Induced absorption coefficient measurement for SIC crystal 2859.

deviation of 0.72. It can be seen that the BTCP crystal recovers about twice as quickly as the SIC crystals.

Crystal No	Recovery Time Const.(days)
2552	2.16 ± 0.54
2682	4.01 ± 0.99
2683	3.59 ± 0.96
2684	4.34 ± 1.07
2706	5.27 ± 0.53

Table 3.3: Time recovery constants for four batch 1 SIC crystals and BTCP 2552.

Interpretation of Results

The induced absorption coefficient is similar to light yield in that it is also a measure of how much scintillation light a crystal will absorb. In Figure 3.10 it can be seen that μ induced is about $1.2m^{-1}$ immediately post irradiation and subsequently decreases exponentially toward a value of $0.30 \pm 0.03\ m^{-1}$ with a time constant of 5.27 ± 0.53 days. Figure 3.3 shows that colour centres with large recovery time constants are responsible for μ not returning to zero in the timescale of the experiment. It can be concluded that about a quarter of the damage induced by the radiation rate of approximately $7Gy/hr$ for 24 hours is semi-permanent. Very fast recovering centres

(less than a minute) could also have been formed in the crystal during irradiation but these contribute negligibly to μ (Figure 3.3). The observed change in μ from $1.2m^{-1}$ post irradiation to $0.30m^{-1}$ post-recovery is caused by colour centres with recovery time constants of just less than a week. The radiation damage caused by this type of centre recovers almost completely within 2 weeks.

The BTCP crystal recovered about twice as quickly as the SIC crystals measured. This is owing to the fact that differences in raw material composition and growth mechanisms[¶] lead to the creation of different lattice defects which form different types of colour centre with distinct time recovery constants.

3.3.3 Ratio of Change in Scintillation Light to Change in Monitoring Signal (R)

Goals of Measurements

The goals of the measurements of R are to compare SIC and BTCP crystals and to measure the spread in values for SIC crystals to see if R can be considered a universal crystal parameter. To ensure that the error introduced by correcting for changes in transparency is tolerable the rms variation in R must be less than 0.05 [41]. The mean value of R for SIC crystals must also be calculated and is expected to be close to unity.

Results

Figure 3.12 shows a plot of scintillation signal vs. monitoring signal for a batch 1 crystal. The value of R for this crystal is calculated as 0.92 ± 0.03. All points along the line are normalised to the pre irradiation average which lies at (0,0) but the linear fit is not forced to go through the origin. The further a data point is away from the origin, the more damaged the crystal is; hence, as the crystal recovers the points move along the line toward (0,0).

[¶]BTCP crystals were grown using the Czolchralski method [47] while SIC used the modified Bridgeman technique.

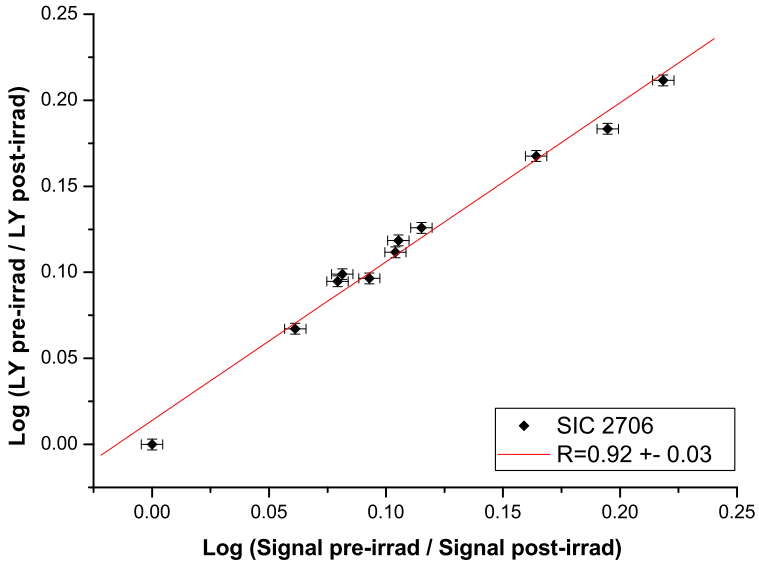

Figure 3.12: R measurement for SIC crystal 2706.

In order to compare the R values between Chinese and Russian crystals, BTCP crystal 2552 was also measured. The R value for this crystal is 1.31 ±0.08 (Fig. 3.13), which is significantly higher than the SIC crystals. Values of R for all SIC crystals tested are given in Table 4 and 5 in Appendix C.

Interpretation of Results

Figures 3.13 and 3.12 show that R for the Russian crystal is significantly larger than the Chinese. This effect that has been seen in 2004 test beam results [48] and previous studies at Imperial College [49]. However, as long as the variation in R for crystals produced by the same supplier is small then it is acceptable not to know R for each individual crystal.

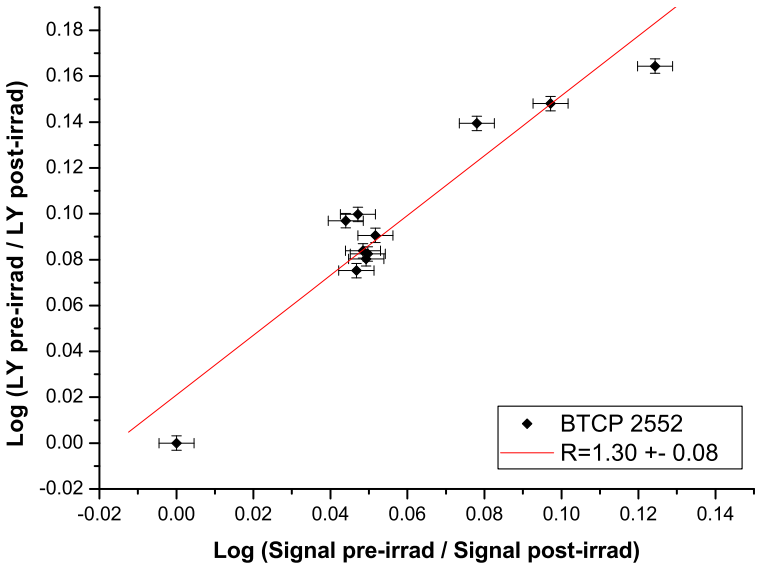

Figure 3.13: R measurement for BTCP crystal 2552.

3.3.4 Summary of Results for SIC Crystals Irradiated at approximately 7Gy/hr for 24 Hours

Goals of Measurements

The goal is to investigate how damaged crystals become when exposed to a radiation dose typical of what they will receive in CMS ECAL at pseudorapidity of 2.7.

Results

Thirty five SIC crystals were irradiated at a dose rate of approximately $7Gy/hr$ for 24 hours and the results are given in Table 4 in Appendix C. The mean light yield decrease, maximum μ and R are 27%, $0.74m^{-1}$ and 0.98 with an average error on each measurement of 1%, $0.05m^{-1}$ and 0.06 respectively.

Figure 3.14 shows the maximum percentage decrease in light yield for these SIC crystals. For a crystal to be suitable for use in CMS the decrease in light yield measured at Imperial College should be less than about 45% and all crystals tested fulfilled this criterion.

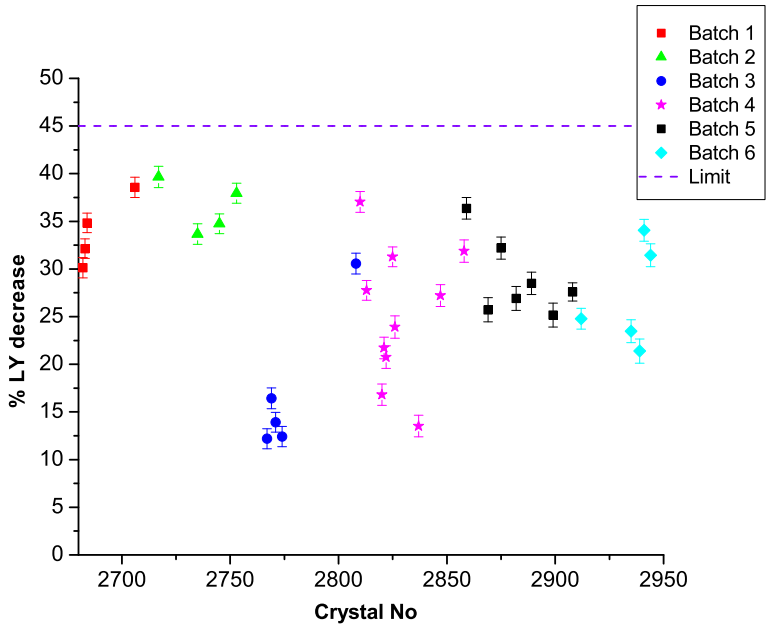

Figure 3.14: Percentage light yield decrease for SIC crystals irradiated at approximately $7Gy/hr$ for 24 hours.

Figure 3.15 shows induced absorption coefficients for these SIC crystals. The maximum μ must be below $1.5m^{-1}$ to be considered acceptable for use in CMS. All crystals tested met this criterion.

Figure 3.16 shows induced absorption coefficients versus light yield decrease for these SIC crystals. The correlation between the variables is strong and positive which is essential for the success of the laser light monitoring system in the CMS ECAL.

Figure 3.17 shows the measurement of R along with experiemental errors for all 35 crystals. Figure 3.18 shows the spread in R for these SIC crystals. The mean of this data is 0.97 with standard deviation of 0.06.

Interpretation of Results

All SIC crystals irradiated at a dose rate of approximately $7Gy/hr$ for 24 hours fall within the limits deemed to be acceptable for light yield and μ (Figs. 3.14 and 3.15). Figure 3.16 shows that induced absorption coefficient and light yield decrease are

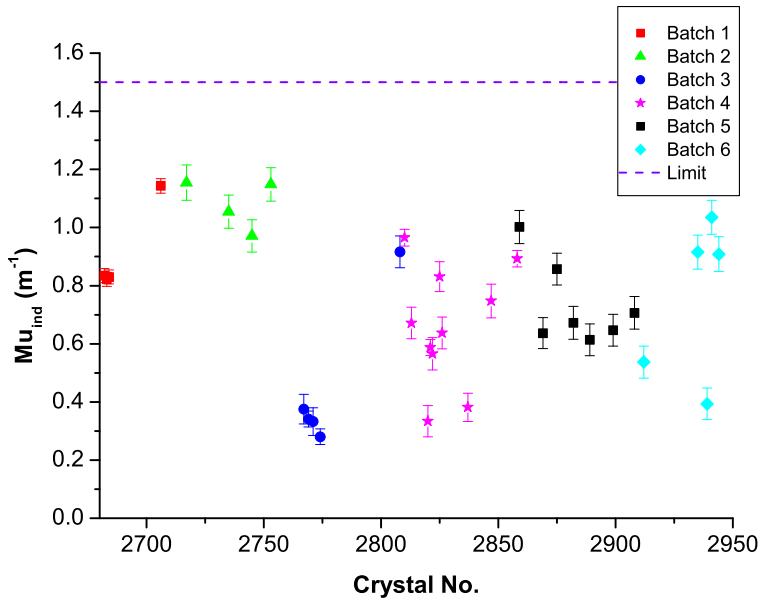

Figure 3.15: Induced absorption coefficient for SIC crystals irradiated at approximately $7Gy/hr$ for 24 hours.

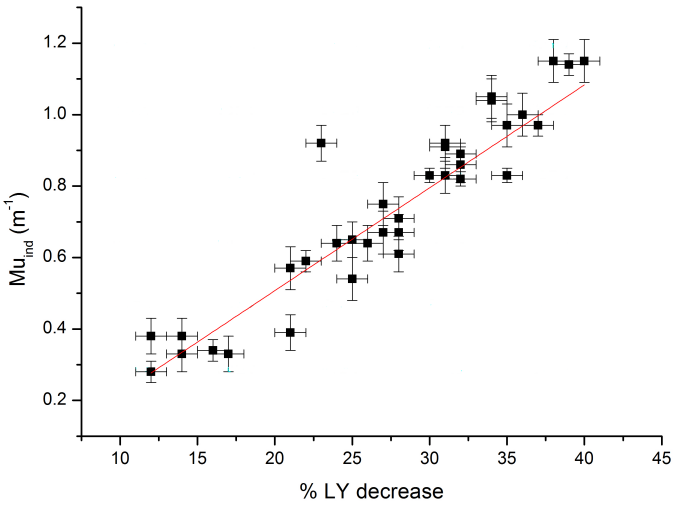

Figure 3.16: Induced absorption coefficient versus light yield decrease for SIC crystals irradiated at approximately $7Gy/hr$ for 24 hours. The intercept of the linear fit is -0.069 ± 0.05 and the slope is 0.029 ± 0.002.

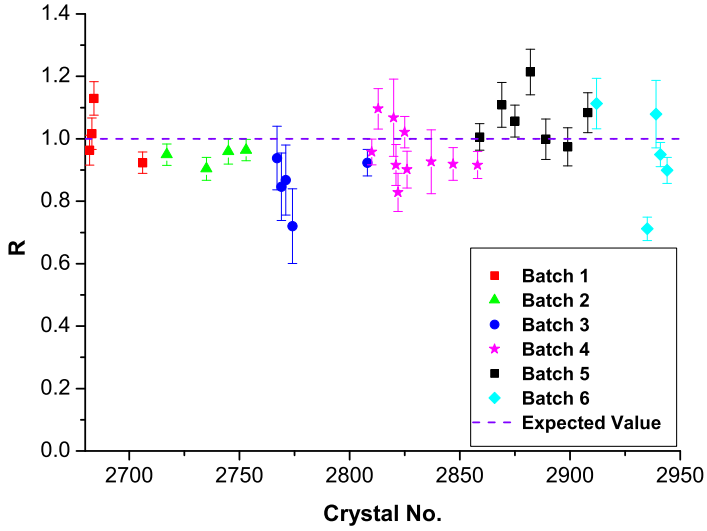

Figure 3.17: R measurements for SIC crystals irradiated at approximately $7Gy/hr$ for 24 hours.

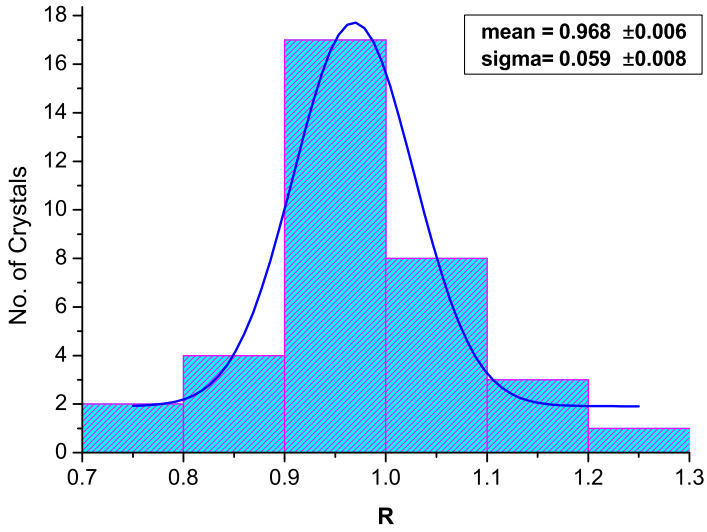

Figure 3.18: Histogram of R measurements for SIC crystals irradiated at approximately $7Gy/hr$ for 24 hours.

strongly correlated therefore a change in scintillation light is correlated to a change in transparency. This is essential for the operation of the laser monitoring signal in CMS. Figure 3.18 shows that the spread in R is 0.06 with a mean of 0.97. In order for R to be considered a universal parameter, production standard SIC crystals are required to have an rms spread in R less than 0.05 [41]. The results suggest that the current spread in R is larger than this but considering that production crystals should be more consistent than preproduction crystals the constraints are feasible.

3.3.5 Results of Calibration with ENEA

Goals of Measurements

The goal of the measurements conducted at ENEA is to provide a calibration with Imperial College. Such measurements were needed to increase the collaboration's confidence in the consistency of measurements conducted at different institutes.

Results

Ten SIC crystals were measured at ENEA and Imperial College. They were irradiated at a dose rate of approximately $16.5 Gy/hr$ for 24 hours. Figure 3.19 shows the results of transmission scans taken at ENEA for SIC crystal 2920. It can be seen that the amount of damage induced by irradiation is dependent on wavelength. Induced absorption coefficients measured at ENEA are quoted at 420nm as this is near the peak of the scintillation spectrum for lead tungstate and Figure 3.20 shows μ as a function of time.

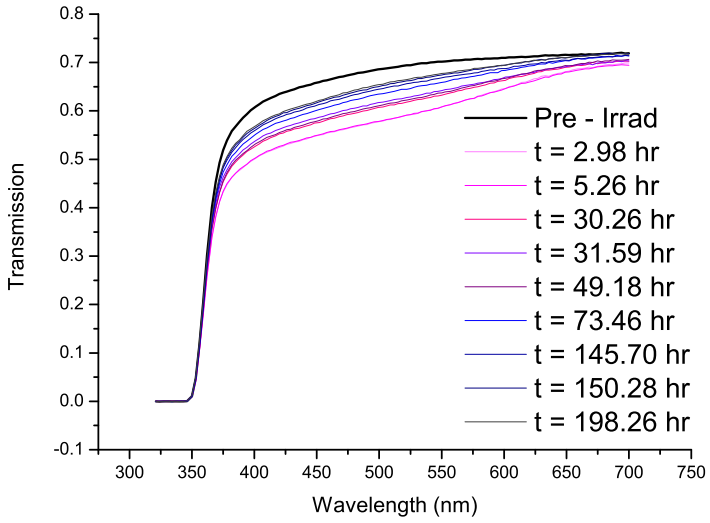

Figure 3.19: Transmission as a function of wavelength measured using Lumen. The black line shows the undamaged transmission curve and the lowest transmission occurs immediately post irradiation. Transmission increases with recovery time and the curves are time ordered.

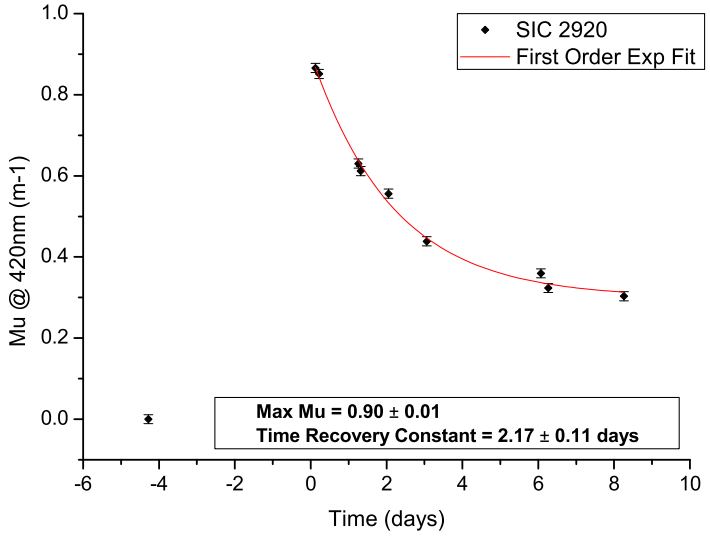

Figure 3.20: Induced absorption coefficient at 420nm as a function of time.

The maximum values of μ at 420nm for all ten crystals are compared to the maximum μ measured at IC using the LED (Fig. 3.21). The fit is fixed to go through the origin. It can be seen from the plot that the crystal with the smallest μ_{ind} according to both Imperial College and ENEA measurements lies many sigma off the line. This data point is thought to be anomalous as it behaves differently from the rest of the crystals tested. For this reason it will not be taken into account in the interpretation of the results from this section.

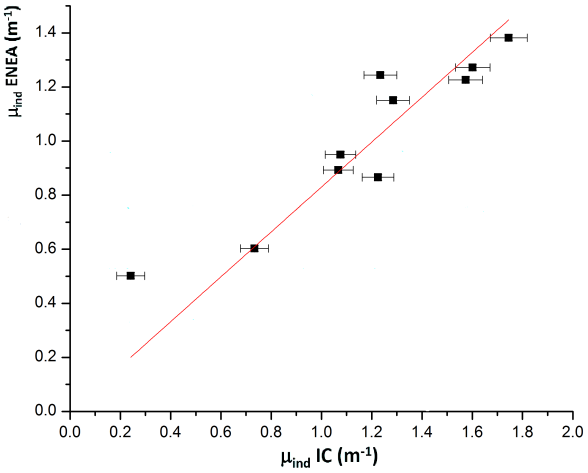

Figure 3.21: Correlation of maximum induced absorption coefficients measured at Imperial College and ENEA. The fit is fixed to go through the origin. The y error bars on the plot are small and therefore difficult to resolve.

Figure 3.22 shows the relationship between the maximum values of μ at 420nm measured at ENEA and the maximum μ measured at Imperial College without the anomalous data point. The plot shows a strong positive correlation for the nine crystals tested. The linear fit is fixed to go though the origin and the slope is given in Equation 3.8:

$$\mu_{ind}^{enea} = (0.83 \pm 0.03)\mu_{ind}^{IC} \tag{3.8}$$

where $\mu_{ind}^{enea/IC}$ is the induced absorption coefficient measured at ENEA / Imperial College.

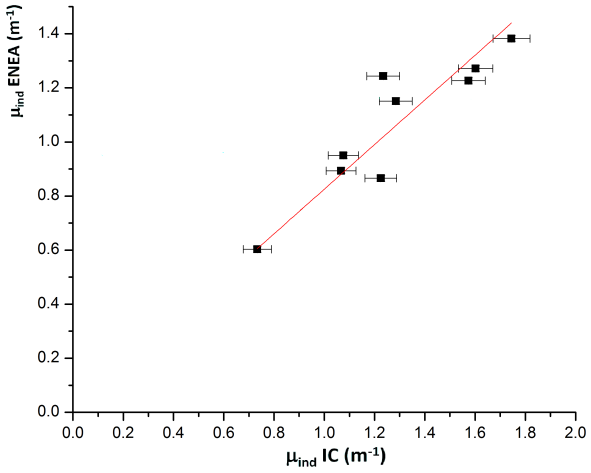

Figure 3.22: Correlation of maximum induced absorption coefficients measured at Imperial College and ENEA for nine crystals (anomalous data point not included). The fit is fixed to go through the origin. The y error bars on the plot are small and therefore difficult to resolve.

Interpretation of Results

The maximum values of μ measured at ENEA and at Imperial College are well correlated (Fig. 3.22). Therefore, it is possible to calculate one from the other (assuming the same irradiation dose rates, dose and measurement conditions). The uncertainty introduced by the linear fit combined with the systematic error on the measurement of maximum μ at IC introduces an uncertainty in the calculated value of maximum μ at ENEA. This was calculated to be approximately a percent higher than the uncertainty on the Imperial College measurement.

The relationship between the μ values is $\mu_{ind}^{enea} = 0.83\mu_{ind}^{imp}$ so maximum induced absorption coefficients measured at ENEA are lower than those measured at IC. Possible causes of the slope of the fit not being unity could be differences in the radiation conditions, for example the dose profile along the crystal, and/or differences in measurement conditions but the true reason is unknown.

In summary the results from each laboratory can be compared using Equation 3.8 and the form of the equation is understood and is due to differences in the experimental methods.

3.3.6 Front Non-Uniformity Results for SIC Crystals Irradiated at approximately 16.5Gy/hr for 24 hours.

Goals of Measurements

The goal of the uniformity measurements is to investigate the effect that radiation has on FNUF.

Results

FNUF measurements were taken for five SIC crystals irradiated at approximately $16.5 Gy/hr$ for 24 hours. All crystals tested exhibited the highest light yields at the measurement point closest to the front face of the crystal. Light yields then decrease linearly toward the centre of the crystal (Fig. 3.23).

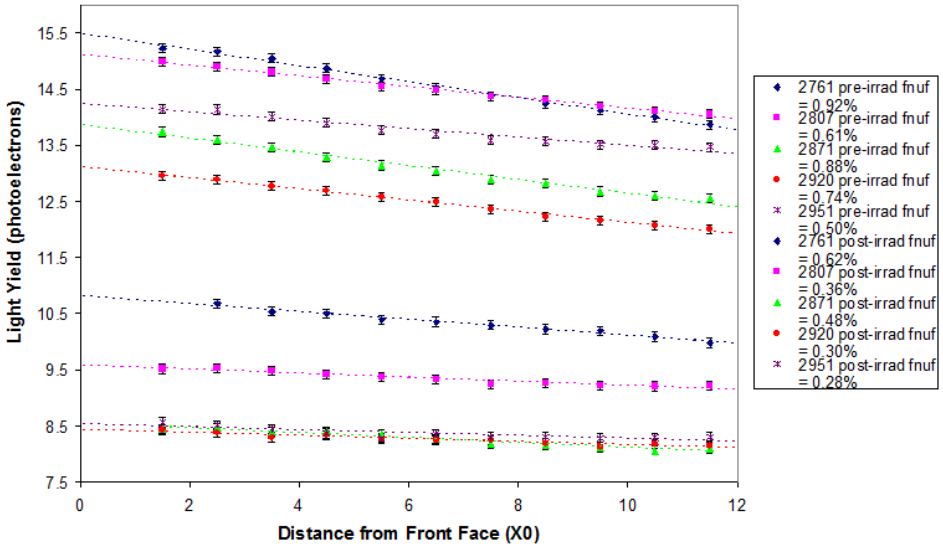

Figure 3.23: Pre and post irradiation light yield vs. distance from crystal front face for five SIC crystals. FNUF values ($\%/X_0$) are given in the legend where the group with light yields ranging from 12 to 15.5 (8 to 11) correspond to pre (post) irradiation measurments.

Table 3.4 shows the correlation between the value of FNUF and μ for individual crystals.

Crystal No.	Correlation
2761	-0.96
2807	-0.89
2871	-0.95
2920	-0.97
2951	-0.94

Table 3.4: Table to show the correlation between value of FNUF and μ for individual SIC crystals.

The histograms in Figure 3.24 compare front non-uniformity before and immediately after irradiation. The value of FNUF decreases post irradiation for all five crystals tested.

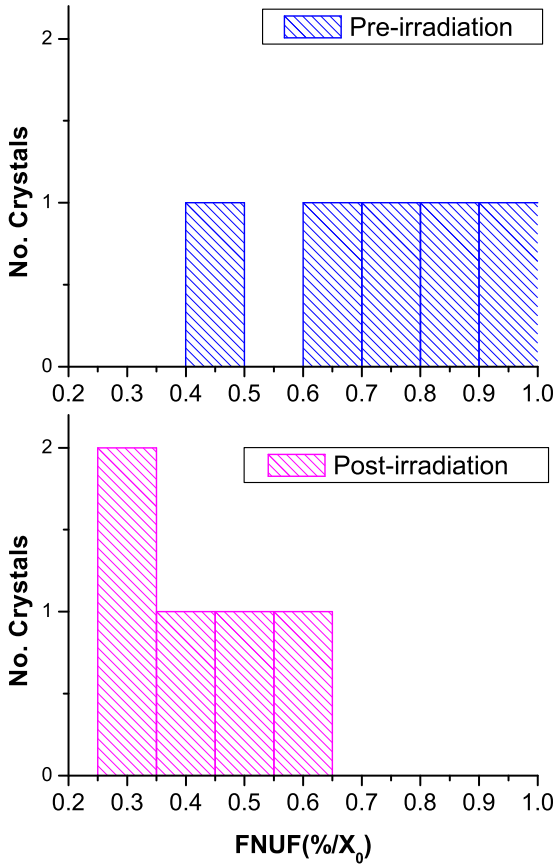

Figure 3.24: Histograms comparing pre and post irradiation FNUF values.

Figure 3.25 shows how the value of FNUF measured immediately after irradiation

is related to the radiation hardness of crystals. The strong negative correlation between the variables implies that radiation hard crystals are less uniform post irradiation than radiation soft crystals. The correlation coefficient is -0.94.

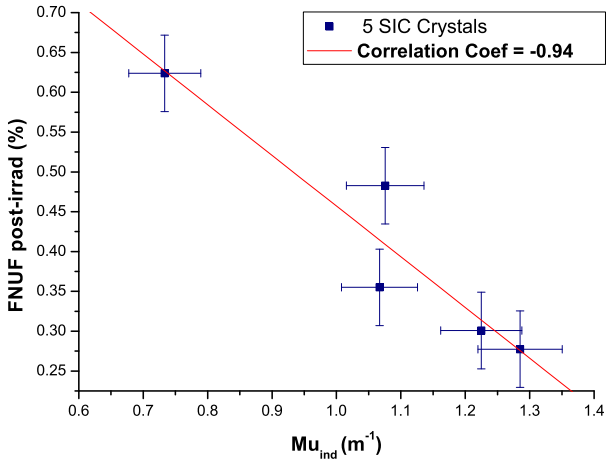

Figure 3.25: Graph showing correlation between FNUF immediately post irradiation and maximum induced absorption coefficient.

Interpretation of Results

The degree of non-uniformity decreases with the amount of radiation damage received (Table. 3.4). This is due to the fact that radiation leads to a decrease in the light attenuation length. As the crystals recover the non-uniformity increases as the colour centres anneal.

Crystals in CMS will always have some degree of radiation damage once data taking begins as it is likely that the crystals will never fully anneal. The effect of radiation on FNUF is advantageous in terms of energy resolution because damage brings the FNUF toward an acceptable value. It must be taken into account that the five SIC crystals measured at IC were wrapped in Tyvek which results in larger values of FNUF than carbon fibre alveolar which surrounds the crystals in CMS [43][‖].

[‖]It should be noted that the gamma rays from the cobalt source used at IC to evoke scintillation in the crystals are not collimated, had it been possible to collimate them it is expected that the absolute values of FNUF measured would be higher.

3.3.7 Summary of Results for SIC Crystals Irradiated at approximately 16.5Gy/hr for 24 Hours

Goals of Measurements

The main goal of the measurements is to investigate the extent of the damage when crystals are exposed to a radiation dose rate marginally higher than in CMS ECAL at maximum pseudorapidity. A possible relationship between μ and R is also considered.

Results

Ten SIC crystals were irradiated at Brunel in the high dose rate cell for 24 hrs at approximately $16.5 Gy/hr$ which is just above the maximum dose rate in the CMS ECAL at high luminosity and high pseudorapidity. From Figure 3.26 it can be seen that seven of the ten crystals tested meet the radiation hardness criterion.

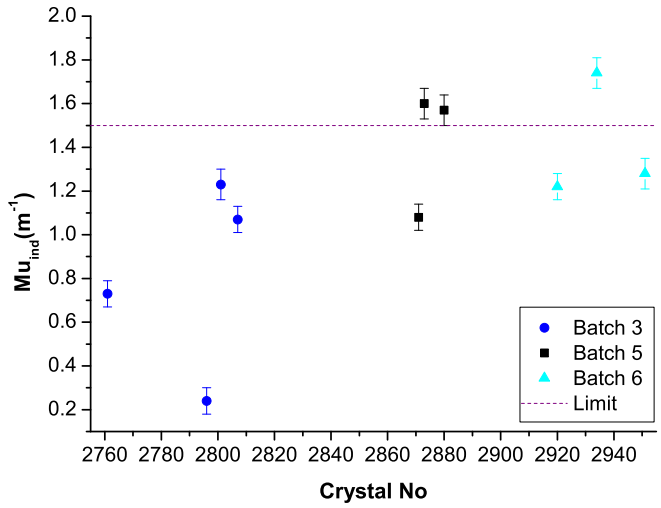

Figure 3.26: Maximum induced absorption coefficient measurements for SIC crystals irradiated at approximately $16.5 Gy/hr$ for 24 hours.

Figure 3.27 shows a strong negative correlation between the parameters R and μ for the ten SIC crystals tested which implies that the more radiation hard a crystal is the higher its R value.

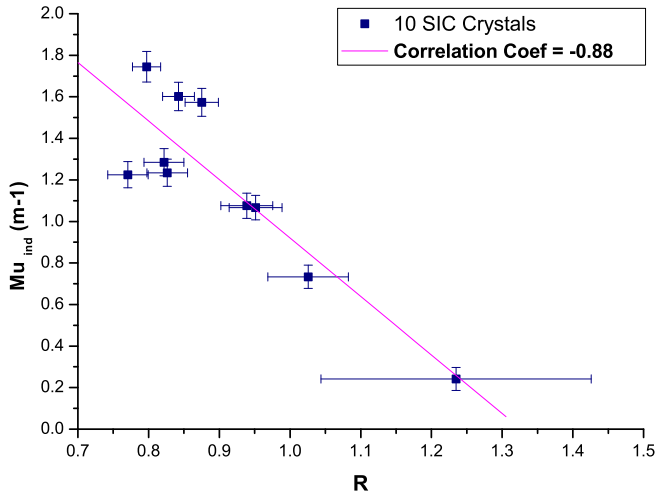

Figure 3.27: Correlation between maximum induced absorption coefficient and R measurements.

Interpretation of Results

The lower the value of a crystal's μ after irradiation, the higher the dose rate it is able to withstand before the energy resolution becomes seriously degraded. The dose rate administered is higher than the dose rate expected at maximum pseudorapidity in the ECAL endcaps at high luminosity. Seven crystals out of ten fall within the limit for μ of 1.5m^{-1} and therefore such crystals are suitable for use anywhere in the endcaps. Crystals like the three that do not fulfill the radiation hardness criteria need to be placed in lower dose rate regions or areas where less precise energy measurement is needed.

The parameter R is time consuming to measure because recovery from irradiation must be mapped for over a week to obtain an accurate value. To measure radiation hardness it is only necessary to measure the crystal twice, before irradiation and as quickly as possible after. If there is a way of estimating R from maximum μ, this would be extremely beneficial. Figure 3.27 shows that for these ten SIC crystals tested at Imperial College there is a strong negative correlation between R and maximum μ. This effect is predicted by Ref. [50]. This implies that the more radiation hard a crystal, the higher its value of R. This effect is due to the fact that

at high values of μ the relationship between light yield and transmission becomes non-linear which manifests itself as a decrease in the value of R.

3.4 Conclusions

All SIC crystals tested at a dose rate of approximately $7Gy/hr$ proved to be sufficiently radiation hard to withstand the harsh CMS endcap ($\eta = 2.7$) environment at high luminosity without unacceptable loss of light yield. Seven of the ten crystals tested at the higher dose rate of approximately $16.5Gy/hr$ had acceptable values of maximum μ. The spread in R values is a little larger than hoped but considered acceptable. At the time of the measurements the information from these studies helped to guide the production of crystals from SIC.

The results of the calibration with ENEA are reliable and values of maximum μ can be compared without unacceptable uncertainties being introduced. The consistency between the measurements increased the confidence that information conveyed to SIC concerning the standard of their crystals was accurate.

Measurements of FNUF have shown that radiation damage has the effect of increasing crystal uniformity which is favourable in terms of decreasing the ECAL energy resolution. It has also been discovered that the more radiation hard a crystal is, the less acceptable the FNUF immediately post irradiation.

Chapter 4

ECAL Reconstruction and Electron Selection in CMS

A major challenge for the hardware and software of any particle detector is the identification of particles with both high purity and efficiency. The analyses detailed in the final two chapters of this thesis involve final state electrons, so this chapter has been devoted to providing a summary of their reconstruction in CMS. The chapter also includes results from test beam analysis and a study carried out by the author to optimise part of the electron reconstruction algorithms.

4.1 Introduction to CMS Software

The CMS software framework (CMSSW) contains a detailed description of the detector [51]. Monte Carlo information is used to simulate LHC data which is then reconstructed using CMSSW. In this way the response of the detector to different particles can be investigated enabling complex reconstruction algorithms to be developed and tested and analyses to be designed before any physics data are available. Not only is CMSSW used for preparing for data taking, it will also provide a user friendly environment to conduct physics analyses when CMS goes online. Much optimisation and validation of the software is ongoing to prepare for LHC startup.

4.2 Reconstruction and Selection of Electrons using CMS Software

A primary electron is composed of a track emanating from the interaction vertex matched with energy deposits in the ECAL. Electron reconstruction is complicated by the presence of tracker material in front of the ECAL which causes many electrons to emit bremsstrahlung in the tracker, making tracks difficult to fit and energy deposits difficult to collect. Dedicated algorithms have been developed to reconstruct electron candidates that deal with such complications [52].

4.2.1 ECAL Clusters and Superclusters

Clusters

The first step in the reconstruction of an electron starts by collecting the energy it deposits in several crystals in the ECAL. The energy from an array of crystals seeded by the crystal with the locally maximum energy deposited is collected into a cluster. Algorithms have been developed that search for energy deposits in crystals surrounding the seed and are optimised to collect a constant fraction of the shower energy without being contaminated with neighbouring particles or noise.

Superclusters

Many electrons emit bremsstrahlung in the tracker. Due to the magnetic field the electrons will bend away from the photons they radiate which results in the production of more than one shower in the ECAL separated in ϕ (Fig. 4.1). As shown in Figure 4.2, clusters along a road in ϕ are sought and collected together to form a supercluster (SC).

Superclustering Algorithms

Two algorithms are being used to reconstruct electron superclusters. The hybrid algorithm is used in the barrel and the island algorithm is implemented in the

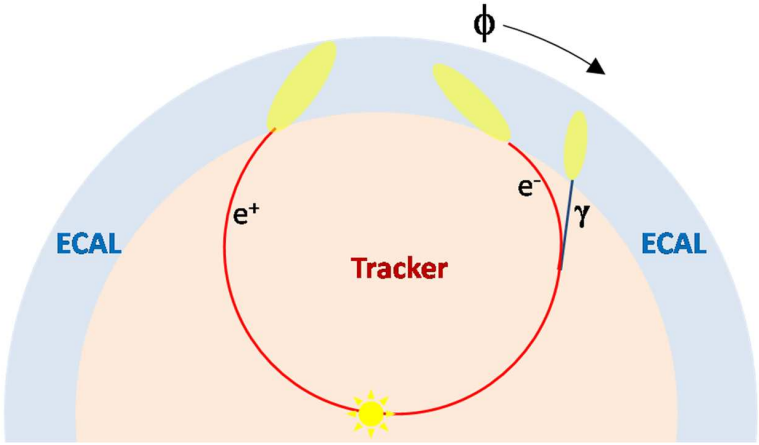

Figure 4.1: Representation of two electrons in CMS tracker and ECAL where one electron emits bremsstrahlung.

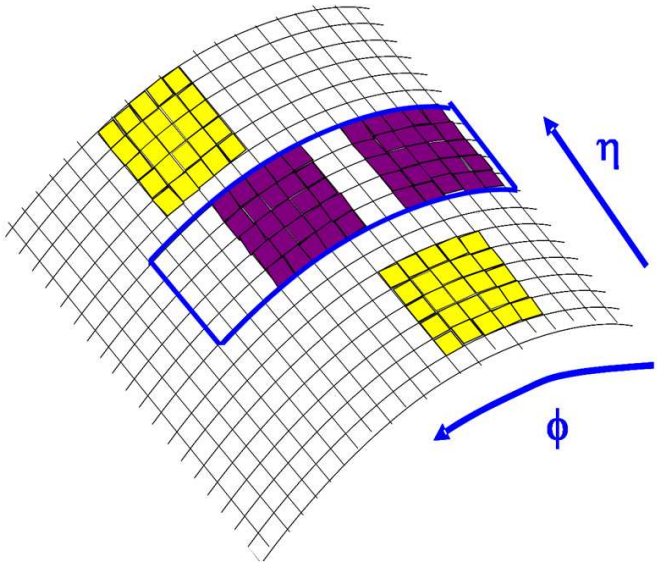

Figure 4.2: A supercluster algorithm searches in the ϕ direction and collects all calorimetric clusters to form a supercluster.

endcap*[34].

4.2.2 Electron Tracking

Finding pixel seeds is the first step in the track reconstruction. The position of an ECAL supercluster defines the search region in the pixel detector. If at least two pixel hits are found then these are used, along with hits in the silicon strip tracker, to build and fit electron tracks. Dedicated algorithms are used to reconstruct electron tracks as they can lose a large proportion of their energy due to bremsstrahlung which affects the shape of the trajectory. A Gaussian sum filter (gsf) algorithm is used for this purpose in CMS as it allows improved pattern recognition and the radiating track hits can be followed right through the tracker [33], [52].

4.2.3 Track-supercluster combination

In the preselection step selection criteria are imposed on the track-supercluster pair and a reconstructed electron candidate is formed if the pair meets the criteria. Electron candidates must have a reconstructed electron track seeded by a supercluster that is matched to hits in the pixel detector, the supercluster and the track must be matched geometrically and an upper limit is also placed on E_{SC}/P_{track}†. In addition to this, a constraint is placed on the E_{HCAL}/E_{ECAL}‡ to remove fake electrons.

The momentum of the electron track and energy from the supercluster are combined to calculate the electron energy. The proportion with which the supercluster and track information is combined is dependent on which measurement has the smaller error. Therefore, at low energies the track information is given more weight than the supercluster but at high energies the opposite is true.

*It should be noted that recent changes have been made to the endcap clustering algorithm to make it more effective for reconstructing very high energy EM objects ($> 200 GeV P_T$). The low energy behaviour is essentially the same as the island algorithm.

†The supercluster energy divided by the track momentum.

‡The energy deposited in the HCAL divided by the energy deposited in the ECAL.

4.2.4 Electron Isolation and Identification

An electron candidate is just the starting point for most analyses involving electrons. Subsequent criteria will be imposed on the candidates to reduce the probability of fakes. The tightness of the criteria will depend on the analysis in question. Common requirements are electron isolation and identification (which has various choices; Robust, Loose and Tight). These requirements and the efficiencies associated with them are described in detail in Chapter 5 of this thesis.

4.2.5 Electron Selection

Electron triggers employ only the ECAL at the level 1 trigger (L1T) and information from tracker, ECAL and HCAL for the high level trigger (HLT). There are three types of L1T: single isolated, double isolated and double, where single/double means that the L1T criteria are applied to one/two energy deposit/s in the ECAL. If an electromagnetic object passes L1T then it is passed to the HLT which uses the following selection criteria[§]:

- Matching of supercluster with hits in the pixel detector.
- Electron isolation.
- E_{SC}/P_{track} matching.

4.2.6 Summary

The steps involved in electron reconstruction and selection have been described briefly in order to introduce the concepts that will be referred to frequently throughout the rest of this thesis.

[§]The specific quantities for the selection criteria have not been given as the values are subject to change at present.

4.3 Test Beam Analysis

4.3.1 Overview

In summer 2006 nine ECAL supermodules were exposed to an electron beam at H4 Prevessin, CERN to test their response and understand more about how they will operate in CMS. All nine supermodules were intercalibrated during this period. Many studies were performed to test the final versions of the readout electronics, high and low voltage, cooling system, temperature and laser monitoring, data acquisition and data quality monitoring.

Energy scans were performed at different pseudorapidity (η) during the test beam period and results have been used to investigate the variation of the fraction of energy deposited within a cluster of crystals as a function of η. The results from the test beam are compared with those from simulation [53] and are presented in this section.

4.3.2 Test Beam Setup

The supermodules were mounted on a rotating table reproducing the pseudo-pointing geometry of CMS. The main differences between CMS and the test beam are the absence of tracker material in front of the ECAL and the absence of the magnetic field. Specific simulation software has been used to compare to the data.

4.3.3 Selecting Electron Events

A scintillating fibre hodoscope is used to track the electrons in order to determine the impact position on the crystal surface (Fig. 4.3). It consists of two sets of scintillating fibre planes, each set consisting of two planes orientated at right angles to each other. The sets of planes are placed $2.5m$ apart and measurements of X and Y are made at each set of planes. Due to the absence of any magnetic field the electrons do not bend and the track can be easily extrapolated to the surface of the

crystal using these two sets of co-ordinates. The position resolution achieved at the crystal face is approximately 250μm in both X and Y directions.

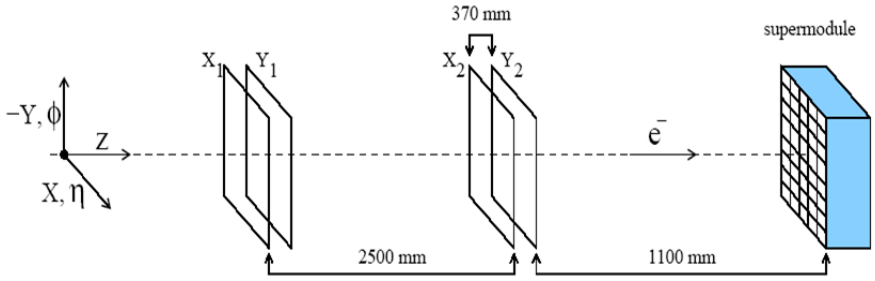

Figure 4.3: A schematic of the hodoscope planes within the experimental set-up in the H4 beam line at CERN.

The Molière radius of lead tungstate is 2.2cm, so an electromagnetic particle deposits a large proportion, but not all, of its energy in a single crystal. Electrons do not emit bremsstrahlung in the test beam so simply summing the energy of crystals around the seed is sufficient to collect the energy of the shower. Results were obtained for arrays of 3x3 and 5x5 crystals.

Figure 4.4 shows the energy deposited in the seed crystal is dependent on electron impact position. The closer the incident particle is to the edge of a crystal the lower the fraction of energy contained in this crystal. The maximum energy fraction does not occur when the particle impacts in the middle of the front face of a crystal as the crystals are off-pointing. The position of maximum containment is found using the peak in the response. A second order polynomial fit is performed on the data to find this maximum for X and Y separately.

To investigate possible trends in energy containment over the entire supermodule only events where electrons hit the crystal close to the maximum containment point are selected. The dashed lines on Figure 4.4 represent hodoscope cuts 2mm either side of maximum containment position, only electrons that impact within this 16mm^2 window are used.

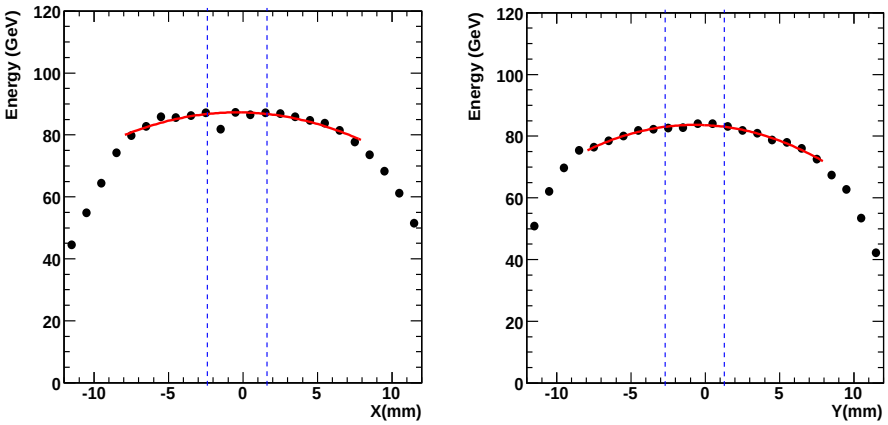

Figure 4.4: The crystal response versus the impact position of the impinging electron on the crystal face for the X (left) and Y (right) coordinate. The result of the fit with a 2nd degree polynomial is superimposed (solid line).

4.3.4 Dependence of Energy Containment on Pseudorapidity

Energy containment, $E1/EN$, is defined as the energy collected in the seed crystal divided by the energy collected in an array of N crystals centred on the seed. Figure 4.5 shows how energy containment varies as a function of pseudorapidity for supermodule 22 for which the electron beam energy was $120GeV$. The plot shows the ratios $E1/E9$ and $E1/E25$ from the test beam data compared with that from simulation. An obvious trend in containment vs. η is observed, the shape of which is represented very well by the simulation.

At the module boundaries a jump in both the $E1/E9$ and $E1/E25$ is evident in correspondence with gaps between the ECAL modules. These gaps result in a decrease in the thickness of the ECAL seen by the shower as shown in Figure 4.6. Therefore, less energy is contained in an array of N crystals while the energy in a single crystal is not affected.

The plot also shows an offset between data and simulation which has been investigated. Different versions of the electromagnetic shower model employed in the simulation change this offset. The important thing is that the shape of the data is well reproduced in the simulation.

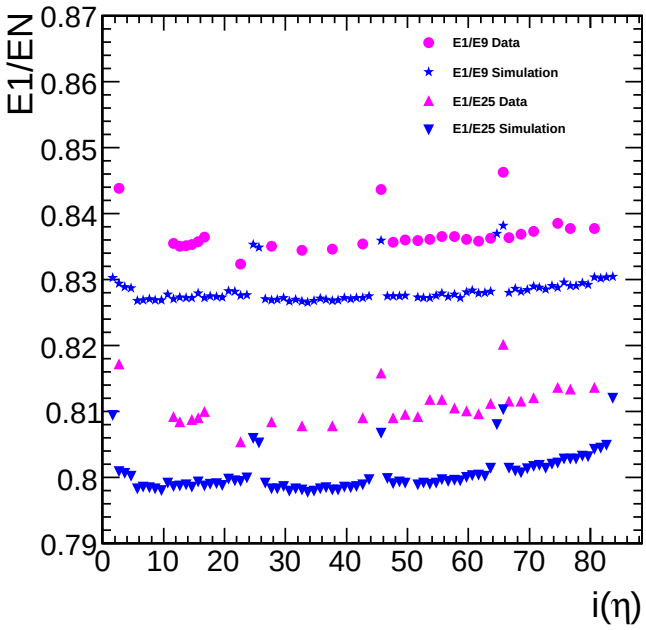

Figure 4.5: Energy containment vs. η for E1/E9 and E1/E25 for barrel supermodule 22, i represents crystal number. One supermodule spans one half of the central part of the CMS detector ($0 < \eta < 1.45$).

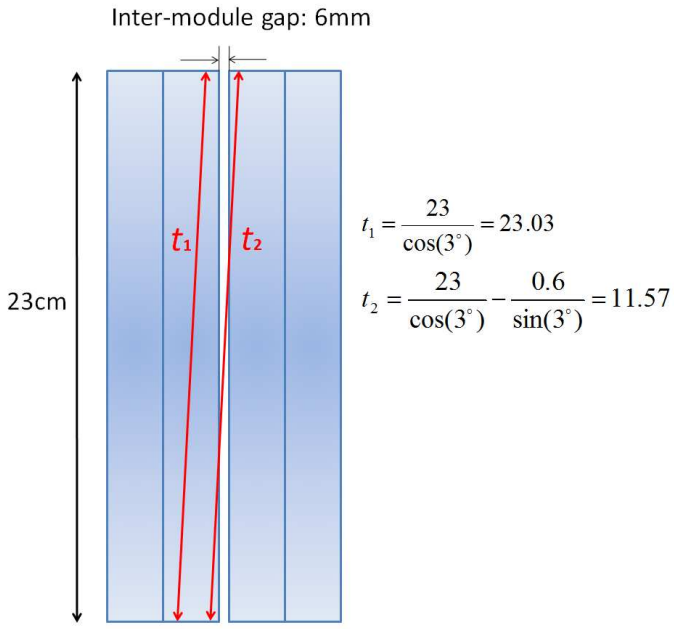

Figure 4.6: Schematic showing how the ECAL thickness (in cm) is affected by the presence of inter-module gaps.

Crystals are gradually tilted toward higher pseudorapidity which means that at high η their front faces are not aligned with neighbouring crystals as they are at $\eta \sim 0$ (Fig. 4.7). Leakage of some of the shower occurs through the exposed edge of the crystal into empty space in front of the adjacent crystal where the energy can not be recovered. The more tilted the crystals the more leakage occurs. It is this geometrical effect that is responsible for the gradual increase in shower containment with increasing pseudorapidity as it has the effect of decreasing the energy collected in an array of crystals.

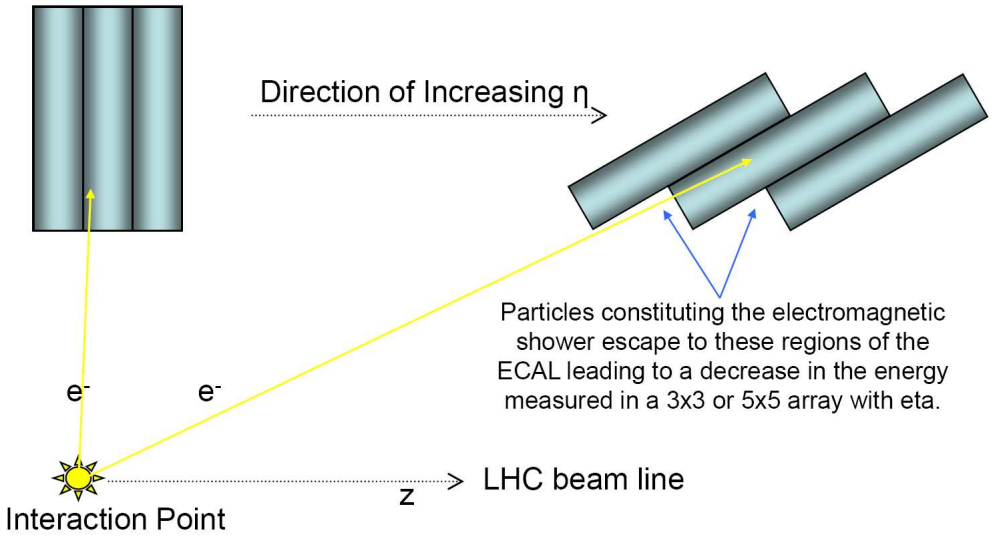

Figure 4.7: A schematic showing the orientation of crystals in the CMS ECAL η.

4.4 Optimising Electromagnetic Shower Depth Parameter

CMS software requires rigorous testing and optimising during development and efforts to validate the porting of reconstruction algorithms to this new software framework are ongoing. This section details a study by the author to ensure that the position calculation of superclusters in the ECAL is correctly implemented. It should be noted that this study was performed separately for photons and electrons as they shower at different depths but only results for electrons are detailed.

As described previously, the starting point for the reconstruction of an electron is a supercluster. If the position in η and ϕ of this supercluster is not correct then this will affect the rest of the reconstruction chain by adversely affecting the pixel hit search and the supercluster-track matching and making the supercluster-track pair less likely to become an electron candidate.

This study compares η_{SC} with $\eta_{detector}$ to calculate the depth of an electromagnetic shower. $\eta_{detector}$ is obtained from the generator level electron with the necessary transformations applied to account for bending in the magnetic field and the Gaussian spread of interaction vertices. For this study $35GeV$ electrons produced in CMSSW were used so that results could be compared with similar studies conducted using old versions of CMS software [3].

Due to the off pointing geometry of crystals in the ECAL the position of the crystal axis in η and ϕ is dependent on depth. The depth of an electromagnetic shower is defined as the distance between the front face and the shower maximum (Fig. 4.8) and is calculated using the following formula:

$$depth = X_0 \left(T_0 + \ln E\right) \tag{4.1}$$

where X_0 is the radiation length, T_0 is the depth parameter and E is the energy in GeV.

Crystals are off-pointing in the opposite direction for positive η with respect to negative η, therefore, an inaccurate calculation of the depth will result in η_{SC} being shifted from the true value in opposite directions for positive and negative halves of the detector. This can be exploited to calculate the depth parameter of an electromagnetic shower but before giving details an explanation of supercluster position is given.

4.4.1 Position Calculation of ECAL Clusters and Superclusters

The position of an individual cluster can be calculated using the weighted mean position of the crystals within that cluster using the following equation:

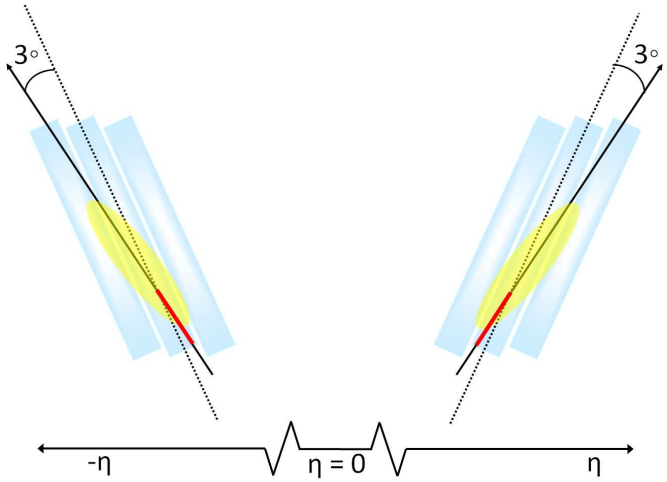

Figure 4.8: Schematic of the ECAL crystals in positive and negative η regions of the detector, the red line shows the shower depth.

$$x = \frac{\sum x_i \bullet W_i}{\sum W_i} \tag{4.2}$$

where x_i is the position in η_i, ϕ_i of crystal i at the depth calculated using Equation 4.1, and W_i is the log weight of the crystal defined as:

$$W_i = W_0 + \ln\left(\frac{E_i}{\sum E_j}\right) \tag{4.3}$$

where W_i is set to zero if it is negative and W_0 controls the smallest weight a crystal can have and still contribute to the energy measurement.

The position of a supercluster is calculated as the energy weighted mean of its constituent clusters.

4.4.2 Calculation of Depth Parameter

The depth parameter, T_0, is found by calculating the offset in mean of the $\eta_{SC} - \eta_{detector}$ distribution for each half of the detector separately, an example is given in Fig. 4.9. The mean value of η_{SC} - $\eta_{detector}$ should be the same for both halves if the depth parameter is set to the correct value. The plots shown in Figures 4.10,

4.11, 4.12 display the variation in the mean offset vs. the depth parameter (T_0) for positive and negative halves of the detector separately. In many cases the errors are small and therefore the error bars are obscured by the markers. The optimal values of T_0 occur where the linear fits cross and are given in the caption for each detector region: barrel, endcap without preshower, endcap with preshower.

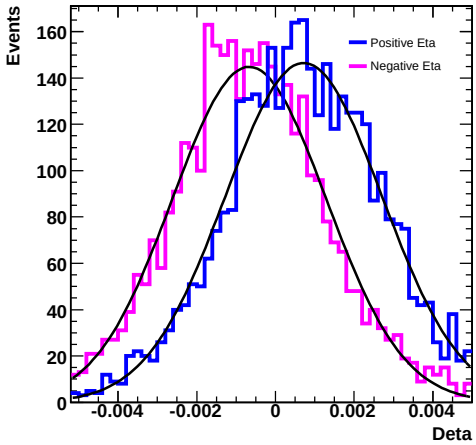

Figure 4.9: The difference between supercluster (SC) η and detector η for positive and negative η regions of the ECAL endcap behind the preshower.

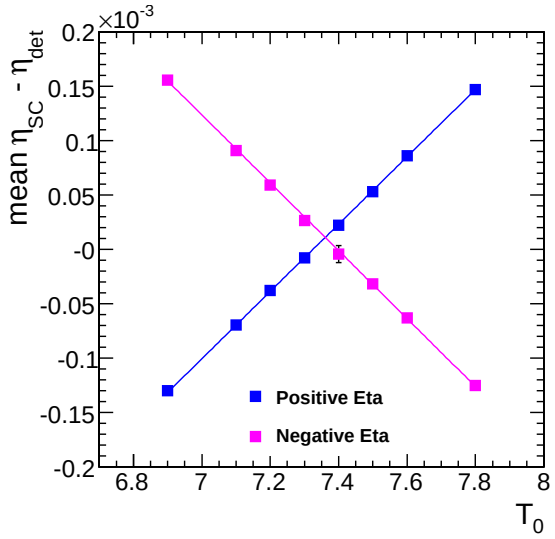

Figure 4.10: Mean $\eta_{SC} - \eta_{detector}$ vs. depth parameter T_0 in the ECAL barrel. In addition to the uncorrelated errors shown on the plot there is a correlated error of 1.5×10^{-5} which is not shown in the error bars. The optimal $T_0 = 7.36 \pm 0.07$ corresponding to mean $\eta_{SC} - \eta_{detector}$ of $1.1 \times 10^{-5} \pm 2.1 \times 10^{-5}$ which is consistent with zero.

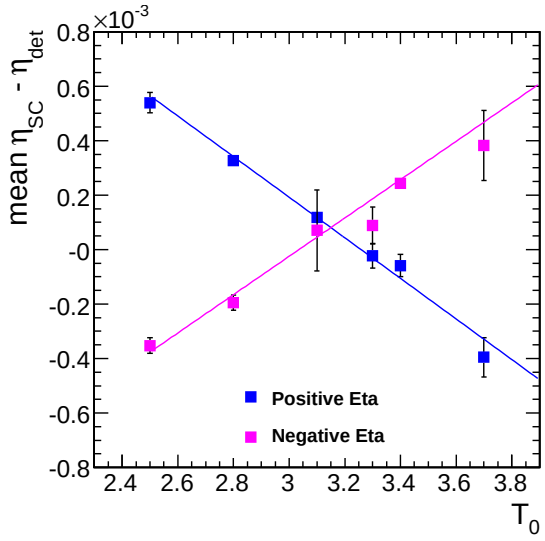

Figure 4.11: Mean $\eta_{SC} - \eta_{detector}$ vs. depth parameter T_0 in the ECAL endcap without preshower. In addition to the uncorrelated errors shown on the plot there is a correlated error of 1.1×10^{-4} which is not shown in the error bars. The optimal $T_0 = 3.15 \pm 0.15$ corresponding to mean $\eta_{SC} - \eta_{detector}$ of $8.1 \times 10^{-5} \pm 1.1 \times 10^{-4}$ which is consistent with zero.

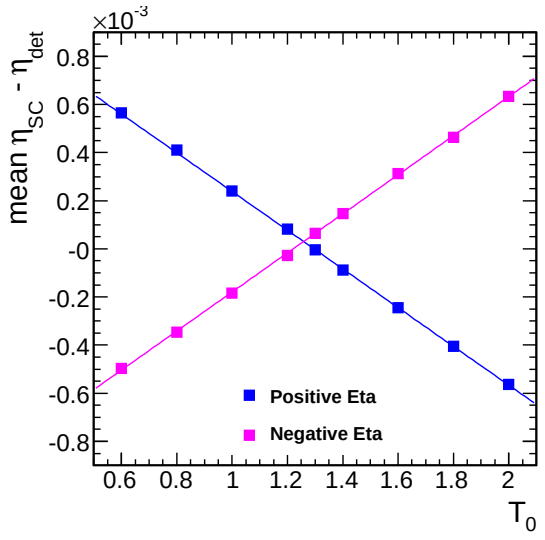

Figure 4.12: Mean $\eta_{SC} - \eta_{detector}$ vs. depth parameter T_0 in the ECAL endcap behind the preshower. In addition to the uncorrelated errors shown on the plot there is a correlated error of 3.3×10^{-5} which is not shown in the error bars. The optimal $T_0 = 1.26 \pm 0.04$ corresponding to mean $\eta_{SC} - \eta_{detector}$ of $3.1 \times 10^{-5} \pm 3.3 \times 10^{-5}$ which is consistent with zero.

4.4.3 ECAL Position Resolution

Using these results the ECAL position resolution can be calculated. Figures 4.13 and 4.14 show this for electrons and positrons separately. Figure 4.15 shows the total position resolution (electrons and positrons together) for the barrel region of the ECAL. The plots show a Gaussian spread peaked at zero plus tails in ϕ where the tails are due to the larger uncertainty associated with the supercluster ϕ measurement for electrons that have emitted bremsstrahlung. These results agree with previous studies done with old CMS software [3]. This part of the electron reconstruction chain can now be considered validated.

Figure 4.13 shows $\phi_{SC} - \phi_{detector}$ for electrons and positrons separately. The plots are the same apart from a more pronounced tail on the negative side for positrons and the positive side for electrons. The schematic showing electrons bending in the CMS tracker shows that this effect occurs when the bremstrahlung is not fully recovered during superclustering and therefore ϕ_{SC} is biased in opposite directions for electrons and positrons.

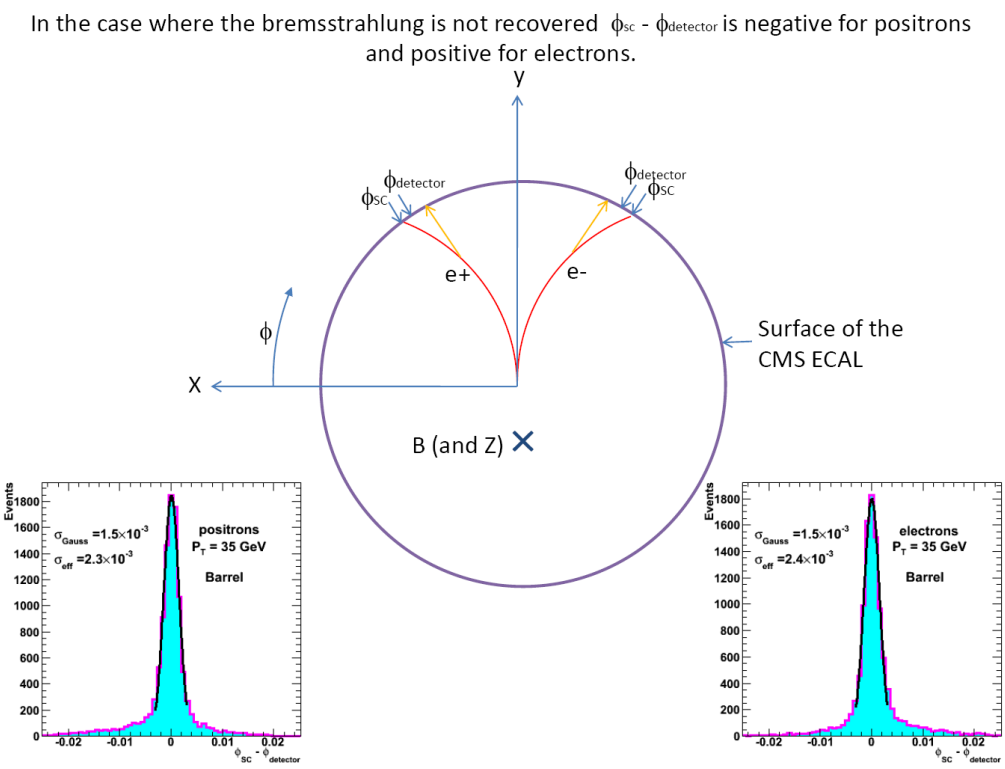

Figure 4.13: Schematic showing electrons and positrons bending and producing bremsstrahlung in CMS. Plots of $\phi_{SC} - \phi_{detector}$ for electrons and positrons separately are included.

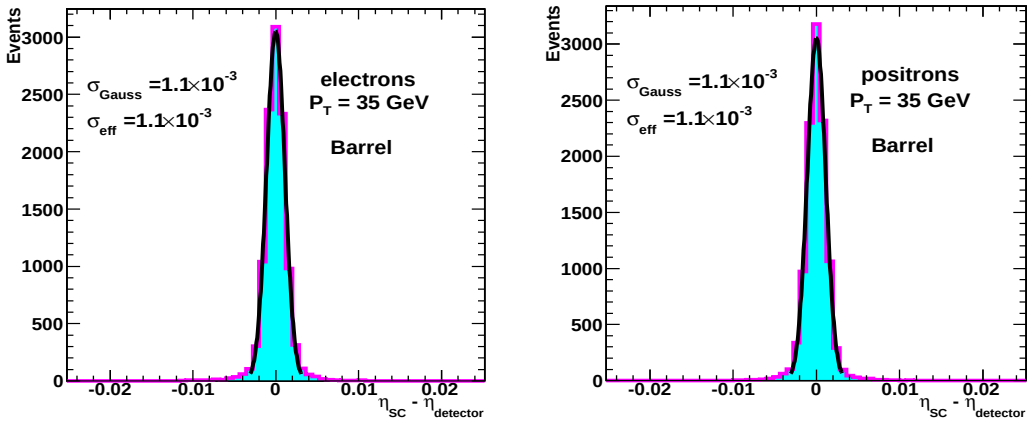

Figure 4.14: Position resolution for the barrel in η for electrons (left) and positrons (right).

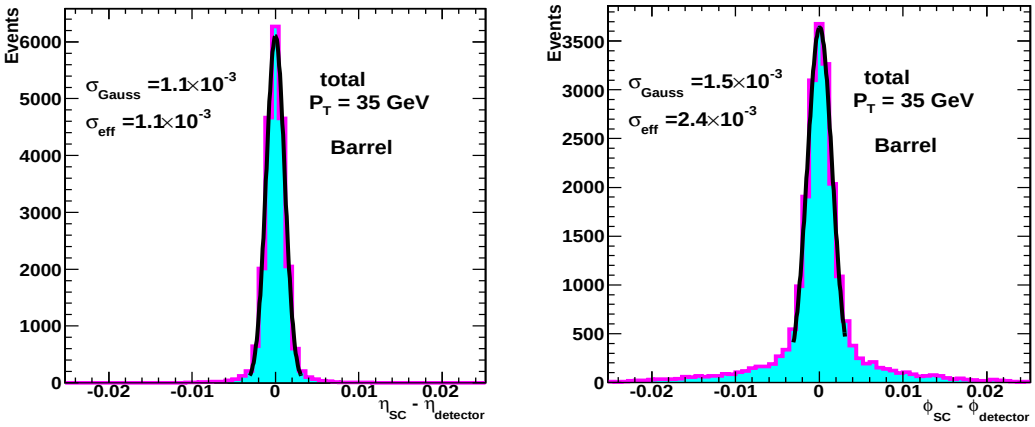

Figure 4.15: Total position resolution for the barrel in η (left) and ϕ (right).

Chapter 5

Measuring Electron Efficiencies at CMS using Early Data

Electrons can be well measured and identified in CMS and many Standard Model and beyond Standard Model physics processes produced at the LHC will result in their production. It is therefore necessary to measure precisely the efficiency with which an electron produced in CMS is fully reconstructed and selected. This chapter details the methods developed to achieve this measurement with early data ($10pb^{-1}$) which require no dependence on Monte Carlo information. Generator level information is only accessed during this analysis to rigorously test that the method is unbiased.

5.1 Tag and Probe Method

The method employed to measure electron efficiencies is termed the tag and probe method. It exploits the fact that the invariant mass of electrons produced in $Z \rightarrow e^+e^-$ events will fall in a narrow range around M_Z to select a high purity, unbiased sample of probes with which to measure online and offline reconstruction efficiencies.

5.1.1 Procedure for Selecting a Sample of Probes

The specific steps for selecting probe superclusters are as follows (Fig. 5.1):

1. If there is a well reconstructed electron in the event that passes electron identification and the single electron isolated HLT this is given tag status.

2. The tag-supercluster invariant mass is calculated for all superclusters (SC) in the event except the one belonging to the tag. If there is exactly one such supercluster that satisfies $85GeV < M_{tag-SC} < 95GeV$ then this is a probe.

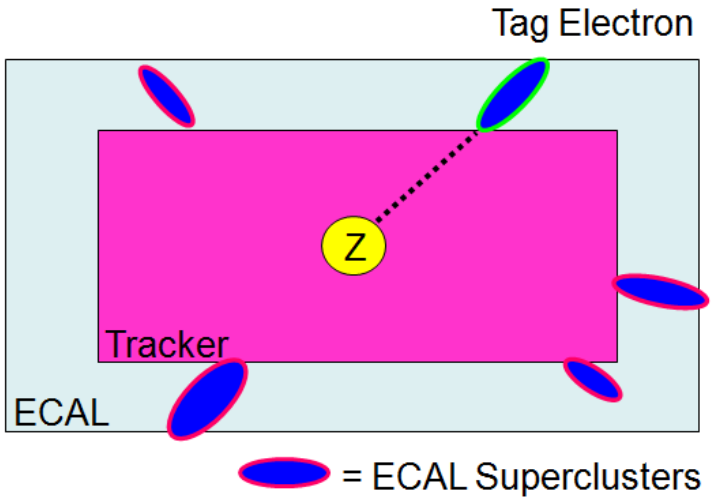

Figure 5.1: Schematic of the tag and probe method.

The tight criteria on the tag along with a strict invariant mass requirement on the tag-probe pair is sufficient to obtain a high purity sample. If there are two possible tags in an event then both are used to search for probes, implying that one $Z \rightarrow e^+e^-$ event could produce zero, one or two probes, which is elaborated upon in Section 5.2.3.

5.2 Measuring Efficiencies

The use of the tag and probe method has been studied in the context of its use in early data taking so sample sizes corresponding to $10pb^{-1}$ have been used which is consistent with the cross-section studies carried out in the next chapter. It is hoped that this amount of data from the LHC will be available before the end of 2008, depending on startup conditions.

5.2.1 Factorisation Scheme

The sample of probes selected using the tag and probe method has been used to measure the efficiency with which an electron will be fully reconstructed, identified and selected relative to an appropriate set of acceptance criteria*. The efficiency measurement must be split into constituent parts so that each step can be investigated and validated. The order in which cuts are applied is important and a specific order has been chosen and is shown in the following equations where efficiencies are calculated from left to right:

$$\epsilon_{total} = \epsilon_{offline} \times \epsilon_{online} \tag{5.1}$$

The offline and online efficiencies are further factorised:

$$\epsilon_{offline} = \epsilon_{preselection} \times \epsilon_{isolation} \times \epsilon_{identification} \tag{5.2}$$

$$\epsilon_{online} = \epsilon_{L1+HLT} \tag{5.3}$$

where each component is defined as follows:

- $\epsilon_{preselection}$ = the efficiency of preselection for an electron object.
- $\epsilon_{isolation}$ = the efficiency that a preselected electron is isolated.
- $\epsilon_{identification}$ = the efficiency of an isolated electron passing preselection to be identified as an electron. This could use Robust, Loose or Tight identification criteria depending on the requirements of individual analyses.

*In this study the probe is required to be in the fiducial region of the electromagnetic calorimeter and also the have transverse energy (E_T) above $20GeV$. These are appropriate cuts for the measurement of the $Z/\gamma^* \rightarrow ee$ and $W \rightarrow e\nu$ cross-sections detailed in the next chapter. It is important to note that for other analyses different acceptance cuts may be appropriate so the tag and probe tools developed by the author are flexible enough to recalculate electron efficiencies with respect to any value of cut on η and/or E_T quickly and simply.

- ϵ_{L1+HLT} = the efficiency of the electron meeting all offline criteria to pass the HLT. This is equivalent to the total online efficiency as only objects that meet L1T criteria get passed to the HLT.

This factorisation scheme is flexible and the order can be changed and efficiencies can be recalculated quickly and easily. Provided that correlations between efficiency measurements are taken into account, the order in which individual efficiencies are calculated should not affect the total. This has been tested and verified and the results are presented in Appendix D.

It was chosen to measure offline electron efficiencies first, followed by the online efficiency, as it is considered a more general measurement. Not all electrons in an event will pass the HLT and it is important that the efficiency for such electrons to be reconstructed and identified is known. However, the advantage of requiring the probe to pass the HLT first, before the offline cuts, would be large background rejection. Methods to deal with background subtraction have been developed and successfully employed (Section 5.2.5) allowing the offline efficiencies to be calculated first.

5.2.2 Correlation of Efficiency Measurements

In order to be able to compute the total efficiency as a product of its component parts, care must be taken to ensure there are no correlations between the steps. For example, the isolation efficiency is likely to be correlated to the identification efficiency as isolated electrons are more likely to meet the identification criteria. It is important to account for such effects. This is achieved by measuring each component of efficiency on a sample of probes that have passed all previous steps in the chain.

5.2.3 Tag-Probe Combinatorics

Any $Z \rightarrow e^+e^-$ event could result in the selection of zero, one or two possible probes. An event could potentially contain zero, one or two electrons that pass the

tag criteria and each tag will have zero or one associated probes. If a tag has more than one possible probe associated with it, these probes are not included in the sample used to calculate efficiencies.

Efficiencies measured using the tag and probe method are defined in the following way:

$$\epsilon = \frac{number\ of\ probes\ passing\ selection}{total\ number\ of\ probes} \tag{5.4}$$

Therefore, the following types of $Z \rightarrow e^+e^-$ event contribute to this measurement:

- TT: events where both electrons pass the tag criteria and their invariant mass falls within the specified window.
- TP: events where exactly one electron passes the tag criteria and the other satisfies the constraint to be classed as a probe. These events fall into two categories:
    1. TP_P: probe passes the selection criteria under investigation.
    2. TP_F: probe fails the selection criteria under investigation.

The tag criteria are tight so an event with two tags will almost always have two probes that pass all the selection criteria[†]. Events with zero tags, or events with one or two tags without associated probes do not enter into either the denominator or numerator of the efficiency calculation (Eq. 5.4) and are therefore not considered further. Considering the events that do contribute to the efficiency calculation and their relative weights leads to the following equation:

$$\epsilon = \frac{2NTT + NTP_P}{2NTT + NTP_P + NTP_F} \tag{5.5}$$

[†]There are very rare occasions where a tag will not pass all probe criteria due to a slightly lower transverse energy cut placed on the tag. Such occurrences have a negligible effect on the following discussion.

where NTT, NTP_P and NTP_F are the number of events observed of each type. TT events contribute with a weight of two with respect to TP events because they provide two probes for the sample rather than one.

Some previous tag and probe analyses have employed an event counting technique rather than counting probes as in this analysis. Allowing probes to be tags and tags to be probes means that events with two tags are counted twice because each electron is taken in turn to be classed as the tag and probes are searched for twice in one event. If both tags have associated probes then both of these are included in the efficiency measuring sample therefore Equations 5.4 and 5.5 are equivalent.

5.2.4 Monte Carlo Truth Validation of Tag and Probe Method

It is essential to verify that the sample of probes selected using the tag and probe method is unbiased since any biases, such as preferentially selecting well reconstructed superclusters, would lead to inaccurate efficiency calculations. To validate the method the efficiencies measured using the probe sample are compared to the efficiencies measured using a sample of superclusters that are geometrically matched to generated electrons from a $W \rightarrow e\nu$ sample. Providing the matching is appropriate, these Monte Carlo (MC) truth superclusters must form a truly unbiased sample. The matching criteria are $|\delta\eta_{(SC-genelectron)}| < 0.05$ and $|\delta\phi_{(SC-genelectron)}| < 0.3rad.$

Efficiency measurements have been performed on both the probe sample and the MC truth sample independently. The cuts on the tag and probe used to make these calculations are detailed in the tables in the results section (5.3). For the purpose of this comparison it is sufficient to state that the cuts applied to the probe superclusters are identical to those applied to the MC truth superclusters. For the purpose of comparing to the Monte Carlo truth a high statistics ($100pb^{-1}$) $Z \rightarrow e^+e^-$ sample has been used.

It is necessary at this point to discuss the differences in the distribution of superclusters selected using both methods. Due to the fact that the parent particles are different (W for the MC truth and Z for the tag and probe) the distribution of

the electron superclusters will be different as a function of η and E_T. Also, in the tag and probe method the request for a well reconstructed tag electron in the event influences the η and E_T distributions of the probes. Figures 5.2 and 5.3 show the distributions of tag electrons, probe superclusters and MC truth superclusters. The samples have been normalised so that the number of probe superclusters is equal to the number of MC truth superclusters.

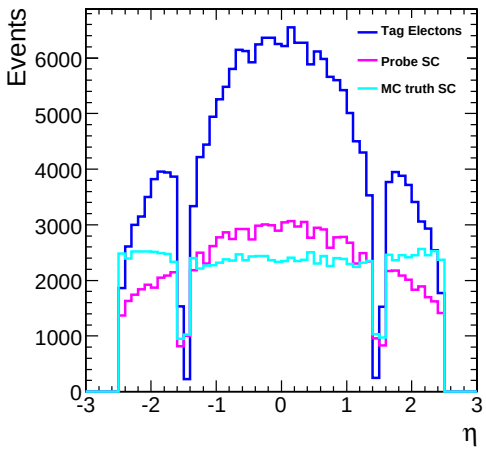

Figure 5.2: η distribution for tag electrons, probe superclusters and MC truth superclusters.

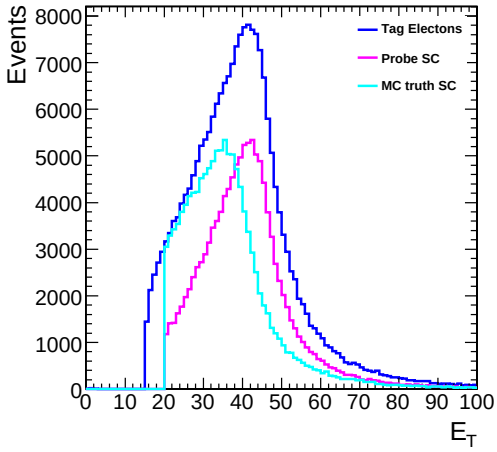

Figure 5.3: E_T distribution for tag electrons, probe superclusters and MC truth superclusters.

Many of the efficiencies in the factorisation scheme vary as a function of η and E_T so efficiencies need to be compared over small ranges in these variables. Figures 5.4 to 5.7 show the comparison between efficiencies measured using tag and probe and the MC truth method.

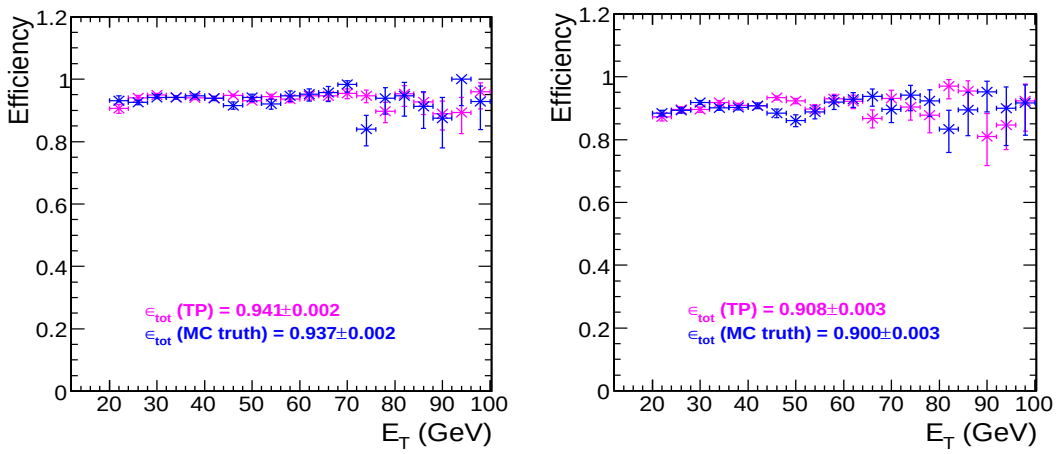

Figure 5.4: Preselection efficiency vs. E_T for $0.0 < \eta < 0.3$ and $1.6 < \eta < 1.9$ respectively.

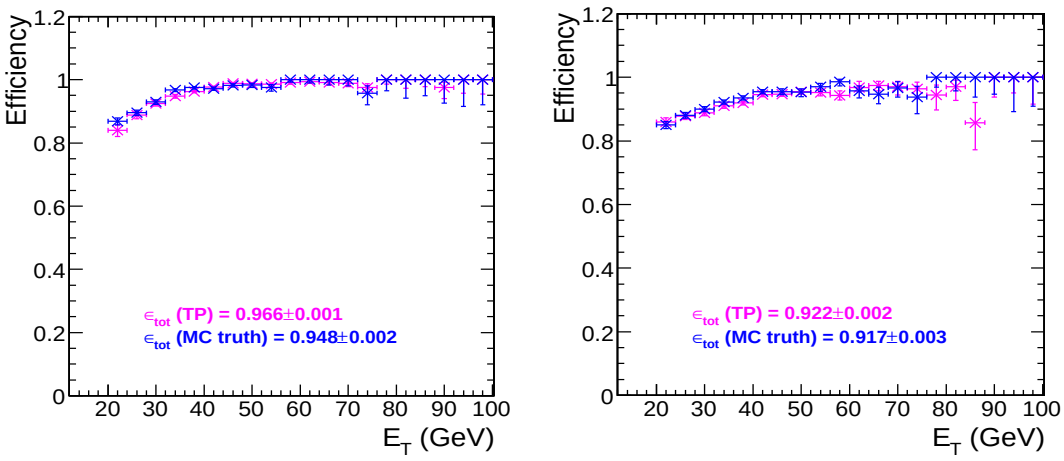

Figure 5.5: Isolation efficiency vs. E_T for $0.0 < \eta < 0.3$ and $1.6 < \eta < 1.9$ respectively.

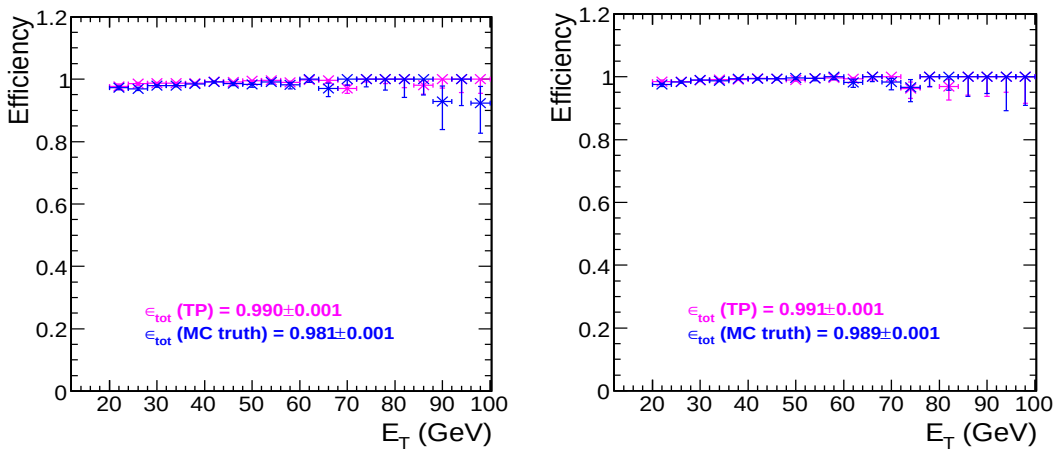

Figure 5.6: Loose identification efficiency vs. E_T for $0.0 < \eta < 0.3$ and $1.6 < \eta < 1.9$ respectively.

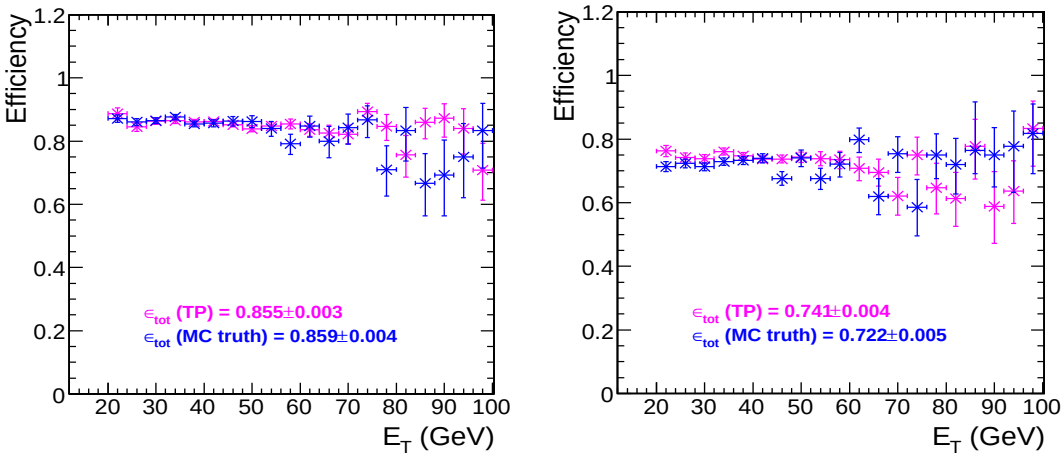

Figure 5.7: Trigger efficiency vs. E_T for $0.0 < \eta < 0.3$ and $1.6 < \eta < 1.9$ respectively.

Figures 5.4 to 5.7 show good agreement within statistical errors. Small disagreements are evident due to the fact that the η and E_T distributions of the superclusters vary within a bin and integrating over this bin produces a systematic shift in the efficiencies[‡] If it were possible to bin more finely without being dominated by statistical errors then it is expected that the efficiencies would agree exactly for each bin. It should be noted that efficiencies integrated over the whole η and E_T ranges will not agree unless the distributions of the superclusters are the same.

A further check has been made to test whether each probe supercluster is geometrically matched to a generated electron from the Z. Five thousand $Z \rightarrow e^+e^-$ events have been used for this study containing nearly three thousand probes and 100% of the probes are matched.

The tag and probe method is considered unbiased and therefore it can be used reliably to measure electron reconstruction efficiencies from data. It is important that efficiencies are provided as a function of η and E_T to be useful for many physics analyses. Efforts to make the method truly robust for LHC start-up analyses are ongoing.

5.2.5 Background Estimation and Efficiency Correction

To measure electron efficiencies accurately using a sample of probes selected using the tag and probe method it is necessary to correct for background events which come from channels such as $W \rightarrow e\nu + jet(s)$ and QCD. The presence of such background means that the probe superclusters do not all come from electrons. The sample has impurities which need to be corrected for. Applying strict criteria to the tag electron as well as requiring that the tag-probe invariant mass is close to M_Z eliminates a large proportion of background. However, it would be unwise to

[‡]Figure 5.3 shows that at high transverse energy ($E_T > 60GeV$), the distribution of probe superclusters and MC truth superclusters are very similar. However, Figure 5.2 shows that the η distributions are different and this is responsible for the discrepancies in the efficiencies in this region. A separate study was also conducted to compare efficiencies calculated using MC matched W^+ and W^- superclusters separately and small differences in the efficiencies was observed. It is therefore concluded that the tag and probe method does not introduce a bias to the efficiency measurements.

apply such tight cuts to the tag and the tag-probe pair that the probe statistics become poor. Instead, methods have been developed to subtract the background and correct the efficiency measurement accordingly.

Contamination of the probe sample becomes less prevalent at each step in the factorisation scheme (Eq. 5.2). It is quite possible that in a $W \rightarrow e\nu + jet$ event the real electron could be classified as the tag and a supercluster caused by the jet could become a probe. However, it is unlikely that this supercluster will pass the electron preselection and even less likely that it will be isolated. In the measurement described here only the first step in the offline efficiency measurement has non-negligible background which is subtracted using the sidebands technique.

Sidebands Technique

The sidebands method for performing background subtraction and subsequent correction of the efficiencies has been developed and employed as it is appropriate for use with early data. The input event sample is a mixture of signal and background events in the correct proportions to represent a realistic "data" sample for $10pb^{-1}$. Table 5.1 details the samples used. For those with weights greater than one, the tag criteria were relaxed in order to have enough probes to obtain a good background shape and then appropriately normalised.

The method is applied to all η and E_T bins to produce a matrix of background subtracted efficiencies suitable for use in other analyses. The procedure involves calculating the number of tag and probe pairs that have an invariant mass in the following regions:

1. Lower Sideband: $50 < M_{TP} < 70\ GeVc^{-2}$
2. Upper Sideband: $110 < M_{TP} < 130\ GeVc^{-2}$

and interpolating between these two regions by assuming an exponential variation of the background with M_{TP} between them as shown in Figures 5.8 to 5.11. The

Sample	Weighting applied for $10pb^{-1}$
$Z/\gamma^* \rightarrow e^+e^-$	1.0
$W \rightarrow e\nu\ \hat{P_T} : 0-15$	1.0
$W \rightarrow e\nu\ \hat{P_T} : 15-20$	1.0
$W \rightarrow e\nu\ \hat{P_T} : 20-30$	1.0
$W \rightarrow e\nu\ \hat{P_T} : 30-50$	1.0
$W \rightarrow e\nu\ \hat{P_T} : 50-80$	1.0
$W \rightarrow e\nu\ \hat{P_T} : 80-120$	1.0
$W \rightarrow e\nu\ \hat{P_T} : 120-170$	1.0
$W \rightarrow e\nu\ \hat{P_T} : 170-230$	1.0
$t\bar{t}$	1.0
$b\bar{b}\ \hat{P_T} : 5-50$	9.30
$b\bar{b}\ \hat{P_T} : 50-170$	1.0
$b\bar{b}\ \hat{P_T} :> 170$	1.0
$di-jet\ \hat{P_T} : 25-50$	19.69
$di-jet\ \hat{P_T} : 50-170$	10.29
$di-jet\ \hat{P_T} :> 170$	1.0
$Z/\gamma^* \rightarrow \tau^+\tau^-$	1.24

Table 5.1: Table of signal and background samples used in the $10pb^{-1}$ "data" sample. P_T values given in GeV.

number of background events in the signal mass range is estimated for both the sample of all probes and separately for those probes passing electron preselection. From this a background subtracted efficiency measurement can be produced using the following equation:

$$\epsilon = \frac{N_{pass} - NBG_{pass}}{N_{tot} - NBG_{tot}} \tag{5.6}$$

where N is the number of probes from the "data" sample and NBG is the calculated number of BG probes in the signal mass range; *tot* refers to all probes and *pass* refers to those passing preselection.

The assumption is made that the sideband regions are far enough away from the signal window ($85 < M_{TP} < 95\ GeVc^{-2}$) that they only contain tag and probe pairs that come from background channels. This suffers from the fact that signal dielectron events from γ^* will be prevalent outside the signal mass window, especially

in the lower sideband, and will therefore be subtracted. However, this should not affect the calculation of electron efficiencies, it just means that signal events are removed causing a small reduction of statistics.

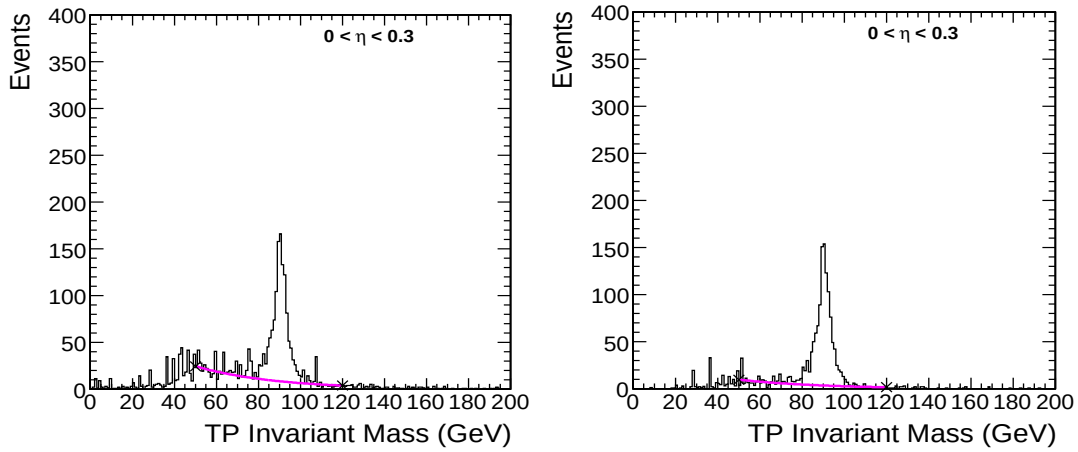

Figure 5.8: Tag-probe invariant mass for $0.0 < \eta < 0.3$ for all probes (left) and all probes passing preselection (right).

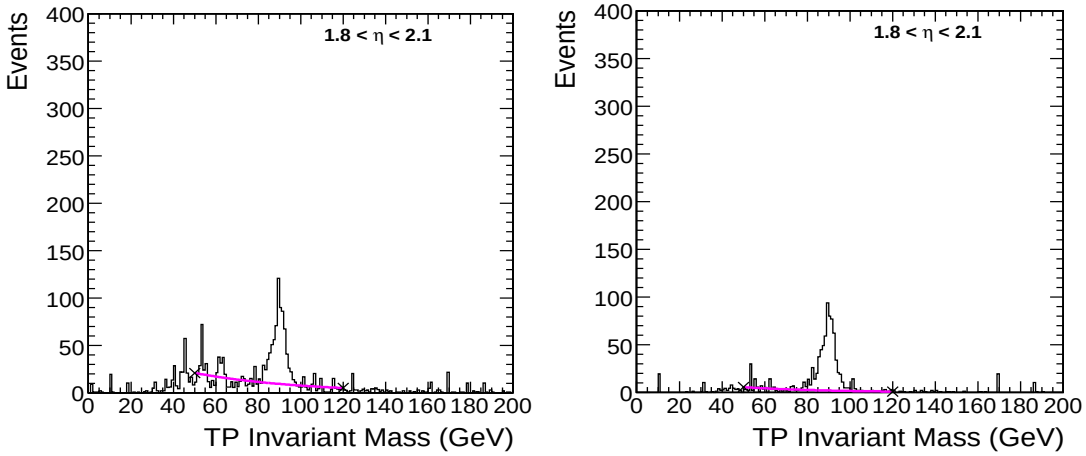

Figure 5.9: Tag-probe invariant mass for $1.8 < \eta < 2.1$ for all probes (left) and all probes passing preselection (right).

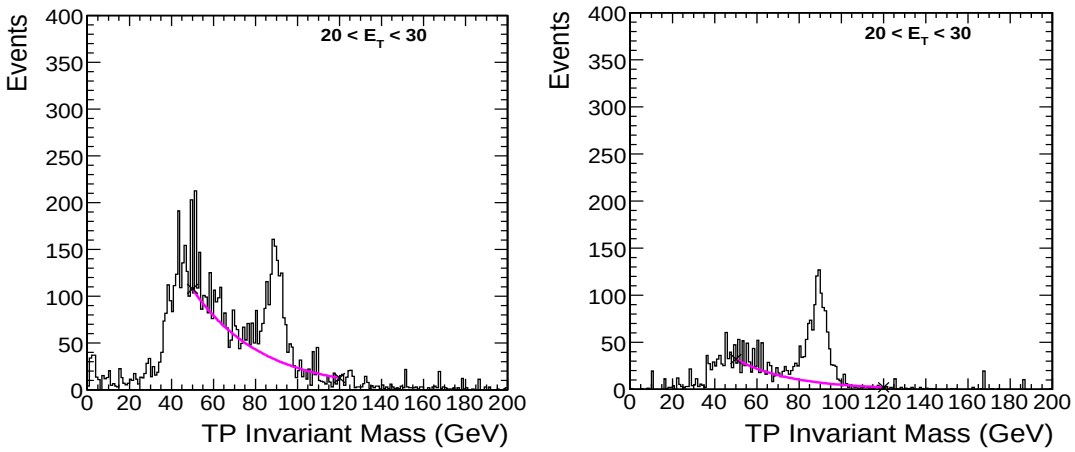

Figure 5.10: Tag-probe invariant mass for $20 < E_T(GeV) < 30$ for all probes (left) and all probes passing preselection (right).

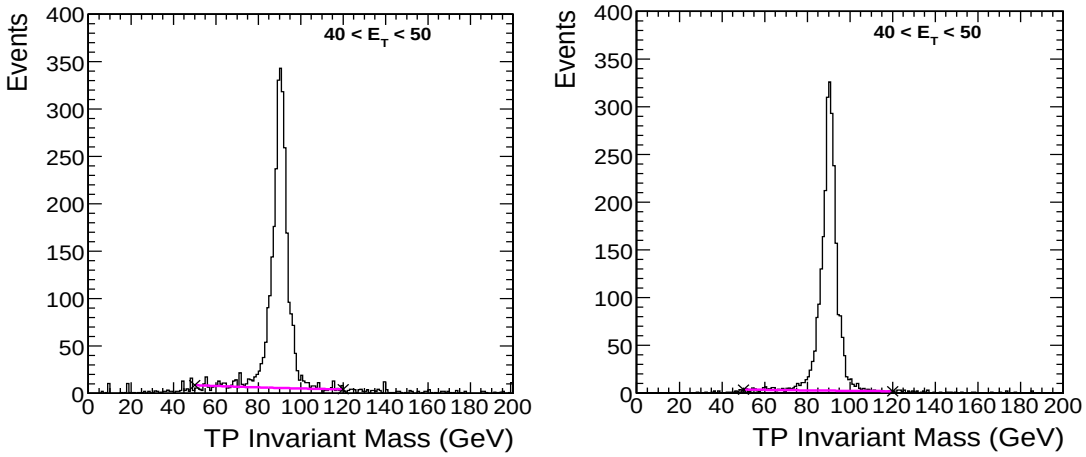

Figure 5.11: Tag-probe invariant mass for $40 < E_T(GeV) < 50$ for all probes (left) and all probes passing preselection (right).

The background subtracted efficiencies vs. η and E_T are shown in Figure 5.12. The errors are a combination of the statistical uncertainty and the systematic error introduced by the background subtraction method. The background subtracted efficiencies show good agreement with those calculated using a signal only sample.

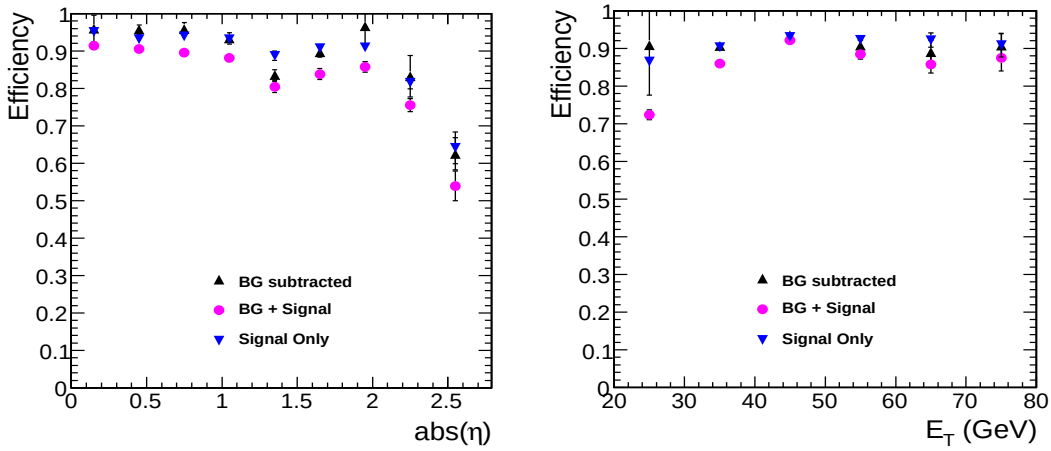

Figure 5.12: Background subtracted preselection efficiency vs η and E_T.

5.3 Efficiency Measurements

The results of all efficiencies in the chain discussed in Section 5.2.1 are given in this section. Efficiencies are dependent on the variables η and E_T and therefore plots are shown versus these variables. The equation for the total offline plus online electron reconstruction and selection efficiency follows:

$$\epsilon_{total} = \epsilon_{preselection} \times \epsilon_{isolation} \times \epsilon_{identification} \times \epsilon_{L1+HLT} \tag{5.7}$$

For each efficiency in this chain the conditions on the tag and probe are detailed and the equation used to calculate the efficiency is given. In these equations *all probes* in the denominator refers to all probes meeting the criteria given in the table. The numerator shows the efficiency under study. The tag criteria are the same for each efficiency step as the selection was considered appropriate for all measurements but this need not be the case. Each individual efficiency calculation is conducted on a

sample of probes that passed all previous selection cuts. In the preselection step the background is considered non-negligible and it has been estimated and subtracted.

5.3.1 Efficiency: Preselection

Table 5.2 shows the tag and probe criteria used for the measurement of the electron preselection efficiency. This is the first step in the factorisation scheme so the only cuts placed on the probe supercluster are geometrical and kinematic and are consistent with the cuts applied in the W and Z cross-section analyses detailed in the next chapter. Figure 5.13 shows the background subtracted preselection efficiency vs. η and E_T. The matrix of efficiencies is given in Table 6 in Appendix E.

Table 5.2: Selection criteria for tags and probes: Preselection efficiency

TAG	PROBE
A PixelMatchGsfElectron: - supercluster in ECAL fiducial: $\|\eta\|$ <1.444 and 1.560< $\|\eta\|$ <2.5 - E_T >15 GeV - isolated (track isolation) - passes Loose electron ID - passes HLT criteria - $\|TIP\| < 0.01$	A SuperCluster: - in ECAL fiducial: $\|\eta\|$ <1.444 and 1.560< $\|\eta\|$ <2.5 - E_T >20 GeV

$$\epsilon = \frac{N_{pass\ preselection} - NBG_{pass\ preselection}}{N_{tot} - NBG_{tot}} \tag{5.8}$$

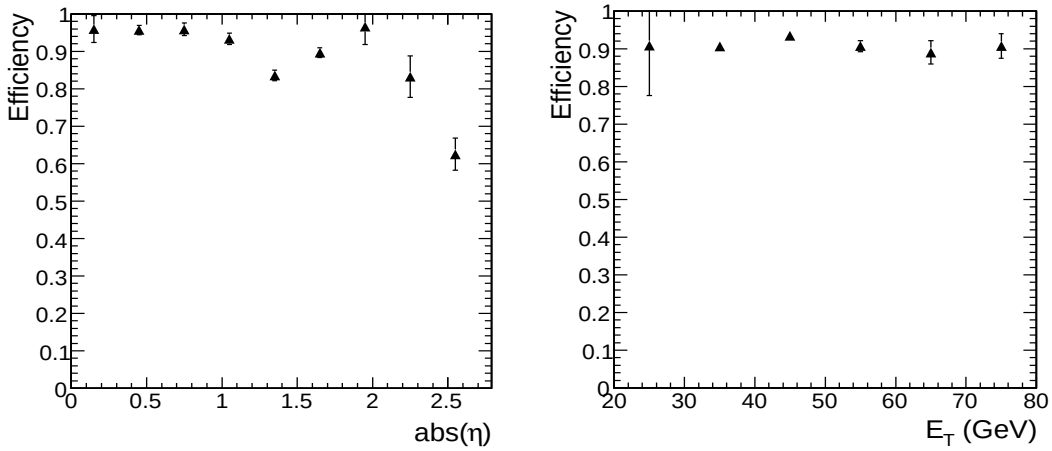

Figure 5.13: Preselection efficiency vs η and E_T.

5.3.2 Efficiency: Isolation

Table 5.3 shows the tag and probe criteria used for the measurement of the electron isolation efficiency. Isolation is defined as:

$$\sum_{track} \left(\frac{P_T^{track}}{P_T^{ele}} \right)^2 < 0.02 \tag{5.9}$$

where all CTF tracks with $P_T^{track} > 1.5GeV$ within an $\eta - \phi$ annular isolation cone centred on the reconstructed electron are summed. The cone has limits $0.02 < \Delta R < 0.6$ where $\Delta R = \sqrt{\Delta\eta^2 + \Delta\phi^2}$. P_T^{ele} is the transverse momentum of the electron at the vertex.

The probe is required to have passed preselection in addition to the geometrical and kinematic cuts. Figure 5.14 shows the isolation efficiency vs. η and E_T. The matrix of efficiencies is given in Table 7 in Appendix E.

$$\epsilon_{isolation} = \frac{probes\ that\ are\ isolated}{all\ probes} \tag{5.10}$$

Table 5.3: Selection criteria for tags and probes: Isolation efficiency

TAG	PROBE
A PixelMatchGsfElectron: - supercluster in ECAL fiducial: $\|\eta\|$ <1.444 and 1.560< $\|\eta\|$ <2.5 - E_T >15 GeV - isolated (track isolation) - passes Loose electron ID - passes HLT criteria - $\|TIP\| < 0.01$	A PixelMatchGsfElectron: - supercluster in ECAL fiducial: $\|\eta\|$ <1.444 and 1.560< $\|\eta\|$ <2.5 - supercluster E_T >20 GeV

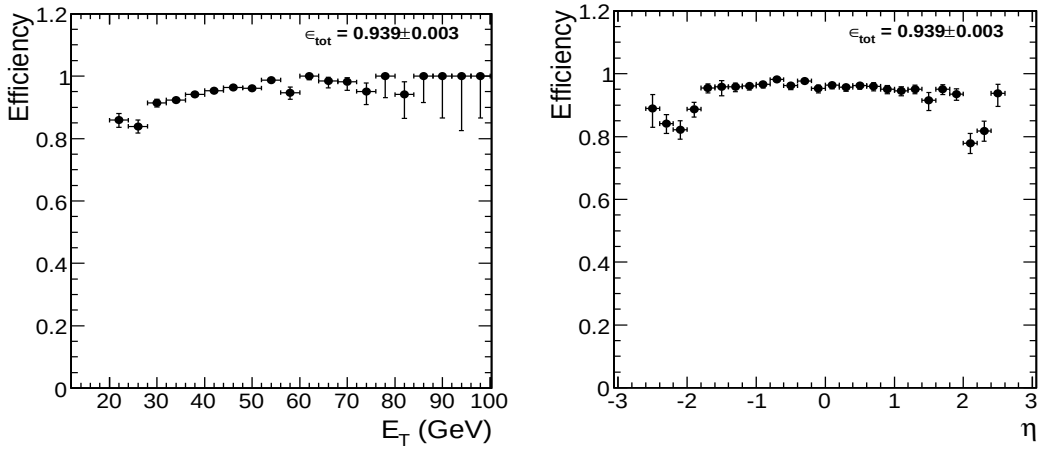

Figure 5.14: Isolation efficiency vs. E_T and η.

5.3.3 Efficiency: Identification

Table 5.4 shows the tag and probe criteria used for the measurement of the electron identification efficiency. The probe is required to have passed preselection and be isolated in addition to the geometrical and kinematic cuts. Figures 5.15 and 5.16 show the efficiency vs. η and E_T for the probe to pass 'Robust' and 'Tight' identification respectively. The matrix of efficiencies for 'Robust' identification is given in Table 8 in Appendix E.

$$\epsilon_{identification(Robust)} = \frac{probes\ that\ pass\ Robust\ electron\ ID}{all\ probes} \tag{5.11}$$

Table 5.4: Selection criteria for tags and probes: Electron identification efficiency

TAG	PROBE
A PixelMatchGsfElectron: - supercluster in ECAL fiducial: $\|\eta\|$ <1.444 and 1.560< $\|\eta\|$ <2.5 - E_T >15 GeV - isolated (track isolation) - passes Loose electron ID - passes HLT criteria - $\|TIP\| < 0.01$	A PixelMatchGsfElectron: - supercluster in ECAL fiducial: $\|\eta\|$ <1.444 and 1.560< $\|\eta\|$ <2.5 - supercluster E_T >20 GeV - isolated (track isolation)

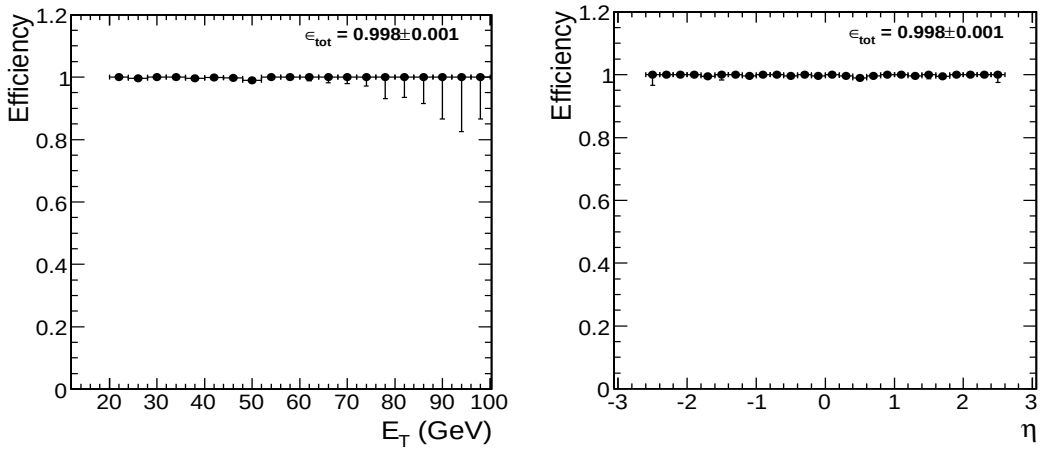

Figure 5.15: Robust electron ID efficiency vs. E_T and η.

$$\epsilon_{identification(Tight)} = \frac{probes\ that\ pass\ Tight\ electron\ ID}{all\ probes} \tag{5.12}$$

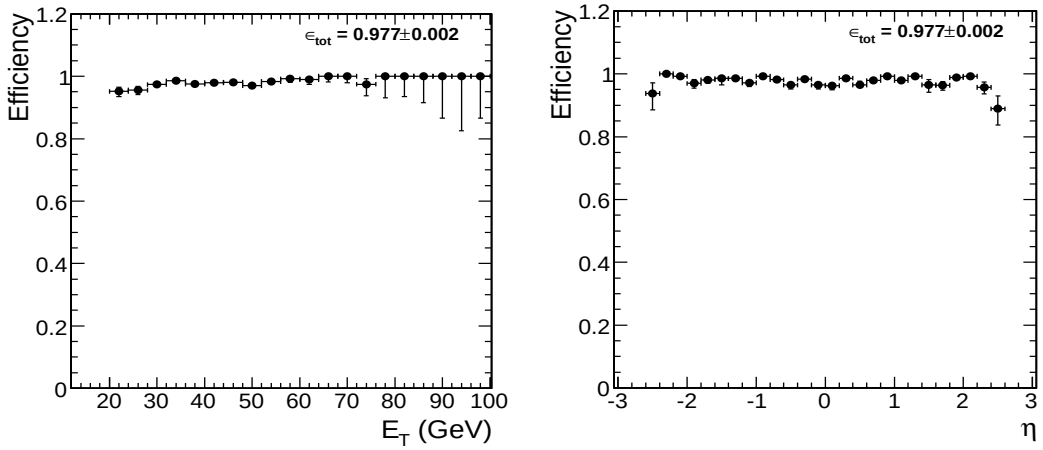

Figure 5.16: Tight electron ID efficiency vs. E_T and η.

5.3.4 Efficiency: Trigger

Table 5.5 shows the tag and probe criteria used for the measurement of the electron online efficiency. The probe is required to have passed preselection, be isolated and meet identification criteria in addition to the geometrical and kinematic cuts. Figures 5.17 and 5.18 show the efficiencies vs. η and E_T for the probe to pass the HLT with respect to 'Robust' and 'Tight' identification respectively. The matrix of online efficiencies with respect to 'Robust' identification is given in Table 9 in Appendix E.

The HLT algorithms will be optimized and are in a state of flux. Many cuts have already been loosened to be suitable for start-up conditions which has led to an increase in trigger efficency. Figures 5.17 and 5.18 show a noticable decrease in the trigger efficiency at high E_T. This is due to the cuts in the HLT algorithm being appropriate for lower E_T electrons $(30 - 50GeV)$. Constraints on E_{SC}/P_{track} and E_{HCAL}/E_{ECAL} both contribute to this inefficiency. The HLT algorithms will be optimized to correct this high E_T behaviour.

$$\epsilon_{L1+HLT(wrt\ Robust\ ID)} = \frac{probes\ that\ pass\ trigger}{all\ probes\ (Robust\ ID)} \tag{5.13}$$

Table 5.5: Selection criteria for tags and probes: Online efficiency

TAG	PROBE
A PixelMatchGsfElectron: - supercluster in ECAL fiducial: $\|\eta\|$ <1.444 and 1.560< $\|\eta\|$ <2.5 - E_T >15 GeV - isolated (track isolation) - passes Loose electron ID - passes HLT criteria - $\|TIP\| < 0.01$	A PixelMatchGsfElectron: - supercluster in ECAL fiducial: $\|\eta\|$ <1.444 and 1.560< $\|\eta\|$ <2.5 - supercluster E_T >20 GeV - isolated (track isolation) - passes electron ID

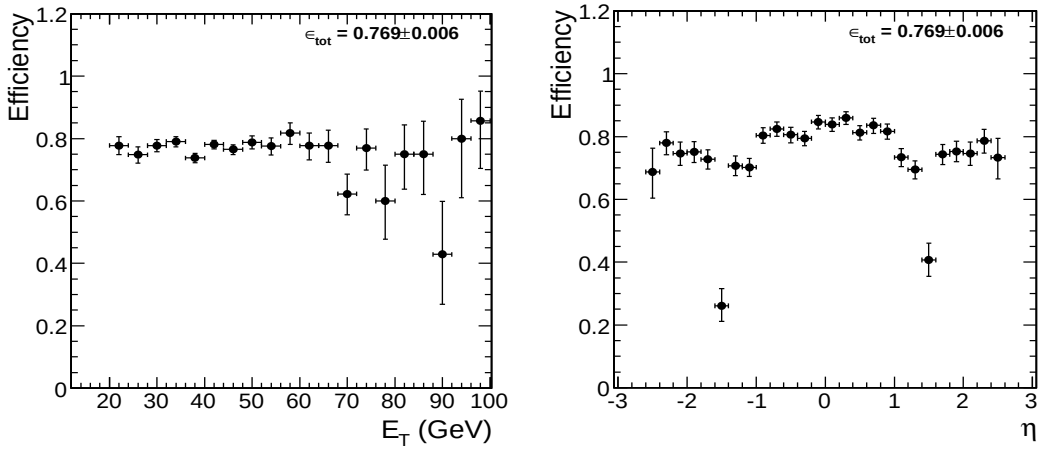

Figure 5.17: Trigger efficiency vs. E_T and η wrt Robust electron ID.

$$\epsilon_{L1+HLT(wrt\ Tight\ ID)} = \frac{probes\ that\ pass\ trigger}{all\ probes\ (Tight\ ID)} \tag{5.14}$$

5.3.5 Efficiencies as a Function of η and E_T

It is clear that efficiencies vary as a function of both η and E_T. Binning two dimensionally in these variables produces a matrix of efficiencies that can be used in generic physics analysis involving final state electrons. This has been demonstrated by using these binned efficiencies to calculate $\sigma(W) \times BR(W \rightarrow e\nu)$ [20] which is described in the final chapter of this thesis.

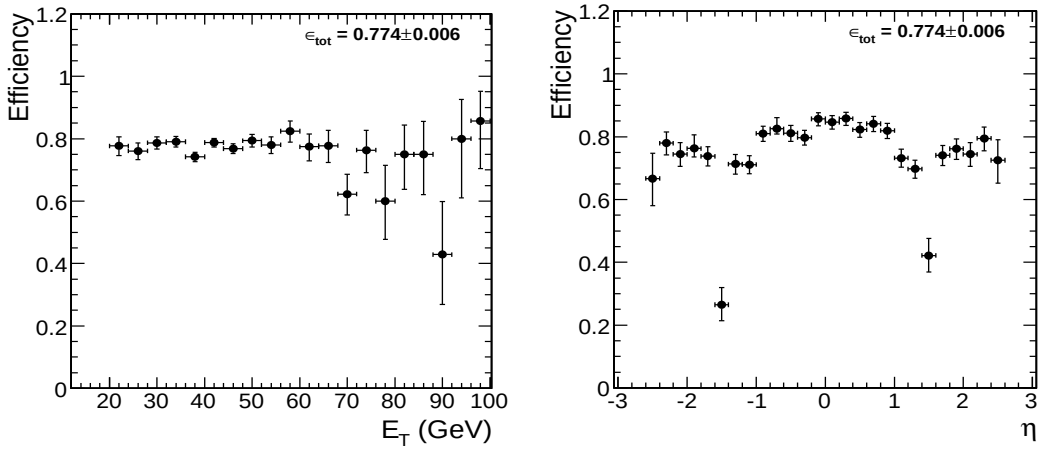

Figure 5.18: Trigger efficiency vs. E_T and η wrt Tight electron ID.

The binning chosen was to divide into 10×10 bins in the ranges $0 < |\eta| < 3$ and $0 < E_T < 100GeV$. For each efficiency measured this matrix has been calculated and the results are tabulated in appendix E.

5.3.6 Cumulative Offline and Online Efficiency

The plots in Figure 5.19 display the cumulative offline and online electron efficiencies as a function of η and E_T. The integrated value is 0.655 ± 0.006 and is dependent on event topology and in this case on the η and E_T of probe superclusters that originate from $Z \rightarrow ee$ events.

5.4 Summary

The efficiencies produced using the tag and probe method have been validated against the Monte Carlo truth efficiencies. A suitable method for subtracting the background has been developed and successfully employed. It is found that most steps in the reconstruction chain have associated efficiencies that vary as a function of η and E_T, therefore it is necessary to bin the efficiencies in these two variables in order to make them useful for analyses where the electron distributions are different

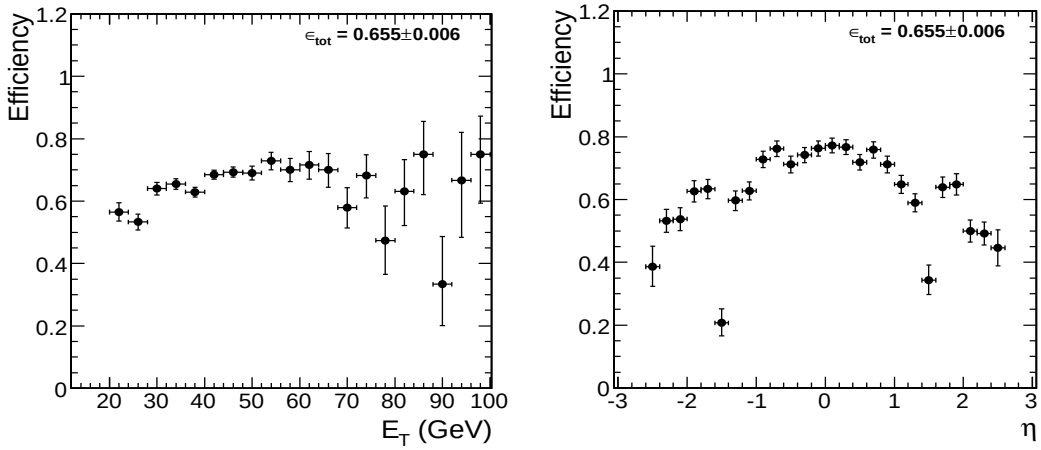

Figure 5.19: Cumulative offline and online efficiency vs. E_T and η.

from the probe distributions. The next chapter illustrates the use of these calculated efficiencies applied to the cross-section calculation of W and Z bosons in the electron decay channels.

Chapter 6

W and Z/γ^* Boson Cross-section Measurements

The production mechanisms of W and Z bosons at the LHC are well understood theoretically. Leptonic decay modes in particular will provide distinctive signatures making them useful for the commissioning of CMS and understanding leptons with early data. Measurements of the inclusive W and Z/γ^* production cross-sections will be among the first results obtained at the LHC. This chapter investigates the methods for making these measurements at CMS with $10pb^{-1}$ of data.

6.1 Weak Vector Boson Production at the LHC

The Drell-Yan process is the dominant mechanism for weak vector boson production at the LHC [54] (Fig. 6.1), where a W or Z is produced by a quark - anti-quark annihilation. Contributions to the theoretical calculation of these processes include:

- Parton cross-sections.
- Parton distribution functions.
- Higher order QCD effects.
- Couplings of the interacting partons to the W and Z bosons.

all of which have associated uncertainties that contribute to the total uncertainty on the calculation.

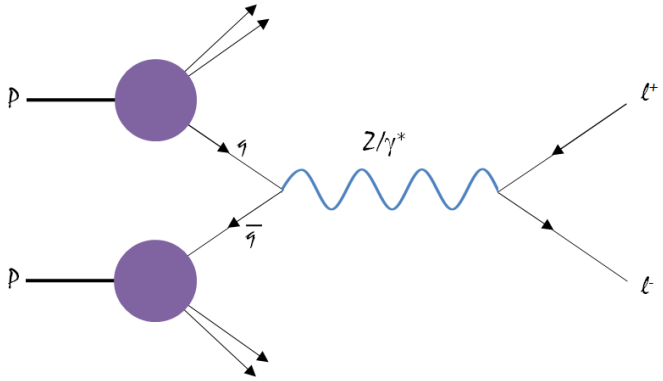

Figure 6.1: Drell-Yan process for producing weak vector bosons subsequently decaying to leptons.

W^+ and W^- are mostly produced by $u\bar{d}$ and $d\bar{u}$ respectively and Z by $u\bar{u}$ and $d\bar{d}$ (Figs. 6.2 and 6.3 [55]). The anti-quarks originate from gluons in the proton that pair produce whereas the quarks can come from gluons or from the valency. Momentum distributions of the interacting partons are the main source of uncertainty in the cross-section calculation of the weak vector bosons. Increased precision on gluon parton distribution functions has been obtained from recent measurements at HERA [56]. This contributes to a lower uncertainty on the sea quarks reducing the uncertainty on the theoretical cross-section to $\sim 3.5\%$ [57].

Low/high rapidity Ws and Zs are produced when the interacting partons have balanced/unbalanced momentum. Figure 6.4 [58] show the theoretical rapidity distributions for W and Z.

The weak vector bosons can decay to both quarks and leptons. Electron decay modes in particular produce distinctive signatures at hadron colliders and can be very precisely reconstructed in CMS. The branching fraction of the W boson to an electron and neutrino is $10.75 \pm 0.13\%$ and for Z to dielectrons is $3.363 \pm 0.004\%$ [59]. In this chapter the methods used for measurement of the inclusive W and Z/γ^* production cross-sections via these decay channels are described. Such methods are data driven but have been developed using simulated samples.

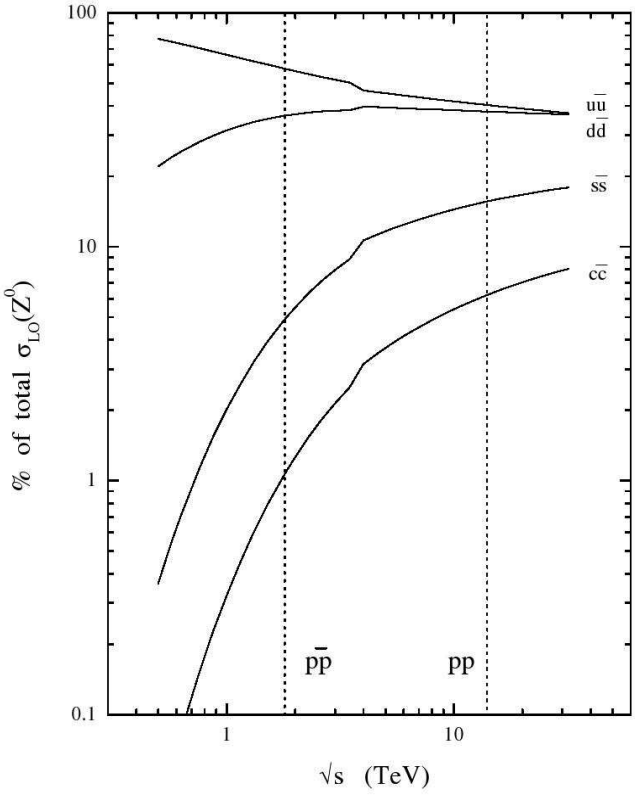

Figure 6.2: Parton decomposition of the Z total cross-section in $p\bar{p}$ and pp collisions. Individual contributions are shown as a percentage of the total cross-section in each case.

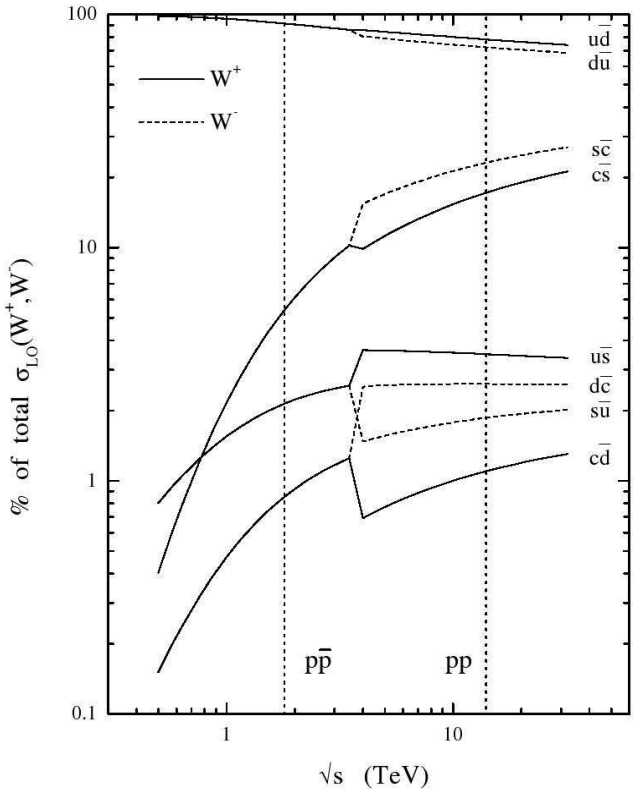

Figure 6.3: Parton decomposition of the W^+ and W^- total cross-section in $p\bar{p}$ and pp collisions. Individual contributions are shown as a percentage of the total cross-section in each case.

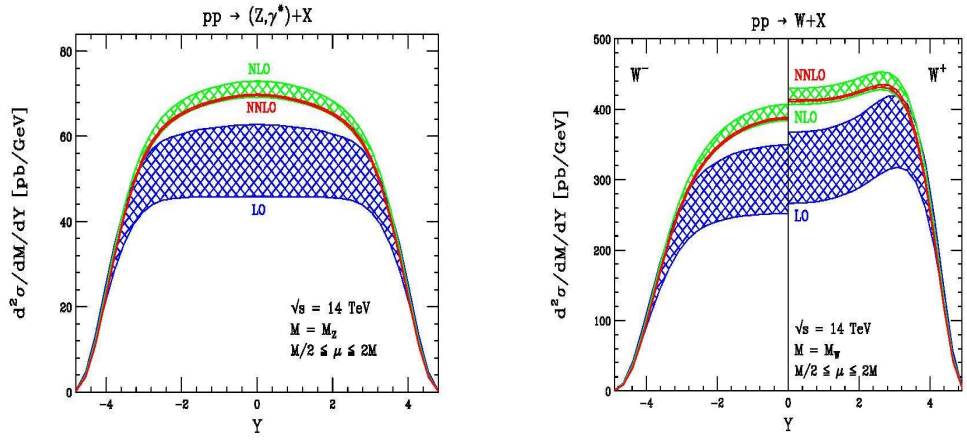

Figure 6.4: Calculated rapidity of Z and W bosons at LHC.

The Z/γ^* cross-section can be calculated using the following formula:

$$\sigma_{Z/\gamma^*} \times BR\,(Z/\gamma^* \to ee) = \frac{N^{pass}_{Z/\gamma^*} - N^{bkgd}_{Z/\gamma^*}}{A_{Z/\gamma^*} \times \epsilon_{Z/\gamma^*} \times \int Ldt} \tag{6.1}$$

A similar formula can be used for $W \to e\nu$:

$$\sigma_{W} \times BR\,(W \to e\nu) = \frac{N^{pass}_{W} - N^{bkgd}_{W}}{A_{W} \times \epsilon_{W} \times \int Ldt} \tag{6.2}$$

where N^{pass} is the number of $W \to e\nu$ and $Z/\gamma^* \to ee$ candidate events selected from data and N^{bkgd} is the estimated number of these that have come from background processes. A_W and A_{Z/γ^*} are the acceptances of geometric and kinematic cuts placed on the decay products of the W and Z respectively. The efficiencies with which events within acceptance pass the selection criteria is represented by ϵ_W and ϵ_{Z/γ^*}. $\int Ldt$ is the integrated luminosity of the data which is $10pb^{-1}$ for this study.

6.2 Acceptance Calculation

The combined geometric and kinematic acceptance has been estimated from Monte Carlo simulation*. The calculations for $Z/\gamma^* \to ee$ and $W \to e\nu$ events are explained in the next two sections.

6.2.1 Acceptance for $Z/\gamma^* \to ee$ Events

The acceptance calculation for $Z/\gamma^* \to ee$ events is performed using superclusters (SC) that are geometrically matched to Monte Carlo electrons emanating from the Z/γ^*. Acceptance (A_{Z/γ^*}) is defined as:

*For this calculation to be representative of reality a Monte Carlo that agrees with the data distributions of superclusters in the ECAL is needed. When data is available we will have the ability to tune the Monte Carlo to achieve this as closely as possible.

$$\frac{Events\ with\ both\ SC\ in\ fiducial\ with\ E_T > 20GeV\ and\ 70 < M_{SC,SC} < 110GeV}{All\ simulated\ Z/\gamma^* \rightarrow ee\ events} \tag{6.3}$$

where the ECAL fiducial region is $|\eta| < 1.4442$ and $1.56 < |\eta| < 2.5$ and $M_{SC,SC}$ is the disupercluster invariant mass[†]. The total acceptance is: 0.324 ± 0.002 calculated using $70,000$ simulated $Z/\gamma^* \rightarrow ee$ events.

6.2.2 Acceptance for W $\rightarrow$ eν Events

The acceptance calculation for $W \rightarrow e\nu$ events is performed using superclusters that are geometrically matched to Monte Carlo electrons emanating from the W. Acceptance (A_W) is defined as:

$$\frac{Events\ with\ one\ SC\ in\ fiducial\ with\ E_T > 20GeV}{All\ simulated\ W \rightarrow e\nu\ events} \tag{6.4}$$

where the ECAL fiducial region is $|\eta| < 1.4442$ and $1.56 < |\eta| < 2.5$. The total acceptance is: 0.7824 ± 0.0018 calculated using $40,000$ simulated $W \rightarrow e\nu$ events.

6.3 Uncertainties

Uncertainties on the cross-section measurements come from a variety of sources, the most important of which are listed:

1. **Signal yield:** the measurement of the signal yield is subject to both statistical and systematic uncertainties. The former are due to the finite sample size whilst the latter are introduced as a result of background subtraction.

[†]The invariant mass constraint is included in the acceptance because the $Z/\gamma^* \rightarrow ee$ selection includes this criterion. The range from $70-110GeV$ is considered large enough such that resolution effects are minimal.

2. **Efficiency measurements:** the statistical precision of the efficiencies depend on the amount of $Z \rightarrow ee$ data available. There are also systematic errors in the efficiency measurements, for example from the procedure used to subtract the background.

3. **Acceptance calculation:** this is measured from simulation and therefore the statistical errors can be made very small by running over a sufficiently large sample. Systematic uncertainties come from a variety of sources such as an imperfect modelling of the signal at the generator level and uncertainties in the direction and energy of reconstructed electrons.

4. **Integrated luminosity:** the error on the luminosity during early data taking is expected to be approximately 10% [60].

The total uncertainty on the cross-section measurement is a combination of all the uncertainties listed above added in quadrature. The uncertainty on the acceptance calculation has been investigated in detail [20]. Results show that the theoretical uncertainty on the $Z/\gamma^* \rightarrow ee$ acceptance calculation due to the limited precision of the parton distribution functions is a function of the pseudorapidity cut placed on the electron (Figure 6.5).

6.4 Event Selection: Z → ee

The selection used in the $Z/\gamma^* \rightarrow ee$ cross-section analysis is as follows:

- Event passes the single isolated electron HLT.
- Two electrons with superclusters in the ECAL fiducial region defined as: $|\eta| < 1.4442$ and $1.56 < |\eta| < 2.5$.
- Transverse energy of both electron superclusters greater than $20GeV$.
- Both electrons are isolated[‡].

[‡]where isolation is track isolation as defined in the last chapter.

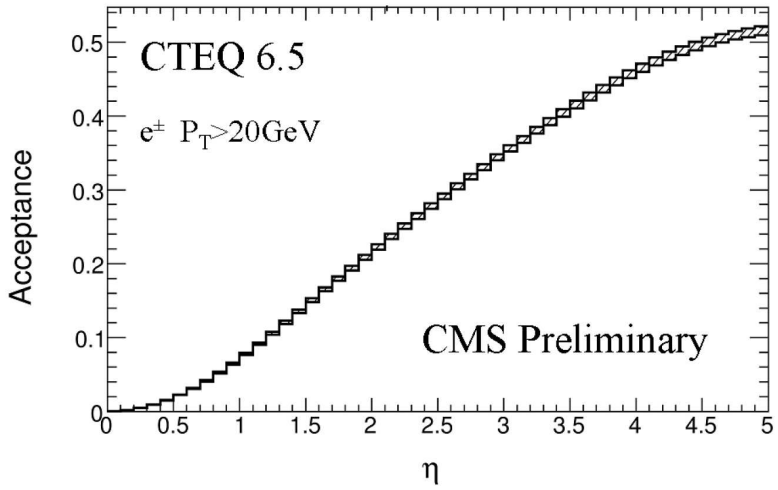

Figure 6.5: Acceptance for $Z/\gamma^* \rightarrow ee$ vs. electron pseudorapidity cut. The difference in the histograms shows the uncertainty due to parton distribution function.

- Both electrons pass 'Robust' electron identification.
- Invariant mass of the electron supercluster pair is between 70 and 110GeV.

6.4.1 Background to Z → ee

Electroweak Backgrounds

Electroweak backgrounds in the $Z/\gamma^* \rightarrow ee$ channel are expected to be small and can be estimated with adequate precision from simulation. Contributing channels include $Z/\gamma^* \rightarrow \tau\tau$, $t\bar{t}$ and $W+jets$. The first two can result in the production of two real electrons that have a softer transverse momentum distribution than the electrons produced directly from the decay of Z/γ^*. The possibility of misidentifying jets as electrons means that the $W + jets$ channel must be considered as a background. All these electroweak background channels were found to be negligible after the $Z/\gamma^* \rightarrow ee$ selection [20]. The dielecton invariant mass distributions for the signal and most significant backgrounds are shown in Figure 6.6.

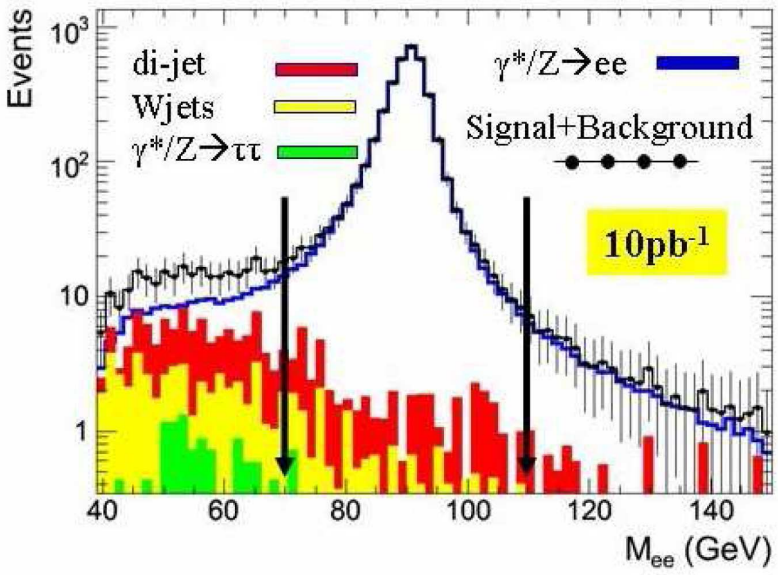

Figure 6.6: Dielectron invariant mass distribution for $Z/\gamma^* \rightarrow ee$ signal and the most dominant backgrounds.

Hadronic Backgrounds

Hadronic background channels include $b\bar{b}$ and $c\bar{c}$ which subsequently decay leptonically and dijets where jet fragments are misidentified as electrons. Although it is very unlikely that such an event will pass the dielectron selection they have a very large production cross-section. All hadronic background channels considered contribute negligibly to the signal after the $Z/\gamma^* \rightarrow ee$ selection as shown in Figure 6.6.

6.5 Event Selection: W → eν

The selection used in the $W \rightarrow e\nu$ cross-section analysis is as follows:

- Event passes the single isolated electron HLT.
- One electron with supercluster in the ECAL fiducial region defined as: $|\eta| < 1.4442$ and $1.56 < |\eta| < 2.5$.

- Transverse energy of the electron supercluster greater than $20GeV$.
- Electron is isolated.
- Electron passes 'Robust' electron identification.
- Missing transverse energy greater than $20GeV$[§].

Efforts are ongoing to improve the selection for the $W \rightarrow e\nu$ [61]. To achieve sufficient background rejection the single electron in the W decay needs to be more tightly selected than in the case of the Z decays especially as it is envisaged that missing transverse energy will have large uncertainties at start-up. This is being achieved by modifying the selection to include the following:

- Increasing the electron supercluster E_T threshold to $30GeV$.
- Tighter isolation that includes ECAL and HCAL as well as track isolation.
- Tighter electron identification (see Tables 6.1 and 6.2).
- Second electron veto to reduce the $Z/\gamma^* \rightarrow ee$ background.

	H/E	$\sigma_{\eta\eta}$	$\Delta\phi_{in}$	$\Delta\eta_{in}$
Barrel	0.115	0.0140	0.090	0.0090
Endcap	0.150	0.0275	0.092	0.0105

Table 6.1: Definition of electron identification criteria for the original $W \rightarrow e\nu$ selection and the $Z/\gamma^* \rightarrow ee$ selection.

	H/E	$\sigma_{\eta\eta}$	$\Delta\phi_{in}$	$\Delta\eta_{in}$
Barrel	0.0150	0.0092	0.020	0.0025
Endcap	0.0180	0.0250	0.020	0.0040

Table 6.2: Definition of electron identification criteria for the new $W \rightarrow e\nu$ selection.

Table 6.1 shows the electron identification criteria used in the $Z/\gamma^* \rightarrow ee$ and the original $W \rightarrow e\nu$ selection and Table 6.2 shows the criteria used in the new

[§]Missing transverse energy ($\not\!\!E_T$) is defined as the magnitude of the transverse vector sum over energy deposits in the calorimeter.

$W \to e\nu$ selection. In these tables H/E is the ratio of hadronic to electromagnetic energy, where H is the energy deposited in the HCAL in a cone of radius $\Delta R = 0.1$ centred on the electromagnetic supercluster and E is the energy of the supercluster. $\sigma_{\eta\eta}$ is the cluster shape covariance in the η direction; and $\Delta\eta_{in}$ and $\Delta\phi_{in}$ are the differences between the position of the supercluster and the position of the track at vertex extrapolated to the ECAL.

6.5.1 Background to W → eν

Backgrounds are more difficult to remove using $W \to e\nu$ selection as only one electron candidate is needed to pass the criteria. Contributions come from both electroweak and hadronic sources.

Electroweak Backgrounds

A significant background comes from $Z/\gamma^* \to ee$ where one electron escapes detection. Due to the good hermeticity of both the CMS ECAL and HCAL this happens in only approximately 3% of events. The electroweak bosons can also decay to taus which subsequently decay to electrons. Such electrons have a soft transverse momentum distribution so the kinematic cut on the supercluster E_T proves effective at minimising this background. Other channels considered are $W\gamma, WW, WZ, ZZ, tW$. The cross-sections of all these electroweak channels are well known and therefore their contributions can be precisely estimated from simulation.

Hadronic Backgrounds

Dijet events where one or more jet is misidentified as an electron contribute to the background in the $W \to e\nu$ channel. This contribution is dependent on the likelihood that a jet fakes an electron which cannot be precisely measured using simulation. The most important backgrounds are shown in the missing transverse energy plot in Figure 6.7¶.

¶The new selection cuts out much more of the background than the original selection shown in this figure.

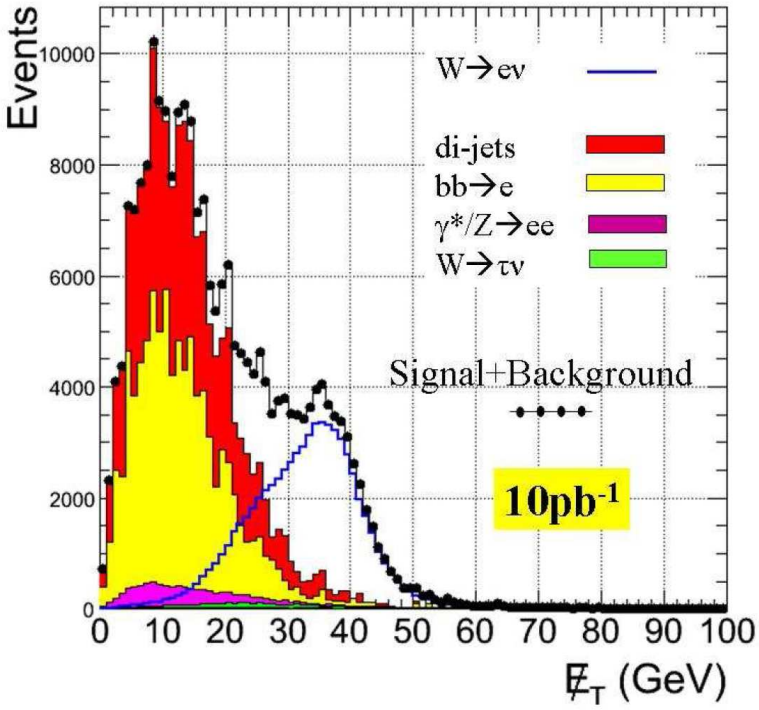

Figure 6.7: Missing transverse energy distribution for $W \rightarrow e\nu$ signal and the most dominant backgrounds.

Data driven methods of estimating and subtracting hadronic backgrounds have been developed [20]. An example is the 'matrix' method which involves inverting the track isolation on the electron in the $W \rightarrow e\nu$ selection. The missing transverse energy distribution for events that have an electron that passes isolation is very similar to the distribution for those where the electron is not isolated. Therefore, a template of the distribution can be found using data. It is assumed that the anti-isolated events come almost exclusively from the hadronic background. The background subtracted signal yield is calculated using this method [20].

6.6 Application of Efficiencies to Cross-section Measurement

Electron efficiencies calculated using the tag and probe method described in Chapter 5 have been used to compute event efficiencies for $Z/\gamma^* \rightarrow ee$ and $W \rightarrow e\nu$. In the case of the $Z/\gamma^* \rightarrow ee$ the samples used to calculate the efficiencies overlap

with the samples used to calculate the signal yield after selection. This leads to an overestimate of the uncertainty on the cross-section measurement described in detail in Ref. [20]. Therefore, for the measurement of the Z/γ^* cross-section with early data from the LHC it may be advantageous to split the sample in half so that the events used to calculate efficiencies using the tag and probe method are not the same as those the efficiencies are applied to. For the measurement of the W cross-section the full statistics $Z/\gamma^* \rightarrow ee$ sample should be used to calculate the efficiencies and then applied to the $W \rightarrow e\nu$ sample.

6.6.1 Z → ee Event Efficiency

The efficiency of a $Z/\gamma^* \rightarrow ee$ event to pass the selection can be calculated from the electron efficiencies by considering that both electrons are required to pass all offline cuts and that the event is required to pass the trigger:

$$\epsilon_{event} = \epsilon^2_{offline} \times \epsilon_{trigger} \tag{6.5}$$

where the efficiency that the event passes the trigger can be calculated using the online electron efficiency:

$$\epsilon_{trigger} = 1 - (1 - \epsilon_{online})^2 \tag{6.6}$$

and the offline efficiency has been factorised as discussed in Chapter 5:

$$\epsilon_{offline} = \epsilon_{preselection} \times \epsilon_{isolation} \times \epsilon_{identification} \tag{6.7}$$

Equation 6.6 is determined by considering that an event passes the trigger if either electron or both electrons pass online cuts. This can be calculated as unity minus the efficiency that neither electron passes.

As discussed previously, electron efficiencies vary as a function of η and E_T and therefore a matrix of efficiencies is provided for use in cross-section calculations (an

application of which is described in the next section). However, in the case of the $Z/\gamma^* \rightarrow ee$ measurement the efficiency is integrated over $E_T > 20GeV$ and the ECAL fiducial region. This is considered valid because the distribution of probes is similar to the distribution of the electrons from the Z decays[‖].

Table 6.3 shows a summary of the results for the $Z/\gamma^* \rightarrow ee$ cross-section measurement (Equation 6.1). The table shows that the calculated cross-section agrees with the generator level cross-section within errors. This confirms that the efficiencies computed using the tag and probe method do not introduce significant biases to the cross-section measurement. This is a good test that both the selection analysis and the efficiency calculation have been done in a consistent manner and the methods developed can confidently be used on early LHC data.

N^{pass}_{Z/γ^*}	3914 ± 63
N^{bkgd}_{Z/γ^*}	assumed 0.0
$\epsilon_{offline}$	$84.8 \pm 0.4\%$
$\epsilon_{trigger}$	$94.6 \pm 0.2\%$
ϵ_{event}	$68.1 \pm 0.6\%$
A_{Z/γ^*}	$32.39 \pm 0.18\%$
$\int Ldt$	$10pb^{-1}$
$\sigma_{Z/\gamma^*} \times BR\,(Z/\gamma^* \rightarrow ee)$	$1775 \pm 34pb$
$Input\ crosssection$	$1787pb$

Table 6.3: Results for the $Z/\gamma^* \rightarrow ee$ cross-section measurement. The errors are purely statistical.

6.6.2 W $\rightarrow$ eν Event Efficiency

The efficiency of a $W \rightarrow e\nu$ event to pass the selection can be calculated from the electron efficiencies by considering that the electron is required to pass all offline cuts and the event to pass the trigger:

$$\epsilon_{event} = \epsilon_{offline} \times \epsilon_{trigger} \tag{6.8}$$

[‖]Studies are ongoing to calculate the cross-section on an event by event basis that fully takes into account any small differences in the distributions although the effect on the cross-section is expected to be negligible as the probe distributions are similar to the electrons from Z/γ^*.

where the trigger in question is the single electron isolated trigger and therefore:

$$\epsilon_{trigger} = \epsilon_{online} \tag{6.9}$$

and the offline efficiency has been factorised as discussed in Chapter 5:

$$\epsilon_{offline} = \epsilon_{preselection} \times \epsilon_{isolation} \times \epsilon_{identification} \tag{6.10}$$

Electrons from the W decay have a different distribution in η and E_T to probes and therefore a matrix of efficiencies must be applied to the selected events taking into account the distribution of reconstructed electrons from the W. This is achieved using the following formula:

$$\sigma_W \times BR(W \to e\nu) = \frac{N_W^{pass} - N_W^{bkgd}}{A_W \times \sum_i f_i \epsilon_i \times \epsilon(\not{E}_T) \times \int Ldt} \tag{6.11}$$

where f_i is the proportion of events that have a reconstructed electron in bin i with respect to all events with electrons in the acceptance.

The $\epsilon(\not{E}_T)$ is the efficiency that signal events satisfy the missing transverse energy criterion. This value is obtained using the matrix method of background subtraction [20].

Table 6.4 shows a summary of the results for the $W \to e\nu$ cross-section measurement. The table shows that the calculated cross-section agrees with the generator level cross-section within errors. This provides a particularly strong check that the tag and probe method is both unbiased and of general use in physics analyses as the binned efficiencies have been successfully applied to a physics channel other than Z/γ^*. This is a more rigourous test than the $Z/\gamma^* \to ee$ measurement as the sample used to calculate the electron efficiencies is completely different to the $W \to e\nu$ sample to which the efficiencies are applied.

$N_W^{pass} - N_W^{bkgd}$	67954 ± 674
$\epsilon_{offline}$	$84.8 \pm 0.4\%$
$\epsilon_{trigger}$	$76.8 \pm 0.5\%$
ϵ_{event}	$65.1 \pm 0.5\%$
A_W	$52.3 \pm 0.2\%$
$\int Ldt$	$10pb^{-1}$
$\sigma_W \times BR(W \rightarrow e\nu)$	$19.97 \pm 0.25nb$
$Input\ crosssection$	$19.78nb$

Table 6.4: Results for the $W \rightarrow e\nu$ cross-section measurement. The errors are purely statistical.

6.7 Summary

The methods for early measurement of the inclusive W and Z/γ^* production cross-sections in the electron decay channel have been developed and successfully employed. Electron efficiencies calculated using data driven methods have been used in this analysis. The selection criteria are considered robust enough for use at start-up and efforts are ongoing to make the selection analysis and efficiency tools easily adaptable. Results of the analyses show that the efficiency measurements do not introduce significant biases on either the Z/γ^* or W cross-section measurements.

Chapter 7

Conclusions

The Large Hadron Collider (LHC) will be capable of producing massive particles that have not existed since the beginning of the Universe. Detectors at the LHC have been designed and built to reconstruct and select the decay products of these particles with high precision. Electrons in particular can be very precisely reconstructed in CMS providing that the detector is well understood and that their efficiencies can be calculated from data.

The research conducted in this thesis has led to an increased understanding of the properties of CMS ECAL crystals and provided a check that new crystals were meeting with strict quality criteria imposed by the CMS Collaboration. Studies with simulated and test beam data have increased confidence that the hardware and software involved in reconstructing electrons are performing well. Data driven methods to determine the efficiency of electron reconstruction and selection in CMS have been developed, tested and employed on a 'data-like' simulated sample. Finally, these efficiencies have been applied in the measurement of the inclusive W and Z/γ^* cross-sections in the electron decay channels.

The main results from each chapter are given in the following sections.

7.1 Irradiation Studies on CMS ECAL Crystals

All SIC crystals tested at a dose rate of $7.4Gy/hr$ proved to be sufficiently radiation hard to withstand the harsh CMS endcap ($\eta = 2.7$) environment at high luminosity without unacceptable loss of light yield. Seven of the ten crystals tested at the higher dose rate of $16.5Gy/hr$ had acceptable values of maximum μ. The spread in R values is a little larger than hoped but considered acceptable. At the time of the measurements the information from these studies helped to guide the production of crystals from SIC.

The results of the calibration with ENEA are reliable and values of maximum μ can be compared without unacceptable uncertainties being introduced and the consistency between the measurements increased the confidence that information conveyed to SIC concerning the standard of their crystals was accurate.

Measurements of FNUF have shown that radiation damage has the effect of increasing crystal uniformity which is favourable in terms of decreasing the ECAL energy resolution. It has also been discovered that the more radiation hard a crystal is, the less acceptable the FNUF immediately post irradiation.

7.2 ECAL Reconstruction and Electron Selection in CMS

The dependence of energy containment on pseudorapidity across an entire ECAL supermodule has been studied during the 2006 test beam. An observed trend is caused by a purely geometrical effect. Crystals are gradually tilted toward higher pseudorapidity resulting in leakage of some of the shower through the exposed edge of the crystal into empty space in front of the adjacent crystal where the energy can not be recovered.

The depth of an electromagnetic shower is an input parameter in the electron reconstruction algorithm. When this parameter is set to the correct value the position

resolution of the ECAL is the same in both positive and negative halves of the detector. The position resolution of the ECAL can be reliably calculated once this parameter is correctly implemented. Results agree with previous studies done with old CMS software [3] and this part of the electron reconstruction chain is considered validated.

7.3 Measuring Electron Efficiencies at CMS using Early Data

The electron efficiencies produced using the tag and probe method have been validated against the Monte Carlo truth efficiencies. Also, a suitable method for subtracting the background has been developed and successfully employed. It is found that most steps in the reconstruction chain have associated efficiencies that vary as a function of η and E_T and therefore it is necessary to bin the efficiencies in these two variables in order to make them useful for analyses where the electron distributions are different from the probe distributions.

7.4 Z/γ^* and W Boson Cross-section Measurements

The methods for early measurement of the inclusive W and Z/γ^* production cross-sections in the electron decay channel have been developed and successfully employed. Electron efficiencies calculated using data driven methods have been used in this analysis. The selection criteria are considered robust enough for use at start-up and efforts are ongoing to make the selection analysis and efficiency tools easily adaptable. Results of the analyses show that the efficiency measurements do not introduce significant biases on either the Z/γ^* or W cross-section measurements.

References

[1] "Large Hadron Collider homepage." `http://lhc.web.cern.ch/lhc/`.

[2] "CERN homepage." `http://www.cern.ch/`.

[3] "The Physics Technical Design Report, volume 2," tech. rep., CMS Collaboration, 2006. CERN/LHCC 2006-021.

[4] "LEP webpage." `http://greybook.cern.ch/`.

[5] Y. Schutz, "Heavy-ion physics at LHC," *J. Phys. G: Nucl. Part. Phys.*, vol. 30, pp. S903–S909, 2004.

[6] "The CMS experiment at the CERN LHC," *Submitted to JINST*, Jan. 2008.

[7] "ATLAS collaboration homepage." `http://atlas.web.cern.ch/Atlas/index.html`.

[8] "LHCb collaboration homepage." `http://lhcb.web.cern.ch/lhcb/`.

[9] "ALICE collaboration homepage." `http://aliceinfo.cern.ch/`.

[10] D. H. Perkins, *Introduction to High Energy Physics 4th edition*. Cambridge University Press, 2000.

[11] F. Halzen and A. D. Martin, *Quarks and Leptons: An Introductory Course in Modern Particle Physics*. John Wiley and Sons, 1984.

[12] P. Higgs, "Broken symmetries and the masses of gauge bosons," *Phys. Rev. Lett.*, vol. 13, Oct. 1964.

[13] M. Goldhaber *et al.*, "Helicity of neutrinos," *Phys. Rev.*, vol. 1109, p. 1015, Dec. 1957.

[14] E. Noether, "Invariant variation problems (1918)," Mar. 2005. arXiv:physics/0503066v1.

[15] G. Arnison *et al.*, "Experimental observation of isolated large transverse energy electrons with associated missing energy at x/s = 540 GeV," *Physics Letters*, vol. 122B, Feb. 1983.

[16] M. Banner *et al.*, "Observation of single isolated electrons of high transverse momentum in events with missing transverse energy at the CERN $\bar{p}p$ collider," *Physics Letters*, vol. 122B, Mar. 1983.

[17] G. Arnison *et al.*, "Experimental observation of lepton pairs of invariant mass around 95 $\frac{GeV}{c^2}$ at the CERN SPS collider," *Physics Letters*, vol. 126B, July 1983.

[18] M. Banner *et al.*, "Evidence for $Z^0 \rightarrow e^+e^-$ at the CERN $p\bar{p}$ collider," *Physics Letters*, vol. 129, Sept. 1983.

[19] "Measurement of W and Z boson production cross sections," *Phys. Rev. D.*, vol. 60, Jan. 1999. arXiv:hep-ex/9901040v1.

[20] G. Daskalakis *et al.*, "Towards a measurement of the inclusive $W \rightarrow e\nu$ and $Z \rightarrow ee$ cross section in pp collisions at $\sqrt{s} = 14TeV$," *CMS AN*, no. 026, 2007.

[21] W. M. Yao *et al.*, "Higgs bosons: Theory and searches." `http://pdg.lbl.gov/2007/reviews/higgs_s055.pdf`.

[22] R. Barate *et al.*, "Search for the Standard Model Higgs boson at LEP," *Phys. Rev. Lett.*, vol. B565, pp. 61–75, 2003.

[23] M. Pieri *et al.*, "Inclusive search for the Higgs boson in the $H \rightarrow \gamma\gamma$ channel.," *CMS AN*, no. 112, 2006.

[24] Y. Fukuda *et al.*, "Evidence for oscillation of atmospheric neutrinos," *Phys. Rev. Lett.*, vol. 81, pp. 1562–1567, 1998.

[25] J. Christenson, J. W. Cronin, V. L. Fitch, and R. Turlay, "Evidence for the 2π decay of the K_2^0 meson," *Phys. Rev. Lett.*, vol. 13, pp. 138–140, July 1964.

[26] ALEPH, DELPHI, L3, and OPAL, "Electroweak parameters of the Z^0 resonance and the Standard Model," *Physics Letters B*, vol. 276, pp. 247–253, Dec. 1992.

[27] "LHC Technical Report." `http://ab-div.web.cern.ch/ab-div/Publications/LHC-DesignReport.html`.

[28] "Tevatron rookie book." `http://www-bdnew.fnal.gov/operations/rookie_books/Tevatron_v1.pdf`.

[29] "The Tracker Project Technical Design Report," tech. rep., CMS Collaboration, 1998. CERN/LHCC 98-006.

[30] "The Hadron Calorimeter Project Technical Design Report," tech. rep., CMS Collaboration, 1997. CERN/LHCC 97-31.

[31] "The Magnet Project Technical Design Report," tech. rep., CMS Collaboration, 1997. CERN/LHCC 97-10.

[32] "The Muon Technical Design Report," tech. rep., CMS Collaboration, 1997. CERN/LHCC 97-32.

[33] "The TriDAS Project Technical Design Report, volume 1: The Trigger Systems," tech. rep., CMS Collaboration, 2000. CERN/LHCC 2000 - 38.

[34] "The TriDAS Project Technical Design Report, volume 2: Data Acquisition and High-Level Trigger," tech. rep., CMS Collaboration, 2002. CERN/LHCC 02-26.

[35] "The Electromagnetic Technical Design Report," tech. rep., CMS Collaboration, 1997. CERN/LHCC.

[36] A. A. Annenkov *et al.*, "Lead tungstate scintillation material," *Nucl. Inst. Meth.*, vol. A490, pp. 30–50, 2002.

[37] P. Lecoq *et al.*, "Systematic study of the short-term instability of $PbWO_4$ scintillator parameters under irradiation," *CMS Note*, no. 055, 1997.

[38] P. Lecoq *et al.*, "Lead tungstate ($PbWO_4$) scintillators for LHC EM calorimetry," *Nucl. Inst. Meth.*, vol. A365, pp. 291–298, 1995.

[39] S. Baccaro, "Radiation damage mechanism in $PbWO_4$ crystal and radiation hardness quality control of PWO scintillators for CMS," *CMS Note*, no. 038, 1997.

[40] P. Lecoq *et al.*, "Radiation damage kinetics in PWO crystals," *CMS Note*, no. 008, 1997.

[41] G. Davies, J. P. Peigneux, A. Singovski, and C. Seez, "A study of the monitoring of radiation damage to CMS ECAL crystals, performed at X5-GIF," *CMS Note*, no. 0020, 2000.

[42] D. J. Graham and C. Seez, "Simulation of longitudinal light collection uniformity in $PbWO_4$ crystals," *CMS Note*, no. 002, 1996.

[43] M. Ryan *et al.*, "Light collection uniformity of lead tungstate crystals for the CMS electromagnetic calorimeter," *Nucl. Inst. Meth.*, vol. A540, pp. 273–284, 2005.

[44] S. Baccaro *et al.*, "Gamma irradiation facility at ENEA - casaccia centre (Rome)," *Internal Note*, 2000.

[45] S. Baccaro *et al.*, "Lumen: a highly versatile spectrophotometer for measuring the transmittance throughout very long samples as well as microstructures," *Internal Note*, 2000.

[46] R. Zhu, "New results from Caltech." Presentation at detector performance meeting at CERN ECAL week 15/03/05.

[47] M. J. Ryan, *Light Collection Uniformity of Lead Tungstate Crystals for the CMS Electromagnetic Calorimeter Endcaps.* PhD thesis, Imperial College London, 2003.

[48] P. Barrillon, "Offline results." Presentation at ECAL test beam analysis meeting 28/07/04.

[49] E. M. McLeod, *An Investigation of Lead Tungstate Crystals for the Compact Muon Solenoid Detector at the LHC.* PhD thesis, Imperial College London, 2003.

[50] A. Cecilia, "Chinese $PbWO_4$ crystals for the electromagnetic calorimeter of CMS experiment." Presentation at ENEA.

[51] "CMS software workbook." `https://twiki.cern.ch/twiki/bin/view/CMS/WorkBookCMSSWFramework`.

[52] S. Baffioni *et al.*, "Electron reconstruction in CMS," *CMS Note*, no. 040, 2006.

[53] A. Zabi *et al.*, "Pseudorapidity dependence of the energy containment at the 2006 ECAL testbeam," *CMS DN*, no. 005, 2007.

[54] S. D. Drell and T. M. Yan, "Massive lepton-pair production in hadron-hadron collisions at high energies," *Phys. Rev. Lett.*, vol. 25, pp. 316–320, May 1970.

[55] A. D. Martin *et al.*, "Parton distributions and the LHC: W and Z production," *Eur.Phys.J.*, vol. C14, pp. 133–145, July 1999.

[56] N. Raicevic, for the H1, and ZEUS collaborations, "Structure functions and extraction of PDFs at HERA," 2006. arXiv:hep-ex/0605050v2.

[57] A. D. Martin *et al.*, "Uncertainties on w and z production at the lhc," *hep-ex/0509002v1*, Sept. 2005.

[58] C. Anastasiou *et al.*, "High-precision QCD at hadron colliders: electroweak gauge boson rapidity distribution at NNLO," *hep-ph/0312266*, May 2004.

[59] C. Amsler *et al.*, "The Review of Particle Physics," *Physics Letters B*, vol. 667, no. 1, 2008.

[60] "Measurement of the relative luminosity at the LHC." `http://uslarp.lbl.gov/workshops/050411/references/1.pdf`.

[61] G. Daskalakis *et al.*, "Towards a measurement of the inclusive $W \to e\nu$ and $Z \to ee$ cross section in pp collisions at $\sqrt{s} = 14TeV$," *CMS PAS*, July 2008.

Appendices

Appendix A: ECAL dose rates at high luminosity

η	Dose Rate at Shower Maximum (Gy/hr)	Dose Rate Behind Crystal (Gy/hr)
0.0(barrel)	0.18	0.02
1.48(barrel)	0.28	0.03
1.48(endcap)	0.29	0.04
2.6(endcap)	6.5	1.4
3.0(endcap)	15.0	3.0

Table 1: ECAL dose rates at high luminosity ($10^{34} cm^{-2} s^{-1}$).

Appendix B: Details of SIC crystals tested in 2005

Crystal No	Batch No	Dates Measured	No of Irradiations	Dose Rate (Gy/hr)
2552	BTCP	04/02/05 - 23/02/05	1	7.4
2682	1	04/02/05 - 23/02/05	1	7.4
2683	1	04/02/05 - 23/02/05	1	7.4
2684	1	04/02/05 - 23/02/05	1	7.4
2706	1	04/02/05 - 23/02/05	1	7.4
2717	2	12/01/05 - 20/01/05	1	7.5
2735	2	12/01/05 - 20/01/05	1	7.5
2745	2	12/01/05 - 20/01/05	1	7.5
2753	2	12/01/05 - 20/01/05	1	7.5
2767	3	08/07/05 - 10/08/05	2	7.0
2769	3	25/02/05 - 08/03/05	1	7.35
2771	3	04/04/05 - 03/05/05	1	7.2
2774	3	25/02/05 - 08/03/05	1	7.35
2808	3	04/04/05 - 03/05/05	1	7.2
2810	4	25/02/05 - 08/03/05	1	7.35
2813	4	04/04/05 - 03/05/05	1	7.2
2820	4	08/07/05 - 10/08/05	2	7.0
2821	4	25/02/05 - 08/03/05	1	7.35
2822	4	08/07/05 - 10/08/05	2	7.0
2825	4	04/04/05 - 03/05/05	1	7.2
2826	4	08/07/05 - 10/08/05	2	7.0
2837	4	04/04/05 - 03/05/05	1	7.2
2847	4	08/07/05 - 10/08/05	2	7.0
2858	4	25/02/05 - 08/03/05	1	7.35
2859	5	27/04/05 - 20/05/05	3	7.15
2869	5	27/04/05 - 20/05/05	3	7.15
2875	5	27/04/05 - 20/05/05	3	7.15
2882	5	27/04/05 - 20/05/05	3	7.15
2889	5	25/08/05 - 06/09/05	1	6.9
2899	5	25/08/05 - 06/09/05	1	6.9
2908	5	27/04/05 - 20/05/05	3	7.15
2912	6	25/08/05 - 06/09/05	1	6.9
2935	6	25/08/05 - 06/09/05	1	6.9
2939	6	25/08/05 - 06/09/05	1	6.9
2941	6	02/06/05 - 15/07/05	2	7.05
2944	6	02/06/05 - 15/07/05	2	7.05

Table 2: Details of 35 SIC crystals tested in 2005.

Crystal No	Batch No	Dates Measured	FNUF	Dose Rate (Gy/hr)	Irradiation Time (hr)
2761	3	08/12/05 - 21/12/05	yes	16.5(16.6)	24.75(24)
2796	3	24/11/05 - 12/12/05	no	16.5(16.3)	23.58
2801	3	24/11/05 - 12/12/05	no	16.5(16.3)	23.58
2807	3	08/12/05 - 21/12/05	yes	16.5(16.6)	24.75(24)
2871	5	08/12/05 - 21/12/05	yes	16.5(16.6)	24.75(24)
2873	5	24/11/05 - 12/12/05 08/12/05 - 21/12/05	no no	16.5(16.3) 6.67	23.58 24
2880	5	24/11/05 - 12/12/05	no	16.5(16.3)	23.58
2920	6	08/12/05 - 21/12/05	yes	16.5(16.6)	24.75(24)
2934	6	24/11/05 - 12/12/05	no	16.5(16.3)	23.58
2951	6	08/12/05 - 21/12/05	yes	16.5(16.6)	24.75(24)

Table 3: Details of crystals tested for calibration study, ENEA values given in brackets.

Appendix C: Results of SIC crystals tested in 2005

Crystal No	R	LY Decrease (%)	Maximum μ (m-1)
2682	0.96±0.05	30±1	0.83±0.02
2683	1.02±0.05	32±1	0.82±0.02
2684	1.13±0.05	35±1	0.83±0.02
2706	0.92±0.03	39±1	1.14±0.03
2717	0.95±0.03	40±1	1.15±0.06
2735	0.90±0.04	34±1	1.05±0.06
2745	0.96±0.04	35±1	0.97±0.06
2753	0.96±0.03	38±1	1.15±0.06
2767	0.94±0.10	12±1	0.38±0.05
2769	0.85±0.11	16±1	0.34±0.03
2771	0.87±0.11	14±1	0.33±0.05
2774	0.72±0.12	12±1	0.28±0.03
2808	0.92±0.04	31±1	0.92±0.05
2810	0.96±0.04	37±1	0.97±0.03
2813	1.10±0.07	28±1	0.67±0.05
2820	1.07±0.12	17±1	0.33±0.05
2821	0.92±0.07	22±1	0.59±0.03
2822	0.83±0.06	21±1	0.57±0.06
2825	1.02±0.05	31±1	0.83±0.05
2826	0.90±0.06	24±1	0.64±0.05
2837	0.93±0.10	14±1	0.38±0.05
2847	0.92±0.05	27±1	0.75±0.06
2858	0.92±0.04	32±1	0.89±0.03
2859	1.01±0.04	36±1	1.00±0.06
2869	1.11±0.07	26±1	0.64±0.05
2875	1.06±0.05	32±1	0.86±0.05
2882	1.21±0.07	27±1	0.67±0.06
2889	1.00±0.06	28±1	0.61±0.05
2899	0.97±0.06	25±1	0.65±0.05
2908	1.08±0.06	28±1	0.71±0.06
2912	1.11±0.08	25±1	0.54±0.06
2935	0.71±0.04	23±1	0.92±0.05
2939	1.08±0.11	21±1	0.39±0.05
2941	0.95±0.04	34±1	1.04±0.06
2944	0.90±0.04	31±1	0.91±0.06

Table 4: R, μ and light yield decrease for SIC crystals irradiated at approximately $7Gy/hr$ for 24 hours.

Crystal No	R	LY Decrease (%)	Maximum μ (m-1)
2761	1.03±0.06	28±1	0.73(0.60)±0.06(0.01)
2796	1.23±0.19	13±1	0.24(0.50)±0.06(0.01)
2801	0.83±0.03	38±1	1.23(1.24)±0.07(0.01)
2807	0.95±0.04	36±1	1.07(0.89)±0.06(0.01)
2871	0.94±0.04	36±1	1.08(0.95)±0.06(0.01)
2873	0.84±0.02	46±1	1.60(1.27)±0.07(0.01)
2880	0.88±0.02	47±1	1.57(1.23)±0.07(0.01)
2920	0.77±0.03	33±1	1.22(0.87)±0.06(0.01)
2934	0.80±0.02	45±1	1.74(1.38)±0.07(0.01)
2951	0.82±0.03	39±1	1.28(1.15)±0.07(0.01)

Table 5: R, μ and light yield decrease for SIC crystals irradiated at approximately $16.5 Gy/hr$ for 24 hours, ENEA values given in brackets.

Appendix D: Cross-check of factorization equivalence

Figures 1 and 2 show the total offline efficiency vs. probe E_T for probes to pass all the offline cuts detailed in Chapter 5 and the online efficiency considering the probes to have passed the offline cuts. Figures 3 and 4 show the online efficiency vs. probe E_T and the offline efficiency for probes that passed the trigger. The total efficiency for online and offline cuts is:

$$\epsilon_{tot} = \epsilon_{offline} \times \epsilon_{online} = 0.848 \times 0.768 = 0.65 \quad (1)$$

$$\epsilon_{tot} = \epsilon_{online} \times \epsilon_{offline} = 0.674 \times 0.967 = 0.65 \quad (2)$$

The total efficiency is independent of the order of the constituent steps, therefore, the correlations between efficiency steps have been correctly accounted for.

Figure 3 shows a noticeable decrease in the trigger efficiency at high E_T. This is due to the cuts in the HLT algorithm being optimised for lower E_T electrons $(30 - 50GeV)$. Constraints on E_{SC}/P_{track} and E_{HCAL}/E_{ECAL} both contribute to this inefficiency. The HLT algorithms are in a state of flux and will be optimised to correct this high E_T behaviour.

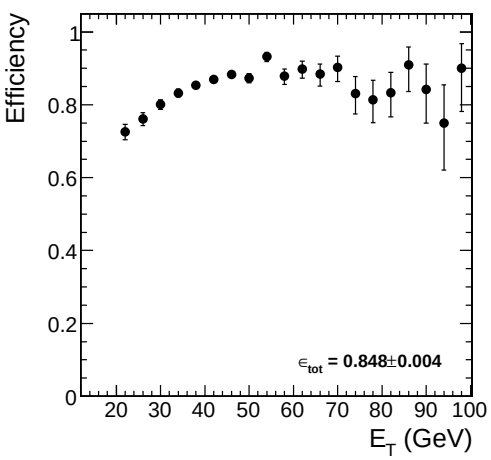

Figure 1: Total offline efficiency.

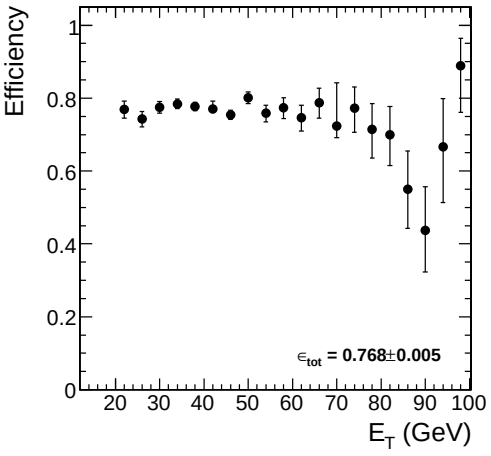

Figure 2: Online efficiency for probes passing all offline cuts.

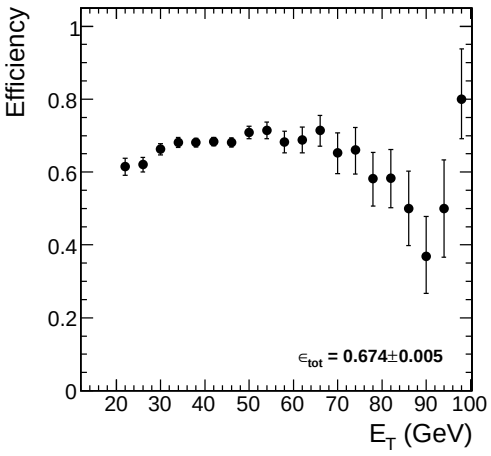

Figure 3: Online efficiency.

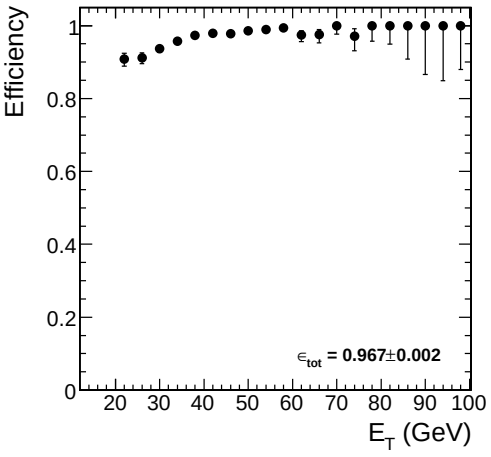

Figure 4: Offline efficiency for probes passing HLT.

Appendix E: Efficiency tables vs. η and E_T

Table 6: Efficiency results: preselection (background subtracted).

$E_T(GeV)$ / η	$20-30$	$30-40$	$40-50$	$50-60$	$60-70$	$70-80$
$0-0.3$	$1.1^{+1.6}_{-1.6}$	$0.91^{+0.048}_{-0.048}$	$0.98^{+0.0082}_{-0.0082}$	$0.99^{+0.022}_{-0.022}$	$1^{+0.16}_{-0.16}$	$0.72^{+0.097}_{-0.097}$
$0.3-0.6$	$0.95^{+0.14}_{-0.14}$	$0.96^{+0.026}_{-0.026}$	$0.93^{+0.015}_{-0.015}$	$0.95^{+0.027}_{-0.027}$	$0.94^{+0.05}_{-0.05}$	$0.96^{+0.14}_{-0.14}$
$0.6-0.9$	$1.1^{+0.22}_{-0.22}$	$0.98^{+0.025}_{-0.025}$	$0.94^{+0.019}_{-0.019}$	$0.95^{+0.025}_{-0.025}$	$0.71^{+0.073}_{-0.073}$	$1.1^{+0.07}_{-0.07}$
$0.9-1.2$	$0.84^{+0.059}_{-0.059}$	$0.96^{+0.018}_{-0.018}$	$0.96^{+0.013}_{-0.013}$	$0.9^{+0.034}_{-0.034}$	$0.89^{+0.066}_{-0.066}$	$0.81^{+0.13}_{-0.13}$
$1.2-1.5$	$0.69^{+0.042}_{-0.042}$	$0.86^{+0.023}_{-0.023}$	$0.94^{+0.025}_{-0.025}$	$0.74^{+0.055}_{-0.055}$	$0.91^{+0.12}_{-0.12}$	$1.1^{+0.089}_{-0.089}$
$1.5-1.8$	$0.98^{+0.02}_{-0.02}$	$0.84^{+0.026}_{-0.026}$	$0.9^{+0.023}_{-0.023}$	$0.87^{+0.047}_{-0.047}$	$1.3^{+0.34}_{-0.34}$	$1^{+0.1}_{-0.1}$
$1.8-2.1$	$1.2^{+0.052}_{-0.052}$	$0.89^{+0.026}_{-0.026}$	$0.96^{+0.015}_{-0.015}$	$0.94^{+0.034}_{-0.034}$	$0.77^{+0.13}_{-0.13}$	$0.96^{+0.083}_{-0.083}$
$2.1-2.4$	$0.82^{+0.053}_{-0.053}$	$0.83^{+0.05}_{-0.05}$	$0.82^{+0.04}_{-0.04}$	$0.84^{+0.092}_{-0.092}$	$0.86^{+0.5}_{-0.5}$	$1.1^{+0.25}_{-0.25}$
$2.4-2.7$	$0.48^{+0.081}_{-0.081}$	$0.66^{+0.097}_{-0.097}$	$0.73^{+0.072}_{-0.072}$	$0.62^{+0.16}_{-0.16}$	$0.27^{+0.23}_{-0.23}$	$0.5^{+0.41}_{-0.41}$

Table 7: Efficiency results: isolation (background not subtracted as considered negligible).

$E_T(GeV)$ / η	$20-30$	$30-40$	$40-50$	$50-60$	$60-70$	$70-80$	$80-90$	$90-100$
$0-0.3$	$0.9^{+0.03}_{-0.037}$	$0.96^{+0.01}_{-0.012}$	$0.96^{+0.0089}_{-0.011}$	$0.99^{+0.0074}_{-0.015}$	$1^{+0}_{-0.028}$	$1^{+0}_{-0.065}$	$1^{+0}_{-0.21}$	$1^{+0}_{-0.44}$
$0.3-0.6$	$0.9^{+0.028}_{-0.033}$	$0.96^{+0.011}_{-0.014}$	$0.97^{+0.0084}_{-0.01}$	$0.99^{+0.008}_{-0.016}$	$1^{+0}_{-0.03}$	$1^{+0}_{-0.074}$	$1^{+0}_{-0.15}$	$1^{+0}_{-0.32}$
$0.6-0.9$	$0.89^{+0.031}_{-0.037}$	$0.95^{+0.013}_{-0.015}$	$0.98^{+0.0065}_{-0.0085}$	$1^{+0}_{-0.014}$	$1^{+0}_{-0.036}$	$1^{+0}_{-0.074}$	$1^{+0}_{-0.15}$	$1^{+0}_{-0.32}$
$0.9-1.2$	$0.87^{+0.031}_{-0.035}$	$0.95^{+0.011}_{-0.014}$	$0.98^{+0.0071}_{-0.0095}$	$0.99^{+0.0098}_{-0.02}$	$1^{+0}_{-0.043}$	$0.89^{+0.075}_{-0.13}$	$1^{+0}_{-0.13}$	$1^{+0}_{-0.32}$
$1.2-1.5$	$0.89^{+0.032}_{-0.039}$	$0.93^{+0.016}_{-0.019}$	$0.98^{+0.0086}_{-0.012}$	$1^{+0}_{-0.022}$	$1^{+0}_{-0.059}$	$1^{+0}_{-0.12}$	$1^{+0}_{-0.25}$	$1^{+0}_{-0.32}$
$1.5-1.8$	$0.88^{+0.031}_{-0.036}$	$0.94^{+0.016}_{-0.02}$	$0.98^{+0.0094}_{-0.014}$	$1^{+0}_{-0.025}$	$1^{+0}_{-0.062}$	$1^{+0}_{-0.15}$	$1^{+0}_{-0.21}$	0^{+1}_{-0}
$1.8-2.1$	$0.81^{+0.037}_{-0.041}$	$0.91^{+0.019}_{-0.022}$	$0.9^{+0.021}_{-0.024}$	$0.85^{+0.045}_{-0.054}$	$1^{+0}_{-0.11}$	$0.67^{+0.15}_{-0.18}$	$1^{+0}_{-0.21}$	0^{+1}_{-0}
$2.1-2.4$	$0.8^{+0.033}_{-0.036}$	$0.81^{+0.029}_{-0.032}$	$0.8^{+0.034}_{-0.037}$	$0.84^{+0.063}_{-0.08}$	$0.92^{+0.058}_{-0.1}$	$1^{+0}_{-0.17}$	$0.67^{+0.19}_{-0.24}$	$1^{+0}_{-0.32}$
$2.4-2.7$	$0.87^{+0.089}_{-0.061}$	$0.88^{+0.056}_{-0.076}$	$0.97^{+0.025}_{-0.048}$	$1^{+0}_{-0.15}$	$1^{+0}_{-0.44}$	$1^{+0}_{-0.44}$	0^{+1}_{-0}	0^{+1}_{-0}

Table 8: Efficiency results: 'Robust' electron identification (background not subtracted as considered negligible).

$E_T(GeV)$ / η	$20-30$	$30-40$	$40-50$	$50-60$	$60-70$	$70-80$	$80-90$	$90-100$
$0-0.3$	$1^{+0}_{-0.016}$	$1^{+0}_{-0.0043}$	$1^{+0.0019}_{-0.0039}$	$1^{+0}_{-0.012}$	$1^{+0}_{-0.028}$	$1^{+0}_{-0.065}$	$1^{+0}_{-0.21}$	$1^{+0}_{-0.44}$
$0.3-0.6$	$0.99^{+0.0082}_{-0.016}$	$0.99^{+0.0045}_{-0.0073}$	$0.99^{+0.0035}_{-0.0056}$	$1^{+0}_{-0.013}$	$1^{+0}_{-0.03}$	$1^{+0}_{-0.074}$	$1^{+0}_{-0.15}$	$1^{+0}_{-0.32}$
$0.6-0.9$	$1^{+0}_{-0.015}$	$1^{+0.0032}_{-0.0066}$	$1^{+0}_{-0.0035}$	$1^{+0}_{-0.014}$	$1^{+0}_{-0.036}$	$1^{+0}_{-0.074}$	$1^{+0}_{-0.15}$	$1^{+0}_{-0.32}$
$0.9-1.2$	$1^{+0}_{-0.012}$	$1^{+0}_{-0.0042}$	$1^{+0}_{-0.0043}$	$0.99^{+0.0099}_{-0.02}$	$1^{+0}_{-0.043}$	$1^{+0}_{-0.12}$	$1^{+0}_{-0.13}$	$1^{+0}_{-0.32}$
$1.2-1.5$	$1^{+0}_{-0.016}$	$1^{+0}_{-0.0059}$	$0.99^{+0.0038}_{-0.0076}$	$1^{+0}_{-0.022}$	$1^{+0}_{-0.059}$	$1^{+0}_{-0.12}$	$1^{+0}_{-0.25}$	$1^{+0}_{-0.32}$
$1.5-1.8$	$1^{+0}_{-0.013}$	$1^{+0}_{-0.0068}$	$0.99^{+0.0075}_{-0.012}$	$1^{+0}_{-0.025}$	$1^{+0}_{-0.062}$	$1^{+0}_{-0.15}$	$1^{+0}_{-0.21}$	0^{+1}_{-0}
$1.8-2.1$	$1^{+0}_{-0.014}$	$1^{+0}_{-0.0063}$	$1^{+0}_{-0.0075}$	$1^{+0}_{-0.025}$	$1^{+0}_{-0.11}$	$1^{+0}_{-0.21}$	$1^{+0}_{-0.21}$	0^{+1}_{-0}
$2.1-2.4$	$1^{+0}_{-0.011}$	$1^{+0}_{-0.0087}$	$1^{+0}_{-0.012}$	$1^{+0}_{-0.051}$	$1^{+0}_{-0.091}$	$1^{+0}_{-0.17}$	$1^{+0}_{-0.32}$	$1^{+0}_{-0.32}$
$2.4-2.7$	$1^{+0}_{-0.053}$	$1^{+0}_{-0.051}$	$1^{+0}_{-0.039}$	$1^{+0}_{-0.15}$	$1^{+0}_{-0.44}$	$1^{+0}_{-0.44}$	0^{+1}_{-0}	0^{+1}_{-0}

Table 9: Efficiency results: online (background not subtracted as considered negligible).

$E_T(GeV)$ / η	$20-30$	$30-40$	$40-50$	$50-60$	$60-70$	$70-80$	$80-90$	$90-100$
$0-0.3$	$0.85^{+0.048}_{-0.038}$	$0.85^{+0.021}_{-0.023}$	$0.84^{+0.018}_{-0.02}$	$0.77^{+0.049}_{-0.037}$	$0.9^{+0.041}_{-0.054}$	$0.94^{+0.044}_{-0.081}$	$0.75^{+0.15}_{-0.21}$	0^{+1}_{-0}
$0.3-0.6$	$0.88^{+0.032}_{-0.038}$	$0.8^{+0.024}_{-0.026}$	$0.82^{+0.021}_{-0.022}$	$0.77^{+0.042}_{-0.046}$	$0.84^{+0.054}_{-0.066}$	$0.64^{+0.11}_{-0.13}$	$0.83^{+0.11}_{-0.17}$	$1^{+0}_{-0.32}$
$0.6-0.9$	$0.83^{+0.04}_{-0.045}$	$0.85^{+0.023}_{-0.025}$	$0.83^{+0.02}_{-0.022}$	$0.88^{+0.034}_{-0.04}$	$0.73^{+0.074}_{-0.083}$	$0.86^{+0.074}_{-0.11}$	$0.83^{+0.11}_{-0.17}$	$1^{+0}_{-0.32}$
$0.9-1.2$	$0.68^{+0.047}_{-0.05}$	$0.7^{+0.027}_{-0.028}$	$0.78^{+0.025}_{-0.026}$	$0.82^{+0.042}_{-0.048}$	$0.68^{+0.086}_{-0.095}$	$0.75^{+0.12}_{-0.16}$	$0.57^{+0.16}_{-0.17}$	$0.5^{+0.25}_{-0.25}$
$1.2-1.5$	$0.67^{+0.054}_{-0.057}$	$0.59^{+0.035}_{-0.036}$	$0.58^{+0.035}_{-0.036}$	$0.6^{+0.067}_{-0.069}$	$0.5^{+0.11}_{-0.11}$	$0.5^{+0.16}_{-0.16}$	$1^{+0}_{-0.25}$	$0.5^{+0.25}_{-0.25}$
$1.5-1.8$	$0.73^{+0.069}_{-0.035}$	$0.74^{+0.033}_{-0.035}$	$0.74^{+0.035}_{-0.037}$	$0.73^{+0.061}_{-0.068}$	$0.65^{+0.1}_{-0.12}$	$0.5^{+0.18}_{-0.18}$	$0.75^{+0.15}_{-0.21}$	0^{+1}_{-0}
$1.8-2.1$	$0.71^{+0.048}_{-0.051}$	$0.76^{+0.031}_{-0.033}$	$0.78^{+0.032}_{-0.035}$	$0.77^{+0.058}_{-0.066}$	$0.78^{+0.11}_{-0.15}$	$0.75^{+0.15}_{-0.21}$	$0.75^{+0.15}_{-0.21}$	0^{+1}_{-0}
$2.1-2.4$	$0.78^{+0.039}_{-0.043}$	$0.78^{+0.035}_{-0.038}$	$0.77^{+0.041}_{-0.044}$	$0.76^{+0.082}_{-0.097}$	$0.55^{+0.14}_{-0.14}$	$0.4^{+0.19}_{-0.18}$	$0.5^{+0.25}_{-0.25}$	$0.5^{+0.25}_{-0.25}$
$2.4-2.7$	$0.75^{+0.085}_{-0.1}$	$0.86^{+0.064}_{-0.085}$	$0.57^{+0.089}_{-0.092}$	$0.83^{+0.11}_{-0.17}$	$1^{+0}_{-0.44}$	0^{+1}_{-0}	0^{+1}_{-0}	0^{+1}_{-0}